Proceedings, 5th Chaotic Modeling and Simulation International Conference, 12 – 15 June 2012, Athens Greece

Negative Differential Resistance of the Discharge Plasma through Fractal Space-Time Theory

Maricel Agop[1,a], Dan G. Dimitriu[2,b], Silviu Gurlui[2,c]

[1]Department of Physics, "Gh. Asachi" Technical University, Iasi, Romania
[2]Faculty of Physics, "Alexandru Ioan Cuza" University, Iasi, Romania
[a]E-mail: m.agop@yahoo.com
[b]E-mail: dimitriu@uaic.ro
[c]E-mail: sgurlui@uaic.ro

Abstract: Negative differential resistance effect in the current-voltage characteristic of an electrode immersed into plasma, associated with the bistability, hysteresis and generation of a fireball, was experimentally evidenced. This instability is modeled in the frame of the scale relativity theory. So, we assume that the charged particle movements take place on continuous but non-differentiable curves, *i.e.* on fractal curves. Then, the complexity of these dynamics is substituted by fractality. Every type of elementary process from plasma induces both spatio-temporal scales and the associated fractals. The movement complexity is directly related to the fractal dimension; the fractal dimension increases as the movement becomes more complex. We obtained a very good agreement between the experimental results and those provided by the theoretical model.
Keywords: Negative differential resistance, Bistability, Hysteresis, Fractal, Scale relativity theory, Pattern formation.

1. Introduction

The transitions between distinctly stable states are very often observed in physical science and technology, especially in systems in which transport of electrical charges occurs. These transitions are associated with bistabilites, experimentally manifested by the presence of the negative differential resistance (NDR) of S- or N-type. Despite of the existence of many models, the physical origin of these effects is still a disputed subject in nonlinear physics.

In plasma physics it is well known that the S-type NDR is related to the appearance and disruption of a complex space charge structure (e.g. double layers, multiple double layers, etc.) [1,2,3], whereas the N-type NDR is related to the spatio-temporal dynamics of such a structure [4,5], or to the onset of low-frequency instabilities [6,7,8].

A negative resistance requires an active component in the electrical circuit able to act as a source of energy. In plasma systems, this component could be a self-consistent double layer existing at the border of a fireball. The double layer works as a nonlinear element of circuit able to convert thermal energy into electrical energy, creating all the conditions necessary for the appearance of the S-type NDR in the current-voltage characteristic of a plasma conductor.

Here, we report on experimental results and theoretical modeling of the S-type NDR effect in plasma conductors. The proposed theoretical model explains the relation between the negative differential resistance and the self-structuring of

plasma as double layer, as well as the shape of the current-voltage characteristic of an electrode immersed into plasma, in conditions in which a double layer structure appears in front of it.

2. Experiment

The experiments were performed in a plasma diode, schematically presented in Fig. 1. Plasma is created by an electrical discharge between the hot filament (marked by F in Fig. 1) acting as cathode and the grounded tube (made of non-magnetic stainless steel) as anode. Plasma density may be changed by varying the discharge current. The plasma was pulled away from equilibrium by gradually increasing the voltage applied to a tantalum disk electrode (marked by E in Fig. 1), under the following experimental conditions: argon pressure $p = 10^{-2}$ mbar, plasma density $n_{pl} \cong 10^7 - 10^8$ cm^{-3} and the electron temperature $kT_e = 2$ eV.

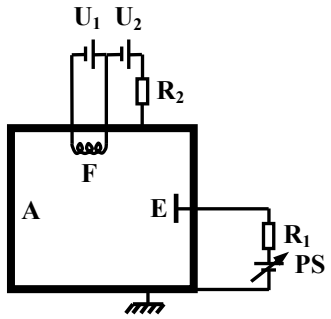

Fig. 1. Schematic of the experimental setup (F – filament, A – anode, E – supplementary electrode, U_1 – power supply for heating the filament, U_2 – power supply for discharge, PS – power supply for supplementary electrode bias, R_1, R_2 – load resistors).

Figure 2 shows a family of current-voltage (I –U) characteristics of the electrode E, obtained for different values of the discharge current (proportional to the equilibrium plasma density). These characteristics were recorded by using an X-Y plotter, which averages the small amplitude fluctuations of the current collected by the electrode. The I - U characteristic starts with an ohmic branch (linear dependence between I and U), ending at a critical value of the voltage applied on the electrode, when a sudden increase of the current appears, associated with a negative differential resistance effect. In other experimental conditions (higher plasma densities and lower values of the load resistor), a sudden jump of the current was recorded [8]. Figure 3 shows such a characteristic recorded by increasing and subsequently decreasing the voltage applied on the electrode. The hysteresis phenomenon is also present in this case. Simultaneously with the current increase, an intense luminous, almost spherical structure develops in front of the electrode, known as fireball or ball-of-fire (see photo in Fig. 4). Emissive probe measurements proved that the structure consists

of a positive core (ion-rich plasma) confined by an electrical double layer. The voltage across the double layer is equal with the ionization potential of the used gas, argon in this case. The development of the fireball corresponds to the negative differential resistance region of the current-voltage characteristic.

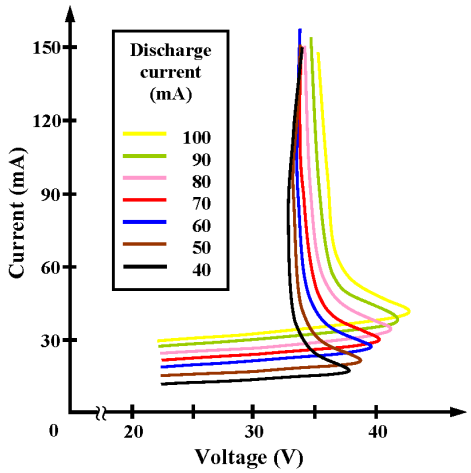

Fig. 2. Set of current-voltage characteristics of the electrode E, for different values of the discharge current (proportional to the plasma density).

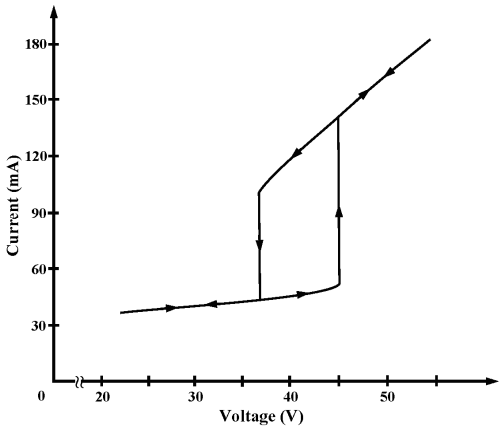

Fig. 3. Current-voltage characteristic of the electrode E at the value of the discharge current I_d = 150 mA.

Fig. 4. Photo of the fireball developed in front of the supplementary electrode E.

2. Theoretical model

Since the instability analyzed here is generated at spatio-temporal scales at which the ionic component of plasma is inertial, while the electronic one is not inertial, we will analyze in the following just the electronic component of plasma. All the physical quantities that describe the dynamics will be normalized with respect to the quantities characteristic of the electronic component of plasma. By employing the one-dimensional hydrodynamic model, we can write the dynamic equations for particles as follows [9]
i) the continuity equation

$$\frac{\partial n}{\partial t}+\frac{\partial (nv)}{\partial x}=0 \tag{1}$$

ii) the momentum equation

$$\frac{\partial v}{\partial t}+v\frac{\partial v}{\partial x}=\frac{q}{m}\frac{\partial \varphi}{\partial x}-\frac{1}{nm}\frac{\partial p}{\partial x}+\zeta \tag{2}$$

where n, m, q, v are the density, mass, charge and speed of electrons, respectively, while p is the pressure, φ is the electrostatic potential and ζ is the electron-neutral collision term. Using the normalized variables

$$\tau=\omega_p t,\ \xi=x/\lambda_D,\ N=n/n_0,\ V=v/c,$$
$$\phi=q\varphi/(k_B T),\ c^2=\gamma k_B T/m,\ \bar{\zeta}=\zeta/c\omega \tag{3a-g}$$

where ω_p is the plasma frequency, λ_D is the Debye length, n_0 is the equilibrium density of particles, c is the acoustic speed, k_B is the Boltzmann constant, T is the particle temperature and γ is the adiabatic index, the equations systems (1) and (2) become

$$\frac{\partial N}{\partial \tau}+\frac{\partial(NV)}{\partial \xi}=0 \tag{4}$$

$$\frac{\partial V}{\partial \tau}+V\frac{\partial V}{\partial \xi}=\frac{\partial \phi}{\partial \xi}-\frac{1}{N}\frac{\partial N}{\partial \xi}+\bar{\zeta} \tag{5}$$

In the following, we will build an analytical solution for the system (4) and (5), in the stationary case, by considering that the quasi-neutrality condition for plasma is fulfilled at any time (which involves the abandon of the Poisson equation), while the electron pressure adiabatically varies (for details see [9]). For this, in the equations system (4) and (5) we make the following change of variable:

$$\theta=\xi-W\tau \tag{6}$$

where W is a quantity that will be later specified. With this transformation, we find:

$$-W\frac{dN}{d\theta}+\frac{d(NV)}{d\theta}=0 \tag{7}$$

$$-W\frac{dV}{d\theta}+V\frac{dV}{d\theta}=\frac{d\phi}{d\theta}-\frac{1}{N}\frac{dN}{d\theta}+\bar{\zeta} \tag{8}$$

After integration, from the continuity equation it results

$$N(V-W)=-c_1,\ c_1=\text{const.} \tag{9a,b}$$

while from the momentum equation it results

$$\frac{V^2}{2}-WV=\phi-\ln N-c_2(\theta),\ c_2(\theta)=-\int\bar{\zeta}(\theta)d\theta \tag{10a,b}$$

Now, through the current density

$$J=NV=-c_1+NW \tag{11}$$

we obtain the voltage-current characteristic $\phi=\phi(J,\theta)$ in the form

$$\phi(J,\theta) = -\frac{W^2}{2} - \ln\frac{W}{c_1} + \frac{W^2}{2\left(\frac{J}{c_1}+1\right)^2} + \ln\left(\frac{J}{c_1}+1\right) - c_2(\theta) \qquad (12)$$

In the equation (12), it's very difficult to find the explicit form of the collision term $c_2(\theta)$ (for details see [9,10]). We can simplify the problem by supposing that the dynamics of the electronic component of the diode plasma display chaotic behaviors (self-similarity and strong fluctuations at all possible scales [11,12]), so that the electrons move on continuous but non-differentiable curves, i.e. fractal curves. Between two successive collisions the trajectory of any particle is a straight line, while the trajectory becomes non-differentiable in the impact point [12,13,14]. Once such a hypothesis is accepted, specific mechanisms are started [12,13,14] leading to the following results:

(i) the explicit form of the collision term is assimilated by the fractality of the electrons trajectories, so that the electrons motion becomes "free". Mathematically, this means that c_2 is independent of the variable θ, i.e. $c_2(\theta) \to c_2 = \text{const}$, case in which relation (12) becomes:

$$\phi(J) = -\frac{W^2}{2} - \ln\frac{W}{c_1} + \frac{W^2}{2\left(\frac{J}{c_1}+1\right)^2} + \ln\left(\frac{J}{c_1}+1\right) - c_2 \qquad (13)$$

(ii) the dynamics of the electronic component of the diode plasma can be described through fractal functions [11,12], i.e. functions that depend on both standard coordinates (time and space coordinates) and resolution scale. In such a conjecture, let's consider the approximation $J/c_1 << 1$ in relation (13) with the choice $W = c_1\exp(-c_2)$. We obtain:

$$\phi + \frac{W^2}{2} \approx \frac{W^2}{2\left(1+2\frac{J}{c_1}\right)} + \frac{J}{c_1} \qquad (14)$$

By extending in the complex space and by recalibrating the coordinates origin

$$2\frac{J}{c_1} \to i\bar{J},\ W \to ia,\ 2\phi \to i\bar{\phi} \qquad (15a\text{-}c)$$

relation (14) becomes:

$$\bar{\phi} \approx \bar{J}\left(1+\frac{a}{1+\bar{J}^2}\right) \tag{16}$$

Equation (23) is of the third order in $\bar{J}$, so it could have three real roots, i.e. to a single value of the field $\bar{\phi}$ correspond three different values of the field $\bar{J}$. The curves $\bar{J} = F\left(\bar{\phi}\right)$ in Fig. 5 show a maximum and a minimum when the parameter *a* surpasses a certain value. These maximum and minimum values can be found by canceling the first derivative of the function (16):

$$\frac{d\bar{\phi}}{d\bar{J}} = 0 \quad \Rightarrow \quad 1+\frac{a\left(1-\bar{J}^2\right)}{\left(1+\bar{J}^2\right)^2} = 0 \tag{17}$$

This is a biquadratic equation with the solutions:

$$\bar{J}_{1,2}^2 = \frac{1}{2}\left[\left(a-2\right) \pm \sqrt{a\left(a-8\right)}\right] \tag{18}$$

Equation (18) will have two different real (positive) solutions only if $a > 8$. For such values of the parameter *a*, the curve $\bar{J} = F\left(\bar{\phi}\right)$ has two extremes, so the system shows bistability. This situation is easy to be understood if we look at the curve corresponding to $a = 18$ in Fig. 5. If $\bar{\phi}$ slowly increases from $\bar{\phi} = 0$, $\bar{J}$ increases until it reaches the point marked by B. Further increasing $\bar{\phi}$ will determine a sudden jump of $\bar{J}$ until the point marked by C is attained, because the region BD of the curve contains unstable states, which cannot be experimentally accomplished. When $\bar{\phi}$ decreases from values greater than the critical value corresponding to the point marked by C, $\bar{J}$ decreases until the point marked by D is reached. If we further decrease the value of $\bar{\phi}$, $\bar{J}$ will jump to the point marked by A, following the curve to the origin. Thus, for values of the field $\bar{\phi}$ in the interval AB, the field $\bar{J}$ can have two different stable values. This bistable behavior determines the negative differential resistance. A good qualitative agreement can be observed between the experimental current-voltage characteristics from Figs. 2 and 3 and those obtained from the theoretical model in Fig. 5. In such a context, the quantity *W* is proportional (through the quantity *a*) to the normalized discharge current density.

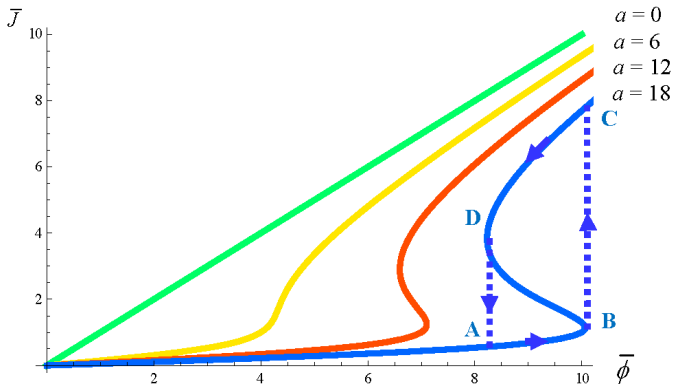

Fig. 5. Theoretical dependence of the normalized current on the normalized potential.

3. Conclusions

A negative differential resistance effect in the current-voltage characteristic of an electrode immersed into plasma was experimentally recorded. It was found that this instability appears simultaneously with the generation of a fireball at the increasing of the voltage applied to the electrode. In order to explain these experimental results, a theoretical hydrodynamic model was built assuming that the ionic component of plasma is inertial, the electronic component is non-inertial and that the electrons move on continuous but non-differentiable curve, i.e. fractal curves. The negative differential resistance effect is associated to a bistability.

Acknowledgment

This work was supported by the Romanian National Authority for Scientific Research, CNCS-UEFISCDI, project number PN-II-ID-PCE-2011-3-0650.

References

1. R. A. Bosch and R. L. Merlino. Sudden jumps, hysteresis, and negative resistance in an argon plasma discharge. I. Discharges with no magnetic field, *Contrib Plasma Phys* 26:1-12, 1986.
2. E. Lozneanu, V. Popescu and M. Sanduloviciu. Negative differential resistance related to self-organization phenomena in a dc gas discharge. *J Appl Phys* 92:1195–1199, 2002.
3. S. Chiriac, M. Aflori and D. G. Dimitriu. Investigation of the bistable behaviour of multiple anodic structures in dc discharge plasma. *J Optoelectron Adv Mater* 8:135–138, 2006.
4. M. Sanduloviciu, E. Lozneanu and S. Popescu. On the physical basis of pattern formation in nonlinear systems. *Chaos Solitons and Fractals* 17:183–188, 2003.
5. S. Popescu. Turing structures in dc gas discharges. *Europhys Lett* 73:190–196, 2006.

6. C. Avram, R. Schrittwieser and M. Sanduloviciu. Nonlinear effects in the current-voltage characteristic of a low-density Q-machine plasma: I. Related to the potential relaxation instability. *J Phys D: Appl Phys* 32:2750-2757, 1999.
7. C. Avram, R. Schrittwieser and M. Sanduloviciu. Nonlinear effects in the current-voltage characteristic of a low-density Q-machine plasma: II. Related to the electrostatic ion-cyclotron instability. *J Phys D: Appl Phys* 32:2758-2762, 1999.
8. S. Chiriac, D. G. Dimitriu and M. Sanduloviciu. Type I intermittency related to the spatiotemporal dynamics of double layers and ion-acoustic instabilities in plasma. *Phys Plasmas* 14:072309, 2007.
9. F. F. Chen. *Introduction to Plasma Physics*, Plenum Press, New York, 1974.
10. Y. Elskens and D. Escande. *Microscopic Dynamics of Plasma and Chaos*, IOP Publishing, Bristol, 2002.
11. B. Mandelbrot. *The Fractal Geometry of Nature*, Freeman, San Francisco, 1982.
12. L. Nottale. *Scale Relativity and Fractal Space-Time – A New Approach to Unifying Relativity and Quantum Mechanics*, Imperial College Press, London, 2011.
13. M. Agop, D. Alexandroaei, A. Cerepaniuc and S. Bacaita. El Naschie's $\varepsilon(\infty)$ space-time and patterns in plasma discharge. *Chaos Solitons and Fractals* 30:470-489, 2006.
14. O. Niculescu, D. G. Dimitriu, V. P. Paun, P. D. Matasaru, D. Scurtu and M. Agop. Experimental and theoretical investigations of a plasma fireball dynamics. *Phys Plasmas* 17:042305, 2010.

Dynamic similarities of rotors with rubbing blades

Jan-Olov Aidanpää

Luleå University of Technology, Luleå, Sweden

E-mail: joa@ltu.se

Abstract: The non-linear behaviour of rubbing cylindrical rotors have been studied in several papers. In such systems rich dynamics have been found for frequencies above the natural frequency. Below natural frequency the solution was found to be stationary. In this paper the influence of blades is studied. A Jeffcott rotor with three, five, ten and fifty blades is used and the contacts are described by large displacement beam theory. The model shows that bladed turbines have a similar dynamic behaviour if scaled properly. This imply that general conclusions for a simple system can be extracted to a more complex one. However it is also shown that the forces and amplitudes are not easily scaled and therefore if the values are wanted one have to simulate the actual system.

Keywords: rotor, dynamic, impact, rubbing, beam, blade.

1. Introduction

In rotor dynamics there are several situations when non-linear problems can occur. One such example is rub-impact which is a highly non-linear phenomenon. The problem is of industrial interest since there are several applications where rub-impact is the main cause for unwanted vibrations e. g. gas turbines, centrifuges, compressors and generators. It has been reported that 10.2% of 275 reported jet engine failures during 1962 to 1975 were caused was rubbing between rotating and stationary parts [1]. Several studies have been performed on the Jeffcott rotor with this kind of rubbing impacts. Some of them are described below, with focus on findings and development of methods.

The jump phenomenon and the influence of radial clearance were studied analytically in [2]. A modified Harmonic Balance method has been used to predict the occurrence and analyse the stability of quasi-periodic motion [3]. In [4] Fourier series and Floquet theory was used for analysis of global bifurcation and stability. They also reported three routes to chaos; from stable periodic through period doubling bifurcations, grazing bifurcation and a sudden transition from periodic motion to chaos. The stability for the case of full annular rub and cross coupling stiffness was analysed in [5]. Chaos has been reported to exist over large parameter ranges and different solutions can coexist [6]. In [7] approximate analytical solutions was developed for non-linear dynamical responses and in [8] the harmonic balance method was used to calculate periodic responses of the non-linear system. In most cases the contact was modelled with an increased stiffness and Coulomb friction. However, other frictional models has also been considered [9]. In all models with annular rub,

the system reaches a stationary point below the natural frequency of the rotor. It is only above the natural frequency where complex dynamics and multiple solutions are found [10]. In these models the rotor and stator was assumed to be circular. Bladed rotors in aero engines have also been studied with complex FEM models [12]. Due to the complexity of these models only short time sequences has been analysed and therefore the dynamics on parameter ranges is still unknown.

In a recent paper an attempt was made to model a rubbing Jeffcott rotor with three blades where the displacements were described by large displacement beam theory [13]. The model showed that when blades are included rich dynamics was found below the natural frequency of the rotor. Simulation time was also short which made the model suitable for numerical analysis. In this paper the same model is used but the dynamic influence of the number of blades is studied. The target is to evaluate similarities and differences in the dynamic when the number of blades are changed.

2. The Model

The model of the Jeffcott rotor is shown in Figure 1 for a case with three blades. The mass of the rotor, m, is supported by the shaft with stiffness k and damping c. The rotor is amplitude limited by the stator which has a radius R. The rotor is described by a point mass m in the centre and n mass less beams of length L, Young's modulus E and area moment of inertia I. The rotor is rotating with the angular velocity ω. In Figure (C) the geometry of the contact is shown. When a blade is in contact the beam will be deformed transversally Δ and axially δ. Both deformations are necessary in order to keep the beam inside the limit radius R. The contact force is described by a radial force P normal to the circle pointing from the contact point towards o and a tangential force μP, where μ is a coefficient of friction. To simplify the analysis it is assumed that ωt-ϕ is small which imply that P is an axial force and μP a tangential force on the beam.

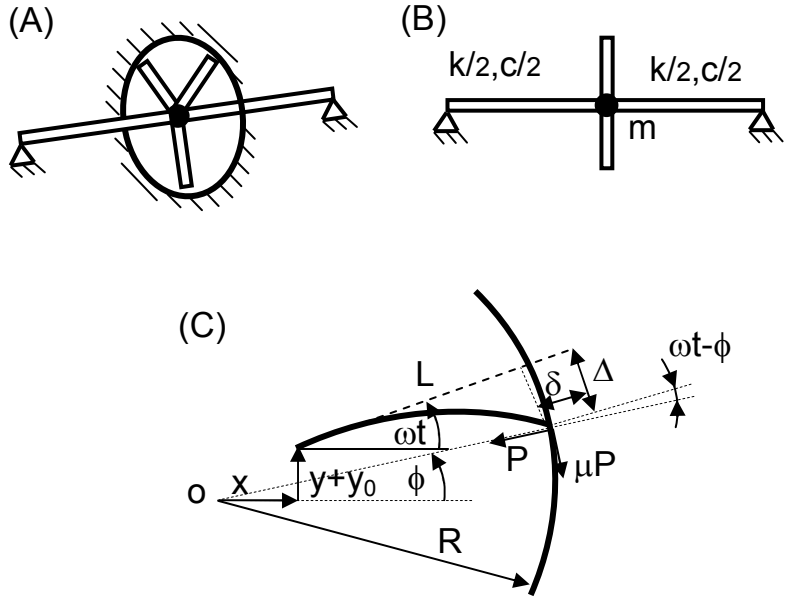

Fig. 1. Rub impact model of the Jeffcott rotor. View of the whole system (A), side view (B) and geometry of the contact (C).

If o is the centre of the stator, the vector to the contact point of the beam can be described as

$$\bar{r} = \left(x + (L-\delta)\cos(\omega t) + \Delta\sin(\omega t)\right)\bar{i} + \left(y + y_0 + (L-\delta)\sin(\omega t) - \Delta\cos(\omega t)\right)\bar{j}$$

where $\bar{i}$ and $\bar{j}$ are unit vectors in x and y direction respectively. The displacement y_0 is an initial misalignment of the rotor. When the rotor is in contact, the rotor is limited by the stator so that

$$|\bar{r}| = R$$

The contact force is described by the radial force P pointing toward o and a tangential component given by a coefficient of friction μP. As noted above, it is assumed that the contact angle $\phi = \omega t$ and therefore the forces on the beam are given by an axial compression force P and a transversal force μP. From beam theory the deformation of cantilevered beam is given by the equation

$$w''(\varepsilon) = \frac{P}{EI}\left(1 + (w')^2\right)^{3/2}\left((\Delta - w(\varepsilon)) + \mu P(L - \varepsilon - \delta)\right)$$

where " ′ " denotes derivation with respect to ε. The beam is assumed clamped at $\varepsilon=0$ and subjected to the forces P and μP on the free end ($\varepsilon=L-\delta$). At the free end, the beam will be displaced by the forces axially δ and transversally Δ. By numerical integration the values of P Δ and δ can be found which satisfies $|\bar{r}| = R$. When a blade is in contact the forces in x and y directions are;

$$Fx = P\frac{\bar{r}\bullet\bar{i}}{R} - \mu P\frac{\bar{r}\bullet\bar{j}}{R} \quad ,$$

$$Fy = P\frac{\bar{r}\bullet\bar{j}}{R} + \mu P\frac{\bar{r}\bullet\bar{i}}{R} \quad .$$

For n blades there will be one set of such forces (Fx_i, Fy_i) for each blade i, hence the equation of motion for the Jeffcott rotor then becomes

$$\ddot{x} + 2\varsigma\omega_n\dot{x} + \omega_n^2 x = -\sum_{i=1}^{n} Fx_i / m$$

$$\ddot{y} + 2\varsigma\omega_n\dot{y} + \omega_n^2 y = -\sum_{i=1}^{n} Fy_i / m$$

In this paper four cases will be studied with different number of blades. In Figure 2 the four cases are shown where (a) is three blades, (b) five blades, (c) ten blades and (d) fifty blades.

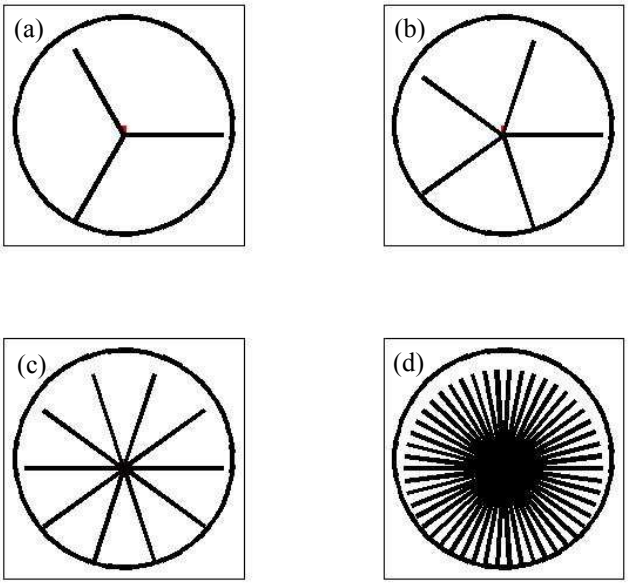

Fig. 2. Rub impact model for different number of blades. (a) three blades, (b) five blades, (c) ten blades and (d) fifty blades.

3. Method

In this paper different bifurcation diagrams are used to evaluate the system. In these simulations a fourth order Runge-Kutta integration with adjustable time-step is implemented in an in-house code written in Fortran. In the bifurcation diagrams 100 Poincaré sections was collected after 500 periods of the excitation

frequency ω. For the suggested model there are 5 dimensions in the state space: displacements x, y, velocities $\dot{x}, \dot{y}$ and the phase $\phi = \omega t$. Since the phase can be restricted to the interval *[0, 2π]* it can be described as a circle S^1 with the period $2\pi/\omega$. Thus points in the 5 dimensional state space are given by $(x, \dot{x}, y, \dot{y}, \theta) \in R^4 \times S^1$. The Poincaré section $\sum$ is chosen as the cross section of this state space for a constant value of the phase θ_p. In this paper this constant value is chosen to 2π. Therefore the Poincaré section is defined as

$$\sum = \left\{ x, \dot{x}, y, \dot{y}, \theta_p \mid \theta_p = 2\pi \right\}.$$

Points in this Poincaré sections are the intersections of a trajectory with the plane $\sum$ positioned at the constant phase $\theta_p = 2\pi$. If a root finding routine was applied at each contact, the time for finding *P*, *Δ* and *δ* would make the simulation time consuming. Analysis of bifurcation diagrams and any global dynamics would be difficult. With the assumption $\phi = \omega t$, there will be an unique relation between the forces acting on the beam and the forces in the contact point. By curve fitting of the results from large displacement beam theory, a simple model can be made of the displacements and forces in contact. An effective simulation program can thereby be made to analyse the system.

3. Results

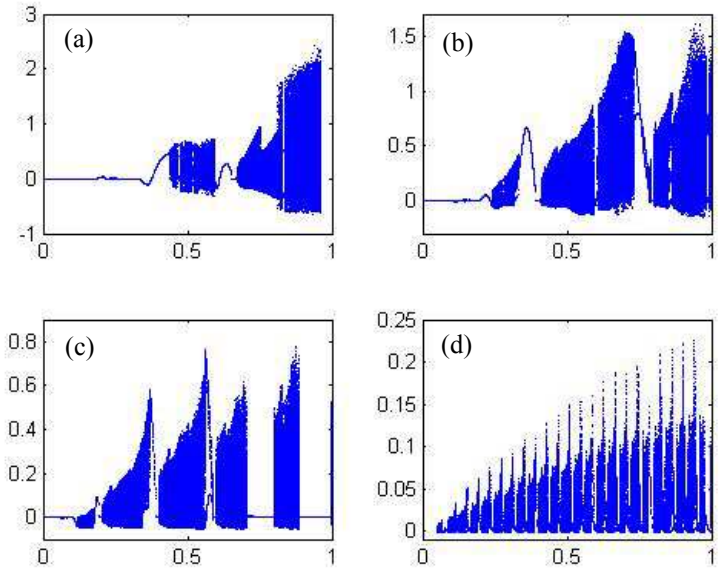

Fig. 3. Bifurcation diagrams for w=0-1 for different number of blades. (a) three blades, (b) five blades, (c) ten blades and (d) fifty blade.

A rubbing system is selected with $R=0.11$, $L=0.1$, $\zeta=0.1$, $y_0=0.010001$, $E=2.06\times10^{11}$, $I=0.01\times0.001^3/12$, $m=1$ and $\omega_n=10$ *[SI units]*. The values for EI corresponds to a blade in the shape of a rectangular steel beam with height *0.001[m]* and width *0.01[m]*. In Figure 3 the bifurcation diagrams are shown for the four cases with three, five, ten and fifty blades. The displacement in y is scaled with the clearance ($y/(R-L)$). The figures shows rich dynamics below the natural frequency with an increasing number of chaotic regions for increasing number of blades.

Since the frequency of the impacts will increase with the number of blades, an attempt is made to find similarities in the dynamics by scaling the excitation frequency. In Figure 4 the same cases are shown for the case when the frequency axis is scaled with $n/3$. This is done in order to find similar excitation frequency as in (a) for the other cases. The gray dotted line indicates the maximum displacement for each frequency. In Figure 5 the maximum contact force is plotted for each case.

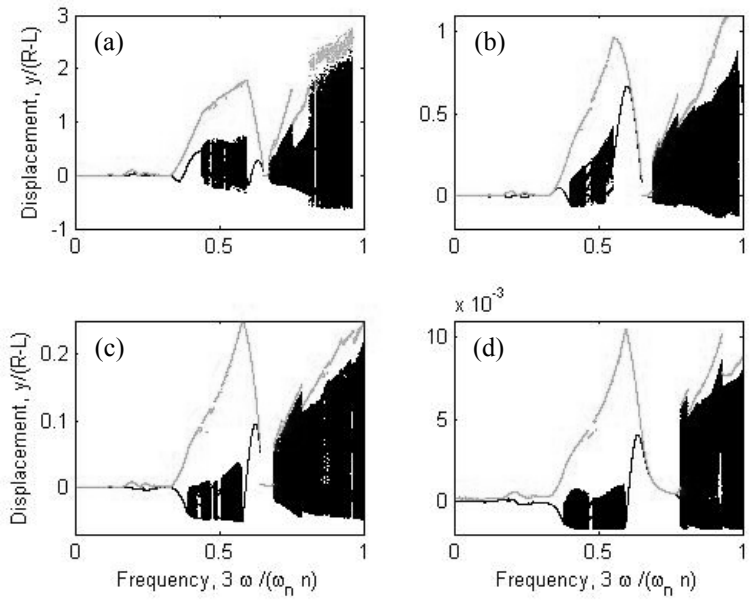

Fig. 4. Scaled bifurcation diagrams for w=0-1 for different number of blades. (a) three blades, (b) five blades, (c) ten blades and (d) fifty blade.

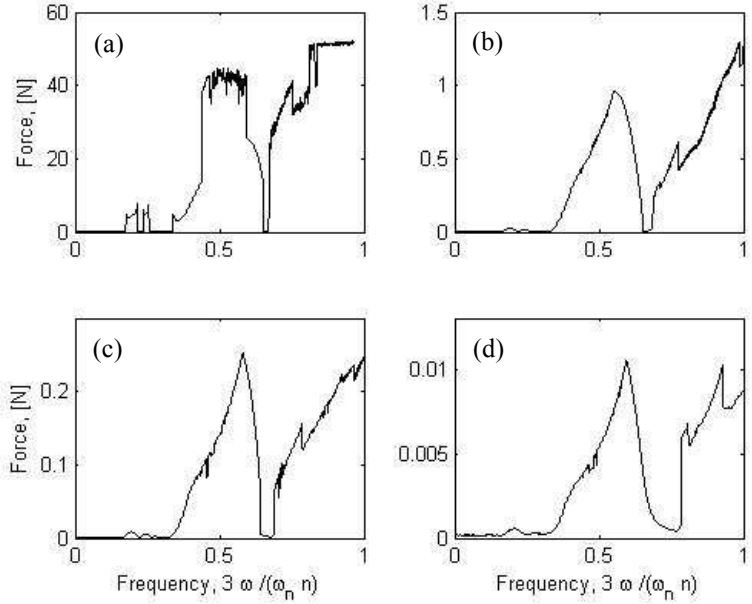

Fig. 5. Maximum contact force for different number of blades. (a) three blades, (b) five blades, (c) ten blades and (d) fifty blade

4. Discussion and Conclusion

Rubbing rotors have been studied extensively but mainly with models describing the rotor and the stator as cylinders. In several industrial applications the rotor consists of blades which conditions at contact significantly differs from the perfect circle. The target of this paper is to evaluate similarities and differences for rubbing bladed rotors with different number of blades. Four cases are compared namely three, five, ten and fifty blades. In the bifurcation diagrams in Figure 3 it is shown that the amplitude decreases when the number of blades is increased. It is also shown that the number of regions with long periodic or chaotic behaviour increases for more blades. For three blades the system becomes unstable for frequencies close to the natural frequency of the system. For the other number of blades no such instability was found.

Since the excitation frequency increases with the number of blades, the frequency axis is scaled with, *n/3* (number of blades/3). Then, it was shown that the dynamics for scaled frequency was similar for the systems with peak amplitudes and chaotic regions in the same range. For low frequencies the amplitude is low but for an excitation frequency larger then ω_n/n the amplitude starts to grow. At about $0.4\omega_n/n$ a chaotic region is found and the vibration reaches a peek at the end of the chaotic region at about $0.6\omega_n/n$. Then a short periodic interval of low amplitude appears followed by a new chaotic interval

with increased amplitudes. The forces of Figure 5 shows peaks at the same position as the maximum vibration amplitudes. The actual value of maximum force or the maximum amplitude could not be scaled but it was shown that they will decrease with the number of blades.

At low frequencies ($<2.4\omega_n/n$), the simulations indicates that general dynamics such as areas of high amplitudes and forces can be predicted together with location of the two first regions of chaotic motion. But for higher frequencies the dynamic will differ due to the number of blades.

References

1. A. F. Kascak, A. B. Palazzolo and G.Montaque. Transient Rotor Dynamic Rub Phenomena, Theory and Test. *Rotating Machinery Dynamics*. 2: 485-494, 1987.
2. J. L. Isaksson. Dynamics of a rotor with annular rub. *Proceedings of IFTOMM 4th International Conference on Rotor Dynamics, Chicago*, 85-90, 1994.
3. Y.-B. Kim and S. T. Noah. Quasiperiodic response and stability analysis for a nonlinear Jeffcott rotor. *J. of Sound and Vibration*. 190: 239-253, 1996.
4. F. Chu and Z. Zhang. Bifurcation and chaos in a rub-impact Jeffcott rotor system. *J. of Sound and Vibration*. 210: 1-18, 1998.
5. J. Jiang and H.Ulbrich. Stability analysis of sliding whirl in a nonlinear Jeffcott rotor with cross-coupling stiffness coefficients. *Nonlinear Dynamics*. 24: 269-283, 2001.
6. E. V. Karpenko, M.Wiercigroch and M. P. Cartmell. Regular and chaotic dynamics of a discontinuously nonlinear rotor system. *Chaos, Solitons & Fractals*. 13: 1231-1242, 2002.
7. E. V. Karpenko, M. Wiercigroch, E. E. Pavlovskaia and M. P. Cartmell. Piecewise approximate analytical solutions for a Jeffcott rotor with a snubber ring. *International Journal of Mechanical Sciences*, 44: 475-488, 2002.
8. G. Von Groll and D. J. Ewins. The harmonic balance method with arc-length continuation in rotor/stator contact problems. *J. of Sound and Vibration*, **241**(2): 223-233, 2001.
9. A. F. Kascak and J. J.Tomko. Effects of Different Rub Models on Simulated Rotor Dynamics. *NASA Technical Paper 2220*. 1984
10. J. O. Aidanpää. Multiple solutions in a rub-impact Jeffcott rotor. *The 10th of International Symposium on Transport Phenomena and Dynamics of Rotating Machinery, Honolulu, Hawaii, March 07-11*. ISROMAC10-2004-120, 2004.
11. M. Legrand, C. Pierre, P. Cartraud and J.-P. Lombard. Two-dimensional modeling of an aircraft engine structural bladed disc-casing modal interaction. *J. of Sound and Vibration,* 319: 366-391, 2009.
12. J-O. Aidanpää, G. Lindkvist, Dynamics of a Rubbing Jeffcott Rotor with Three Blades, CHAOS 2009, The 3rd Chaotic Modeling and Simulation International Conference,MAICh Conference Centre, Chania, 1 - 4 June 2010.

Chaotic Trend Possibility in the Gold Market

Nilufer Alan[†], Ilknur Kusbeyzi Aybar[*], O. Ozgur Aybar[†▪], Avadis S. Hacinliyan[†‡]

[†]Yeditepe University, Department of Information Systems and Technologies, Istanbul, Turkey
[‡]Yeditepe University, Department of Physics, Istanbul, Turkey
[*]Yeditepe University, Department of Computer Education and Instructional Technology, Istanbul, Turkey
[▪]Gebze Institute of Technology, Department of Mathematics, Kocaeli, Turkey

E-mail: oaybar@yeditepe.edu.tr
E-mail: ahacinliyan@yeditepe.edu.tr
E-mail: ikusbeyzi@yeditepe.edu.tr
E-mail: nlfr_alan@hotmail.com

Abstract: In this study, the International market gold prices over the last 31 years were analyzed for trends by five different methods, linear trend analysis, ARMA analysis, Rescaled range analysis, attractor reconstruction and maximal Lyapunov Exponent, detrended fluctuation analysis. Unfortunately not all methods give consistent results. The linear analysis reveals three regions with different trends. This is not supported by the rescaled range or detrended fluctuation analysis results. The maximal Lyapunov exponent calculation reveals chaotic behavior. The detrended fluctuation analysis reveals behavior close to brown noise. This is not corroborated by the rescaled range analysis, which indicates anti persistent behavior. The ARMA model implies first differencing that indicates a strong underlying linear trend.
Combining these results, one probable explanation is that the strong linear trend, (also corroborated by ARMA analysis) affects the rescaled range calculation, because of its dependence on extreme values. The detrended fluctuation analysis removes this trend and reveals brown noise. This is consistent with a maximal positive Lyapunov exponent. Hence, we have a linear trend plus brown noise and neither of these two effects is dominant.

Keywords: Dynamical systems, Gold Markets, Lyapunov exponents, Nonlinear Time Series Analysis.

1. Introduction

The goal of this paper is to provide a practical and accessible example for linear and nonlinear time series modeling. As a case study Gold prices in International markets between January 2, 1973 and March 31, 2011 is chosen. This field of study has been chosen for two main reasons. First, up-to-date data are available and it is free to download from international agencies. Second, Gold prices had important effects on international monetary system which is explained in Section two. In section three, time series definition and its key features are explained such as trend, seasonality. In section four, one dimensional time series

analysis of ARIMA and its components are explained. Section five is arranged for non linear time series analysis methods and linear and non linear time series analysis results are given. Gold has been the foundation of monetary systems for centuries. To illustrate the importance of Gold in monetary systems over the last century, one could start with the end of the British Gold Standard in 1914 to permit inflationary financing of World War I. As with all monetary inflations, it resulted in a buildup of debt as the public borrowed in order to spend money before loss of its purchasing power, with a view to repaying borrowings with currency after relative loss of its purchasing power. The end of monetary inflation in 1921 brought a return to stability for the UK and US. In 1929, collapse of overpriced equity markets resulted in deflation of consumer demand and depression. The cure for this came in 1935 by devaluing the paper money thus raising the paper money price of Gold. To restore stability and to avoid giving a message in favor of possible further inflation of the World Monetary Base, Foreign Exchange Rates were then fixed against Gold and the US Dollar was made convertible into Gold at a set price. The 1935 was ratified at Bretton Woods in 1944. Integrity of the US Dollar was guaranteed by the right of non-US Central Banks to convert their US Dollars to Gold if they feared that the purchasing power of the Dollar could be devalued through excess creation of money. However, in 1968 this arrangement was informally, and in 1971 formally, ended. The World Monetary system came off the US Gold Standard to permit inflationary financing which led directly to the Great Inflation of the 1970's and which, as usual, touched off a resurgence in debt. The 1970's Great Inflation of money ended in 1981, resulting in falling interest rates and strengthening bond and equity prices[1,2].

2. Nonlinear Time Series Analysis

Chaos occurs from the nonlinear evolution of systems. Chaotic dynamical systems are ubiquitous in nature such as the tornado, stock market, turbulence, and weather. Firstly, phase space reconstruction is necessary to understand that whether time series has chaotic behaviors or not[3,4,5].

The most striking feature of chaos is the limit of unpredictability of its future. This feature is usually called as the "sensitive dependence on initial conditions" or referring to the Lorenz models behavior, "butterfly effect. In this section, we will look at the details of nonlinear time series analysis by using mutual information, embedding dimension, maximal Lyapunov exponents, detrended fluctuation analysis and rescaled range analysis[6,7].

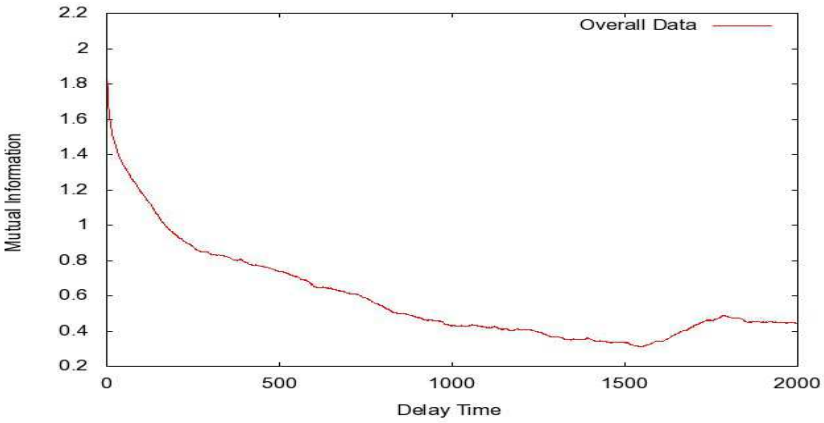

Fig. 1. Mutual Information of Overall Data

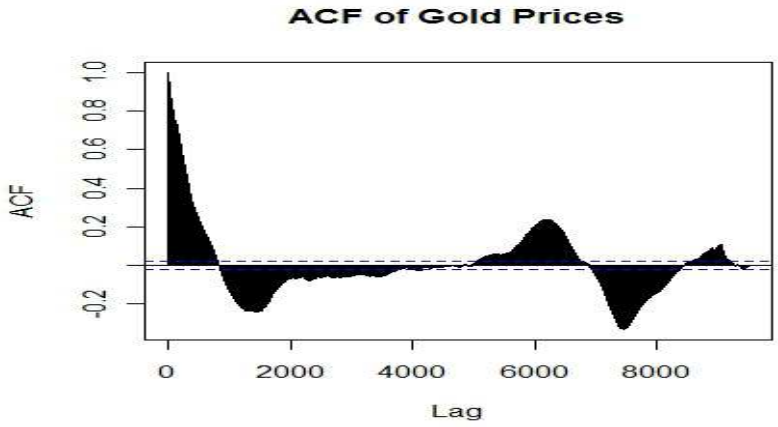

Fig. 2. Autocorrelation function of Gold prices (ACF vs. Lag)

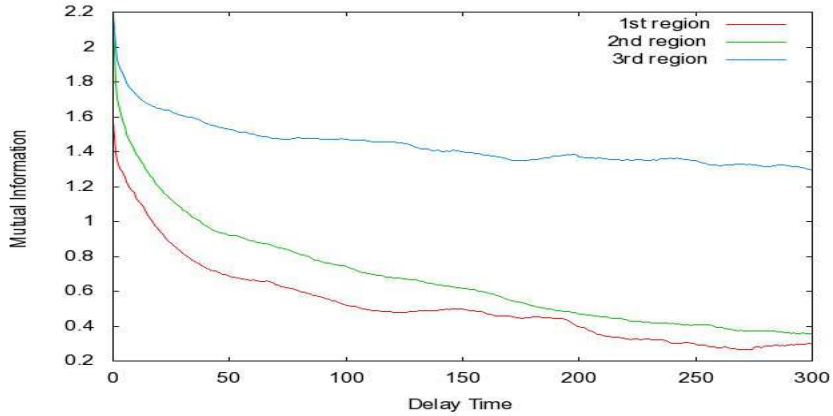

Fig. 3. Mutual Information of Each Region and Overall Data

In order to reconstruct phase space delay time should be found and to find delay time there are basically two methods which are mutual information and autocorrelation function.
As implied in Figure delay time of overall data is nearly 1500. Delay time is expected to be small as far as possible. As second method the calculation of autocorrelation functions were made with R Project statistics package program and also figures were drawn with this program. Figure shows autocorrelation ACF vs. lag and in this figure from first value to nearly 1000th value the ACF rapidly decreases and reaches zero. According to this figure delay time is nearly 1000. After that value it fluctuates between -0.2 and 0.2.The lags do not fall within their standard errors for this reason it is not white noise[8,9].
In each method delay times are too high to evaluate data as a whole. For this reason each region's mutual information was drawn one by one. Delay time chosen from average mutual information is more reliable because it also takes into account possible nonlinearity. For this reason as shown in Figure delay time of each region are calculated and plotted with mutual information method only. Moreover, they are found different from each other. First region's delay time is 100. For second delay time is calculated as 300 and for third region 60.

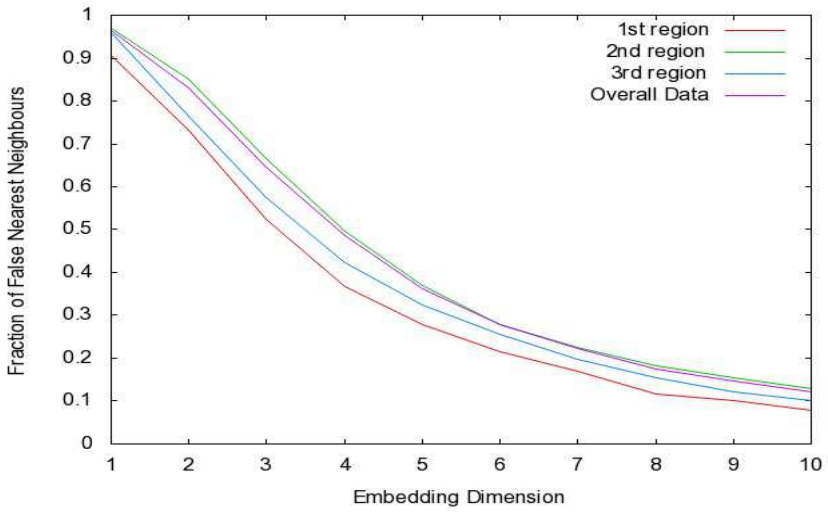

Fig. 4. FNN vs. Embedding Dimension of Each Region and Overall Data

After determining delay times embedding dimensions should be found. To find a satisfactory value for the embedding dimension, false nearest neighbors' method provides a good estimate. After finding delay time for overall data and for each region the fraction of false nearest neighbors are calculated. In Figure14 and the fraction of false nearest neighbors versus embedding dimension are plotted.
Although each regions delay times and trend behaviors' are different from each other, their embedding dimensions are nearly same. All regions embedding dimension graphs' are stabilizing after 8 dimensions.

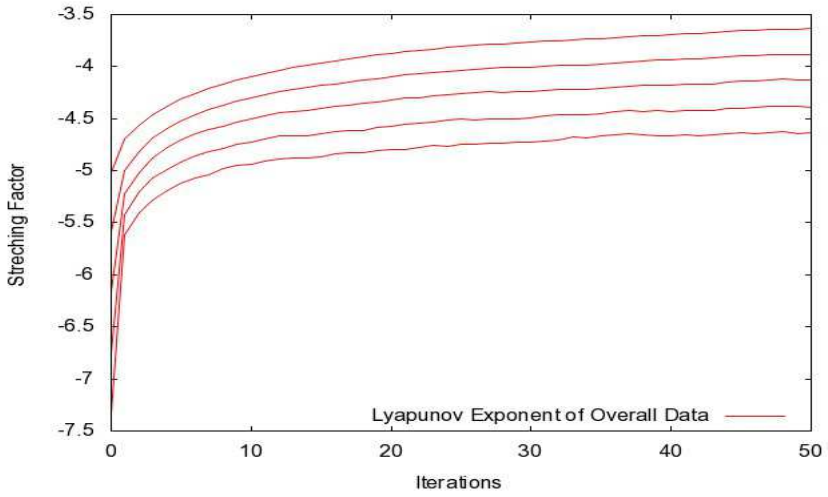

Fig. 6. Lyapunov exponents of Overall Data

The Lyapunov exponents are invariants of the dynamics. The maximal Lyapunov exponents are estimated with the use of TISEAN package and coded as the lyap_k routine. With the fit function of Gnuplot each region's slopes are calculated.1st region's Lyapunov exponent is 0.0308149, in 2nd is 0.0308149, in 3rd is 0.0255495 and Lyapunov exponent of overall data is 0.0175337.As a conclusion a positive Lyapunov exponent is indicated from Gold prices. All Lyapunov exponents are positive on this account they are not stable fixed points .Moreover, they are not equal to ∞. Consequently, they do not indicate random noise. However, they are positive and this shows that this time series is chaotic with a predictibility horizon of approximately 30.

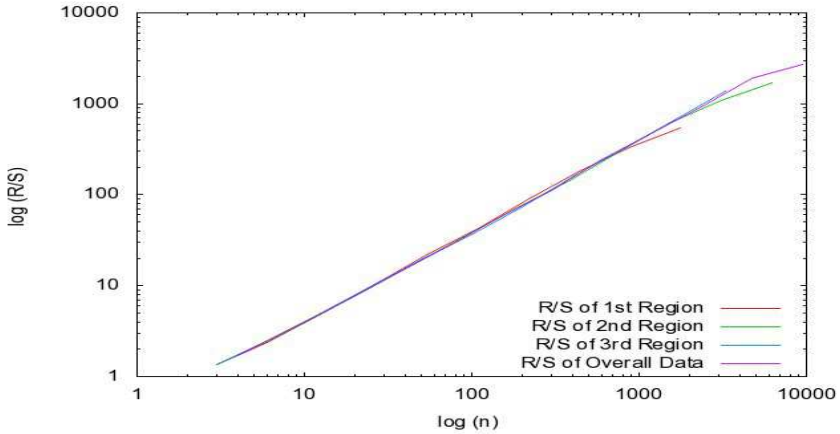

Fig. 7. R/S Analysis of Overall Data and Three Regions

In order to calculate Hurst exponent for each region and overall data Gnuplot and its fit function were used. For each region the Hurst exponent is calculated

and the exponents are found to be very close to each other. In the graph below, 1st region's R/S slope is 0.315411 and for 2nd region is 0.285779, for 3rd is 0.285779 and for overall data is 0.305127. If R/S slope was 0.5 it will be random series but it is positive and less than 0.5. Therefore, we consistently observe anti persistent behavior. There is a linear overall trend, as indicated by the first differencing plus noise. The positive Lyapunov exponent indicates that the noise is broadband.

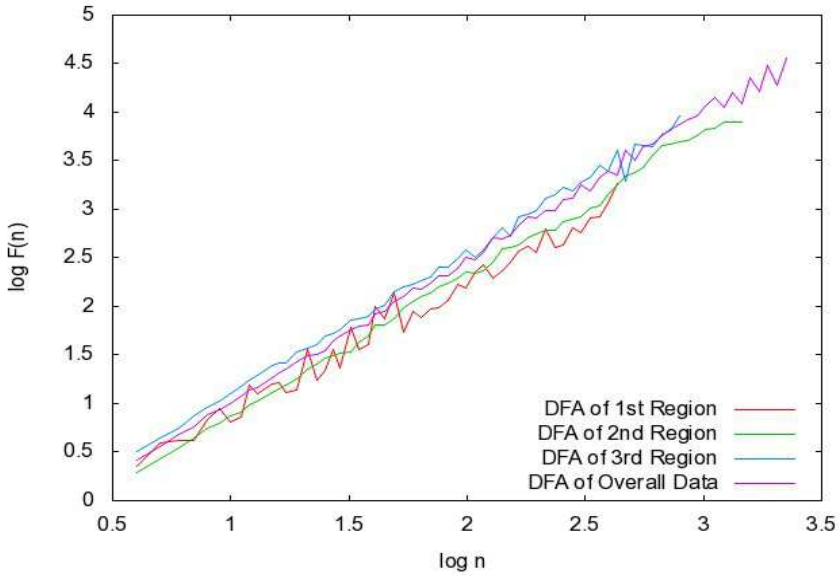

Fig. 8. Log n of Overall Data and Three Regions

As shown in Figure each regions' DFA behavior is very similar to the others .Slopes are calculated with Gnuplot' s fit function and they are found as that 1st region is 1.3136, for 2nd region is 1.45522, 3rd region is 1.46538 and for overall data is 1.4911. As explained in chapter 5 if the slope of DFA is 1.5 it is shows random walk model. All regions especially DFA slope of overall data is nearly 1.5 and it shows random walk model.

3. Conclusions

In this study, the International market gold prices over the last 31 years were analyzed for trends by five different methods, linear trend analysis, ARMA analysis, Rescaled range analysis, attractor reconstruction and maximal Lyapunov Exponent, Detrended fluctuation analysis. Unfortunately not all methods give consistent results. The linear analysis reveals three regions with different trends. This is not supported by the rescaled range or detrended fluctuation analysis results. The maximal Lyapunov exponent calculation reveals chaotic behavior. The detrended fluctuation analysis reveals behavior

close to brown noise. This is not corroborated by the rescaled range analysis, which indicates anti persistent behavior. The ARMA model implies first differencing.
Combining these results, one probable explanation is the strong linear trend, (also corroborated by ARMA analysis) which affects the rescaled range calculation, because of its dependence on extreme values. The detrended fluctuation analysis removes this trend and reveals brown noise. This is consistent with a maximal positive Lyapunov exponent. Hence, we have a linear trend plus brown noise and neither of these two effects is dominant[7,8,9].

References

1. S. Boker. Linear and Nonlinear Dynamical Systems Data Analytic Techniques and an Application to Development Data, A Dissertation Presented to the Graduate Faculty of the University of Virginia in Candidacy f or the Degree of Doctor of Philosophy, 39, 1996.
2. M. Bolgorian, Z. Gharlı. A Multifractal Detrended Fluctuation Analysis Of Gold Price Fluctuations , *Acta Physica Polonica B* , vol. 42, 2011.
3. K. Clayton, F. Vaio. Basic Concepts in Nonlinear Dynamics and Chaos, A Workshop presentation at Society of Chaos Theory in Psychology and the Life Sciences meeting, 1997.
4. C. H. Skiadas. Two simple models for the early and middle stage prediction of innovation diffusion. *IEEE Trans Eng Manage* 34:79–84, 1987.
5. C. H. Skiadas and C. Skiadas. *Chaotic Modeling and Simulation: Analysis of Chaotic Models, Attractors and Forms*, Taylor and Francis/CRC, London, 2009.
6. P. Franses, *Time Series Models for Business and Economic Forecasting*, Cambridge University Press, 9, 1998.
7. H. Kantz, T. Schreiber, *Nonlinear Time Series Analysis*, Cambridge University Press, 2nd Edition, 86, 2004.
8. D. Kugiumtzis, B. Lillekjendlie, N. Christophersen, Chaotic time series: Estimation of invariant properies in state space, *Modeling, Identification, and Control*, vol. 15, 4: 205-224, 1994.
9. O. Cakar, O. O. Aybar, A. S. Hacinliyan, I. Kusbeyzi, Chaoticity in the Time Evolution of Foreign Currency Exchange Rates in Turkey, *CHAOS 2010 3rd Chaotic Modeling and Simulation International Conference*, Greece (2010).


Proceedings, 5th Chaotic Modeling and Simulation International Conference, 12 – 15 June 2012, Athens Greece

Analysis of the bifurcating orbits on the route to chaos in confined thermal convection

Diego Angeli[1], Arturo Pagano[2],
Mauro A. Corticelli[1], Alberto Fichera[2], and Giovanni S. Barozzi[1]

[1] University of Modena and Reggio Emilia, Department of Mechanical and Civil Engineering, Via Vignolese, 905, I-41125 Modena, Italy
(E-mail: diego.angeli@unimore.it)
[2] University of Catania, Department of Industrial and Mechanical Engineering Viale Andrea Doria, 6, I-95125 Catania, Italy
(E-mail: apagano@diim.unict.it)

Abstract. Bifurcating thermal convection flows arising from a horizontal cylinder centred in a square-sectioned enclosure are studied numerically, with the aim of achieving a more detailed description of the sequence of transitions leading to the onset of chaos, and obtaining a more precise estimate of the critical values of the main system parameter, the Rayleigh number Ra. Only a value of the geometric aspect ratio A of the system is considered, namely $A = 2.5$, for which a period-doubling cascade was previously observed. Results give evidence of new and interesting features in the route to chaos, such as a window of quasiperiodic flow and the detection of high-order period orbits.
Keywords: Thermal convection, period-doubling cascade, quasi-periodicity, deterministic chaos.

1 Introduction

Buoyancy-induced flows in enclosures represents one of the most complete multi-scale coupled non-linear fluid flow problems. Their primary importance in the field of the study of bifurcations and chaos is due to the fact that they represent passive systems on which bifurcative dynamics easily show up, and, eventually, lead to relevant observations on the relationship between the onset of chaos and the transition from laminar to turbulent flow.

Many works have been carried out on the non-linear dynamics of thermal convection in basic enclosure configurations, such as the rectangular enclosures heated from below (the Rayleigh-Bénard problem) and from the side [1,2] (the "vertical enclosure" case), and, more recently, the horizontal annulus between two coaxial cylinders [3]. Fewer works dealt with more complex geometrical and thermal configurations [4–6]. Nevertheless, from a theoretical and practical standpoint, the interest in this topic is growing continuously.

The physical system considered in the present study is the cavity formed by an infinite square parallelepiped with a centrally placed cylindrical heating source. The system is approximated to its 2D transversal square section containing a circular heat source, as sketched in Fig. 1. The temperature of both

enclosure and cylinder is assumed as uniform, the cylindrical surface being hotter than the cavity walls. Thus, the leading parameter of the problem is the Rayleigh number Ra, based on the gap width H, expressing the temperature difference in dimensionless terms. Another fundamental parameter is the Prandtl number, fixed for this study at a value $Pr = 0.7$, representative of air at environmental conditions.

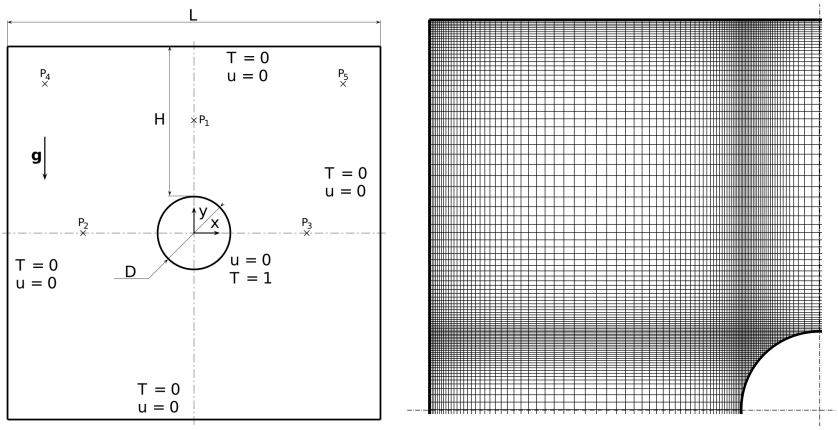

Fig. 1. Left: schematic of the system under consideration; (×) symbols indicate locations of the sampling points. Right: quadrant of the computational grid.

From the standpoint of thermofluids, the convective system in Fig. 1 is particularly interesting, since, due to the curvature of the cylindrical differentially heated surfaces, its phenomenology encompasses the features of both the Rayleigh-Bénard and the vertical enclosure cases. As soon as a temperature difference is imposed between the cylinder and the enclosure, fluid motion ensues immediately in the vicinity of the horizontal midplane, where the cylindrical walls are substantially vertical. On the other hand, the fluid in the top part of the enclosure is subject to an unstable vertical gradient, as in the Rayleigh-Bénard problem, while vertical boundary layers are invariably forming at the enclosure sidewalls. The combination of these situations in a single problem produces a variety of flow configurations and transition phenomena.

Previous studies [5,6] already unfolded different scenarios on the route to chaos of the system considered here, depending on its aspect ratio $A = L/H$. Accurate numerical investigations carried out for two A-values, $A = 2.5$ and $A = 5$, revealed the existence of a period-doubling scenario following a Hopf bifurcation for $A = 2.5$, and a transition to chaos via a symmetry-breaking pattern followed by a blue-sky bifurcation for $A = 5$ [6].

The aim of the present work is to achieve a deeper insight into the series of bifurcations for the case $A = 2.5$, in virtue of a wider set of numerical

simulations performed by refining the step of the bifurcation parameter Ra. Particular attention has been devoted to the analysis of the stretching and folding attitudes of specific regions of the system attractor in proximity of the Ra-values corresponding to the period doubling bifurcation points, and in the chaotic range.

Numerical predictions are carried out by means of a specifically developed finite-volume code. Successive bifurcations of the low-Ra fixed point solution are followed for increasing Ra. To this aim, time series of the state variables (velocity components and temperature), are extracted in 5 locations represented in Fig. 1 by points P1 to P5. Nonlinear dynamical features are described by means of phase-space representations, power spectra of the computed time series, and of Poincaré maps.

2 Problem statement and methods

The problem is stated in terms of the incompressible Navier-Stokes formulation, under the Boussinesq approximation. The governing equations (continuity, momentum and energy) are tackled in their non-dimensional form:

$$\nabla \cdot \mathbf{u} = \mathbf{0} \tag{1}$$

$$\frac{\partial \mathbf{u}}{\partial t} + \mathbf{u} \cdot \nabla \mathbf{u} = -\nabla p + \frac{Pr^{1/2}}{Ra^{1/2}} \nabla^2 \mathbf{u} + T\hat{\mathbf{g}} \tag{2}$$

$$\frac{\partial T}{\partial t} + \mathbf{u} \cdot \nabla T = \frac{1}{(RaPr)^{1/2}} \nabla^2 T \tag{3}$$

where t, $\mathbf{u}$, p and T represent the dimensionless time, velocity vector, pressure and temperature, respectively, and $\hat{\mathbf{g}}$ is the gravity unit vector. A value $Pr = 0.7$ is assumed for air. Boundary conditions for T and $\mathbf{u}$ are reported in Fig. 1.

Detailed descriptions of the adopted numerical techniques and of discretization choices are found in previous works [5,7]. A detail of the computational grid is shown in Fig. 1. In order to analyze the system dynamics in the vicinity of bifurcation points, Ra was increased monotonically with suitable steps, each simulation starting from the final frame of the preceeding one. All the simulations were protracted until a fixed dimensionless time span was covered, large enough for an asymptotic flow to be attained.

3 Results and discussion

In previous studies [5,6] a preliminary analysis of the system with $A = 2.5$ reported the birth of chaotic behaviours for Ra greater than $Ra = 2.0 \cdot 10^5$. In particular, power spectral density distributions, attractor representations and

Poincaré maps were used to give a clear evidence of a basic period doubling route to chaos. In particular, it was shown that the flow is characterised by two fundamental harmonics at $Ra = 1.7 \cdot 10^5$, four harmonics at $Ra = 1.8 \cdot 10^5$ and eight at $Ra = 1.9 \cdot 10^5$, whereas chaos was observed at $Ra = 2.0 \cdot 10^5$.

Given the great theoretical and practical importance of an accurate determination of the bifurcating behaviour of the flow, deeper analyses have been performed by refining the step of numerical simulation of the range of interest of the Rayleigh number. As described in the following, two main results have been obtained: (i) the identification of a window of quasiperiodic flow; (ii) the identification of three further period doublings preluding appearance of chaos.

3.1 Window of quasiperiodic flow

Several simulations performed in the range $Ra = 1.7 \div 1.9 \cdot 10^5$ have been found to be characterised by a well defined quasiperiodic behaviour. Again, the observation of this result has been performed both in the frequency domain and in the state space.

Fig. 2 reports the PSDs of the variables simulated at point P1 for the case at $Ra = 176875$, in (a) for the horizontal velocity component u, in (b) for the vertical velocity component v and in (c) for the temperature T.

The following interesting observations can be drawn from the analysis of the three plots of Fig. 2:

- the PSDs of v and T are mainly the same, as a consequence of the vertical character of the buoyancy-driven flow that determines the dynamics of the thermal and velocity field;
- the quasiperiodic behaviour finds a clear expression in the excitation of two independent frequencies, reported in the figures, and of bands formed by their linear harmonic combinations;
- the two dominant frequencies of v and T, exactly double those of the horizontal velocity u, as a direct consequence of the vertical symmetry of the domain.

Fig. 3 reports the phase plots for the simulation at point P1 for the case at $Ra = 176875$, i.e. for the same quasiperiodic dynamic discussed in Fig. 2. Plot (a) reports the whole toroidal attractor, whereas plot (b) allows for a deeper observation of the narrow toroidal structure of the attractor itself. Finally, plots (c), (d) and (e) reports the Poincaré map obtained by sectioning the attractor with the planes orthogonal to each of the axis in correspondence of the mean value of respective variable in the considered observation window. From the analysis of the plots in Fig. 3 it is possible to draw a further clear proof of the existence of the quasiperiodic behaviour, manifested in the state space by the torus and in the Poincaré maps by the elliptical traces. Notice that in plot (c) two partly superimposed elliptical

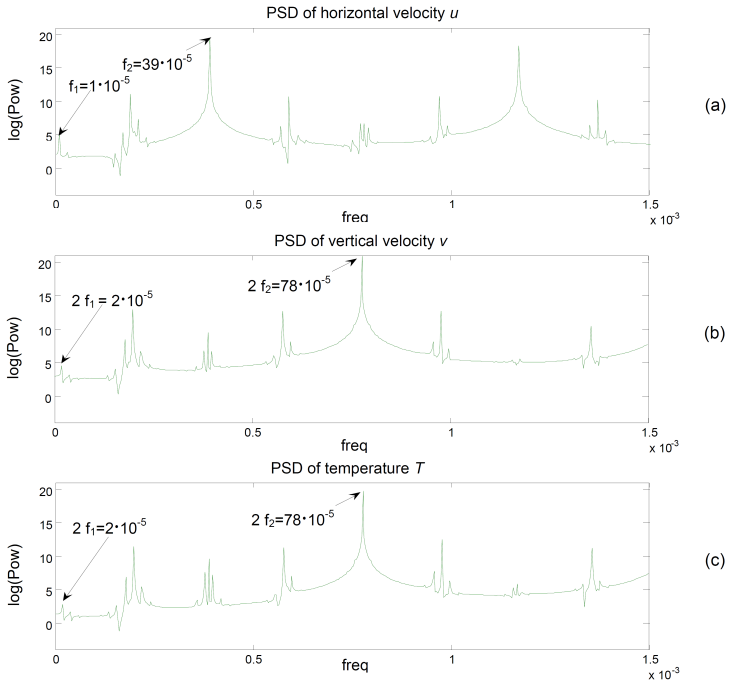

Fig. 2. PSDs of the simulated state variables at point P1 for the quasiperiodic case at $Ra = 176875$: (a) horizontal velocity u; (b) vertical velocity v; (c) temperature T.

traces appears as a consequence of the intersection of the two branches of the torus in the chosen Poincaré plane.

It is worthy to mention that further analyses, omitted here for brevity, revealed that the quasiperiodic torus appears $Ra = 1.740 \cdot 10^5$, bifurcating from the stable limit cycle which represents the solution at $Ra = 1.735 \cdot 10^5$, while it disappears, for $Ra = 1.795 \cdot 10^5$, giving rise to the period-doubling route described in the following. Such observations contribute to shed light on the proper bifurcation path in the range $Ra = 1.740 \div 1.795 \cdot 10^5$, which therefore redefines the simple period doubling assumed in [6].

3.2 High order period doublings

A further refinement of the Ra steps of the simulation in the range $Ra = 1.9 \div 2.0 \cdot 10^5$ allowed for the determination the critical values of Ra at which higher order period doublings occur. In particular, the progressive increase from $Ra = 1.8 \cdot 10^5$, for which a period 8 limit cycle exists, it has been possible to determine the birth of the limit cycles characterised by 16, 32, 64 and even 128 periods, which anticipate the appearance of chaos.

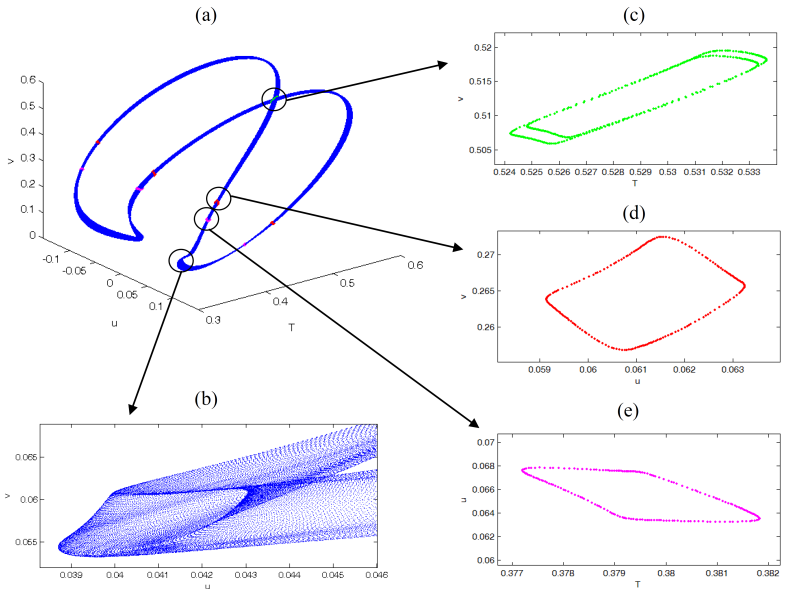

Fig. 3. Phase plots of the quasiperiodic dynamical behaviour at point P1 for $Ra = 176875$: (a) attractor in the state space T-u-v; (b) particular evidencing the structure of the narrow torus; (c), (d), (e) Poincaré maps.

From the analysis of the extensive simulations performed for very narrow step of Ra in the range $Ra = 1.9 \div 2.0 \cdot 10^5$, completed with the observation of the window of quasiperiodic behaviour, it has been possible to summarise the complete bifurcation path from period-2 limit cycle to chaos according to the limits reported in Tab. 3.2. There, the notation introduced in [3] is used to identify the different flow regimes.

	P_1	QP_2	P_2	P_4	P_8
$Ra \cdot 10^{-5}$	≤ 1.735	$1.74 \div 1.79$	$1.795 \div 1.8975$	$1.898 \div 1.9367$	$1.93675 \div 1.94730$
	P_{16}		P_{32}	P_{64}	N
$Ra \cdot 10^{-5}$	$1.94735 \div 1.9495$		$1.94955 \div 1.94985$	1.9499	> 1.95

Table 1. Sequence of flow regimes encountered and correspondent ranges of Ra.

Fig. 4 reports the Poincaré maps for some characteristic values of the Rayleigh number falling within the ranges of limit cycles of high-order period (from P_4 to P_{64}) as well as for one value in the chaotic range, $Ra = 1.9625 \cdot 10^5$. In each map it is possible to observe the existence of four clusters of points, each of which can be considered generated by the four intersections of the original P_1 limit cycle existing for $Ra \leq 1.735 \cdot 10^5$. In order to achieve a deeper detail on the phenomenon, the encircled clusters in Fig. 4 are reported

in Fig. Fig. 5, where the series of doubling of each point can be better observed. As a final remark, it is possible to observe that the period doubling bifurcation path is responsible for the birth of bands in the chaotic attractor, characterised by a marked attitude to stretching and folding typical of fractal sets, as it can be deduced by the ordered distribution of the intersections in the Poincaré maps.

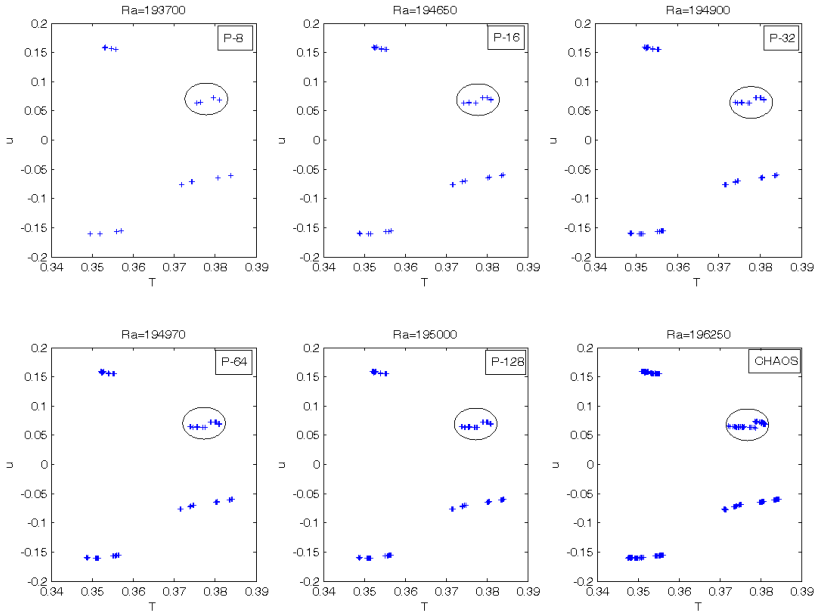

Fig. 4. Poincaré maps for characteristic Ra-values, for limit cycles of high-order period (from P_4 to P_{64}) and chaos.

4 Concluding remarks

The sequence of bifurcations leading to deterministic chaos in natural convection from a horizontal cylindrical source, centred in a square enclosure of aspect ratio $A = 2.5$, was analysed in detail by numerical means.

The set of long term simulations revealed further remarkable aspects of the route to chaos of the system, for increasing the main parameter Ra. In first instance, a window of quasiperiodic behaviour was observed over a wide range of Ra-values, originating from the first limit cycle and giving rise to the subsequent the period-doubling cascade.

Furthermore, the refinement of the parameter range allowed for the detection of additional stages in the sequence of period doublings of the system, up to the observation of a P_{64} orbit, before the final appearance of chaos.

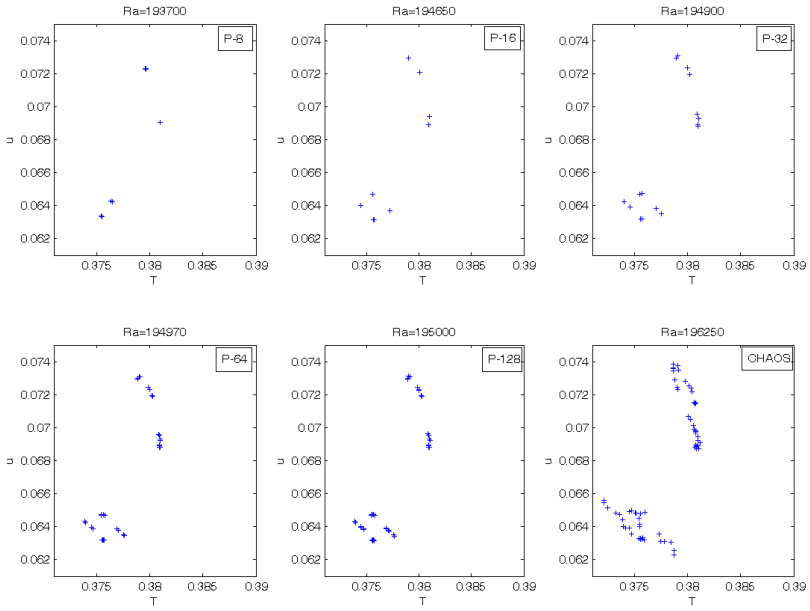

Fig. 5. Details of the encircled clusters of points in the Poincaré maps of Fig. 4.

References

1.K. T. Yang. Transitions and bifurcations in laminar buoyant flows in confined enclosures. ASME *Journal of Heat Transfer*, 110:1191–1204, 1988.

2.P. Le Quéré. Onset of unsteadiness, routes to chaos and simulations of chaotic flows in cavities heated from the side: a review of present status. In G. F. Hewitt, editor, *Proceedings of the Tenth International Heat Transfer Conference*, volume 1, pages 281–296, Brighton, UK, 1994. Hemisphere Publishing Corporation.

3.D. Angeli, G. S. Barozzi, M. W. Collins, and O. M. Kamiyo. A critical review of buoyancy-induced flow transitions in horizontal annuli. *International Journal of Thermal Sciences*, 49:2231–2492, 2010.

4.G. Desrayaud and G. Lauriat. Unsteady confined buoyant plumes. *Journal of Fluid Mechanics*, 252:617–646, 1998.

5.D. Angeli, A. Pagano, M. A. Corticelli, A. Fichera, and G. S. Barozzi. Bifurcations of natural convection flows from an enclosed cylindrical heat source. *Frontiers in Heat and Mass Transfer*, 2:023003, 2011.

6.D. Angeli, A. Pagano, M.A. Corticelli, and G.S. Barozzi. Routes to chaos in confined thermal convection arising from a cylindrical heat source. *Chaotic Modeling and Simulation*, 1:61–68, 2011.

7.D. Angeli, P. Levoni, and G. S. Barozzi. Numerical predictions for stable buoyant regimes within a square cavity containing a heated horizontal cylinder. *International Journal of Heat and Mass Transfer*, 51:553–565, 2008.

On the introduction of internal variables in self-organized critical models for earthquakes

Markos Avlonitis

Department of Informatics, Ionian University, Corfu, Greece
E-mail: avlon@ionio.gr

Abstract: The paper elaborates on a recent self-organized critical (S.O.C.) model for stick-slip motion of fault planes incorporating material and process non-uniformities during earthquakes by means of internal variables. A general theoretical framework for earthquake constitutive equations is given by means of stochastic differential equations. Within the context of the proposed framework a model where shear strength, interpreted as an internal variable, is spatially evolved is also elaborated. In order to study the dynamic behavior of the proposed model a discrete automaton was built validating the robustness of the proposed model. Indeed, simulation results are also demonstrated reproducing correctly experimentally observed quantitative measures during earthquakes. More specifically it is demonstrated that the model address in a robust way the reported b values of the Richter-Gutenberg power law for pre-shocks.

1. Introduction

The understanding of earthquake dynamics as well as the possibilities for the prediction or forecasting of strong earthquakes by means of precursor events macroscopically detected in seismological signals remains a challenging topic in the area of seismology in the last decades (Jordan and Jones, 2010). More specifically, the particular role of the b-value changes, in the magnitude-frequency or G-R relation (Gutenberg and Richter, 1944) for foreshocks has been underlined by several authors (Papazachos, 1975, Jones and Molnar, 1979, Molchan et al., 1999, Papadopoulos et al., 2009). Indeed, observations on seismic sequences have shown that the b-value usually drops and becomes significantly lower in foreshocks. This crucial seismological parameter b, however, seems to be a constitutive-like variable dependent on a variety of local seismotectonic conditions, such as the material heterogeneity, the mode of stress distribution, that is either symmetrical or asymmetrical, and on the existence or not of asperities in the fault zone.

In another issue, it has been proposed that the b-value can be used as an indicator of the type of the structure of the active zone and more precisely of the possible asperities pattern located there (e.g., Zhao and Wu, 2008). As will be discussed latter this is indeed the case since the asperities pattern defines the actual real contact area within the fault zone and it seems that there is a connection between the real contact area and the value of the b exponent.

In this paper a general theoretical framework for earthquake constitutive equations is outlined. In detail, we propose the introduction of appropriate internal variables by means of stochastic differential equations in order to construct more accurate models for the mechanical behavior of earthquake sources. While this framework is introduced and demonstrated in the next two

sections an automaton incorporating shear strength as an internal variable is given in Section 4 where some first simulation results validating the proposed model are also given. In the same section, a discussion about open problems concerning the evolution of earthquake sources is also presented.

2. Proposed framework for earthquake constitutive equations

Let us consider a fault deforming in pure shear. The following constitutive equation for the rate of slip is assumed,

$$\mu\, \partial\gamma/\partial t = \tau_{ext} - \tau_{int} \qquad (1)$$

where τ_{ext} is the externally applied stress resolved in the slip direction and τ_{int} is the total local internal stress exerted.

The external stress τ_{ext} may be assumed constant over the space coinciding with the long-term loading of the tectonic plates. Some other external macroscopic sources of stresses may also be modeled here with this term, as will be shown later. On the other hand, the local internal stress exerted at the location x, quite general, may depend on the space x, the local deformation γ as well as the corresponding rate $\dot{\gamma}$. As a milestone of this work we proposed that the dependency of local stresses to the aforementioned material properties and deforming conditions may be attributed to the existence and evolution of appropriate internal variables. To this end Eq. 1 can be generalized as follows (here the formalism is presented for the 1-D while generalization to higher dimension is straightforward),

$$\mu\, \partial\gamma/\partial t = \tau_{ext} - \tau_{int}(x, \gamma, \dot{\gamma}) \qquad (2)$$

We further assume that internal stresses are made up by three contributions,

$$\tau_{int}(x, \gamma, \dot{\gamma}) = \tau_S(\gamma, \dot{\gamma}) + \tau_{int}^{d}(x, \gamma, \dot{\gamma}) + \tau_{int}^{st}(x, \gamma, \dot{\gamma}) \qquad (3)$$

The first term on the right-hand side of this equation accounts for the resistance of deformation because of the material shear strength which in general may be deformation or/and velocity depended interpreted here as internal variables. The second and third term accounts for the internal stresses arising because of the specific interactions between material points and are divided into a deterministic and a stochastic part. As a result the initial evolution equation becomes a stochastic differential equation where for the random fluctuating part $\tau_{int}^{st} = \delta\tau$ we may write quite general, $\langle \delta\tau \delta\acute{\tau} \rangle = \langle (\delta\tau)^2 \rangle f\left(\frac{x-\acute{x}}{x_{corr}}\right) g\left(\frac{\gamma-\acute{\gamma}}{\gamma_{corr}}\right)$ where $\langle (\delta\tau)^2 \rangle$ defines the amplitude of the stress fluctuations and $\gamma_{corr}\,(x_{corr})$ is the characteristic strain (space) interval over which such fluctuations persist (Zaiser and Aifantis, 2003).

While the nature and the role of the stochastic term will be analyzed elsewhere here we focus on the role of the remaining deterministic terms. The deterministic part of the internal stresses may be modeled by a second order gradient (1-D) and a term modeling linear hardening, i.e.,

$$\tau_{int}^{d} = H\gamma - c\frac{\partial^2\gamma}{\partial x^2} \qquad (4)$$

where H is a hardening coefficient.
In the rest of the section the robustness of the proposed framework is demonstrated by mapping older models within its context. To this end we note that stresses and forces coincide if a unit space element is assumed. The same holds for the strains γ and displacements $u = x - x_0$. The well known one dimension Burridge and Knopoff slider-block model (Burridge and Knopoff, 1967) can be mapped within the proposed framework assuming that the upper tectonic plate is moving with constant velocity and as a result the external stress per unit time takes the form, $\tau_{ext} = K_L v$ where K_L is the elastic constant in the vertical direction within the fault plane. More over if next neighborhood interaction between material points is assumed, Eq. (4) may be derived with $c = K$ where K is the elastic constant in the vertical direction within the fault plane. Finally, Burridge and Knopoff had introduced a velocity weakening friction. In our context this reads (in the simplest form), $\tau_S(\gamma, \dot{\gamma}) \equiv \tau_S(\dot{\gamma}) = F_{crit} - f\dot{\gamma}$. Substituting in the initial constitutive equation,

$$\mu\,\partial\gamma/\partial t = K\frac{\partial^2\gamma}{\partial x^2} + K_L v - H\gamma - F_{crit} + f\dot{\gamma} \qquad (5)$$

and as a result the BK model is fully reconstructed.

In the same line, the Olami Feder Christensen model (Olami et al., 1992) can also be reconstructed noting that essentially is a 2-D version of the BK model, with constant friction law, i.e., $\tau_{int}^{d} = -c(\frac{\partial^2\gamma}{\partial x^2} + \frac{\partial^2\gamma}{\partial y^2})$, with $c = K$ and $\tau_S(\gamma, \dot{\gamma}) \equiv \tau_S = F_{crit}$. Substituting (for the isotropic case),

$$\mu\,\partial\gamma/\partial t = K\left(\frac{\partial^2\gamma}{\partial x^2} + \frac{\partial^2\gamma}{\partial y^2}\right) + K_L v - H\gamma - F_{crit} \qquad (6)$$

The model proposed by Dieterich (1994) introduces the notion of the rate- and state- dependent friction mechanism. According to this mechanism, the coefficient of friction is given as a function of the slip rate as well as of a state variable θ that accounts for the history of sliding. As a result, within the proposed context, the corresponding friction must be written in the form (A and B are constants),

$$\tau_S(\dot{\gamma}, \theta) = F_{crit}^{0} + Aln\dot{\gamma} + Bln\theta \qquad (7)$$

The model proposed by Hainzl and co-workers introduce a transient creep mechanism in order to explain the observed spatio-temporal clustering accompanying earthquakes (Hainzl et al., 1999). This has the consequence that in the inter-occurrence time interval between successive earthquakes, the stresses increase according to the tectonic loading τ_{ext}^{load} and additionally according to the transient creep τ_{ext}^{creep} in the crust. In the proposed framework this is translated as,

$$\tau_{ext} = \tau_{ext}^{load} + \tau_{ext}^{creep} \quad (8)$$

In this work a simple creep law was adopted, $\tau_{ext}^{creep} = \eta\dot{\gamma}$, where η is the corresponding viscous coefficient. The final evolution equation reads,

$$\mu\,\partial\gamma/\partial t = K\frac{\partial^2\gamma}{\partial x^2} + K_L v - H\gamma + \eta\dot{\gamma} - F_{crit} \quad (9)$$

3. Shear strength as an appropriate internal variable

The model first presented in (Avlonitis and Tassos, 2010) introduce the shear strength as an internal spatially evolving variable, i.e.,

$$\tau_S(\gamma,\dot{\gamma}) \equiv \tau_S(\gamma, x) = \tau_S^0 + K'\frac{\partial^2\gamma}{\partial x^2} \quad (10)$$

where the gradient coefficient $K' = c\lambda$ is expressed as a function of the microstructural heterogeneity of the source (here the coefficient c) as well as of the source processes (hardening or softening modeled here by means of the positive or negative value of the coefficient λ) taking places during an earthquake. Substituting in the initial evolution equation,

$$\mu\,\partial\gamma/\partial t = K\frac{\partial^2\gamma}{\partial x^2} + K_L v - H\gamma - \tau_S^0 - K'\frac{\partial^2\gamma}{\partial x^2} \quad (11)$$

or,

$$\mu\,\partial\gamma/\partial t = (K - K')\frac{\partial^2\gamma}{\partial x^2} + K_L v - H\gamma - \tau_S^0 \quad (12)$$

Eq. (12) is of crucial importance since it redresses the generic weakness of the OFC model. In fact, it introduces the effect of structural softening into the corresponding constitutive equation and through it to macroscopic measured quantities such that the b value of the Richter-Gutenberg power law.

4. Simulation results and Discussion

A variation of the classic OFC simulator was constructed under the line of reasoning present in the previous section, i.e., to model structural softening. As was discussed in the introduction, structural softening is believed that takes place before an earthquake occurs, i.e. during pre-socks. It is also known that

during pre-shocks a reduction of the b value of the Richter-Gutenberg relation occurs (Papadopoulos et al., 2009).

It is our aim to reproduce these macroscopic findings via simulations of the proposed model. To this end we mimic structural softening by introducing within the simulated fault plane sites with lower shear strength, as is assumed in Eq. 10 for negative values of the parameter lambda λ, hereafter called soft phase. As the structural softening proceeds the soft phase gradually increases. The degree of structural softening is measured as the percentage of the soft phase within the simulated fault plane. Initial results are shown in Fig. 1, reproducing correctly the macroscopic observations for the slope of the Richter-Gutenberg power law. Indeed, as depicted in Fig. 1, as the percentage of the soft phase within the fault plane is increased the b value decreases. This means that as the material enters deeper in the softening regime the slope within the linear regime of the Richter-Gutenberg power law (in log-log plot) decreases.

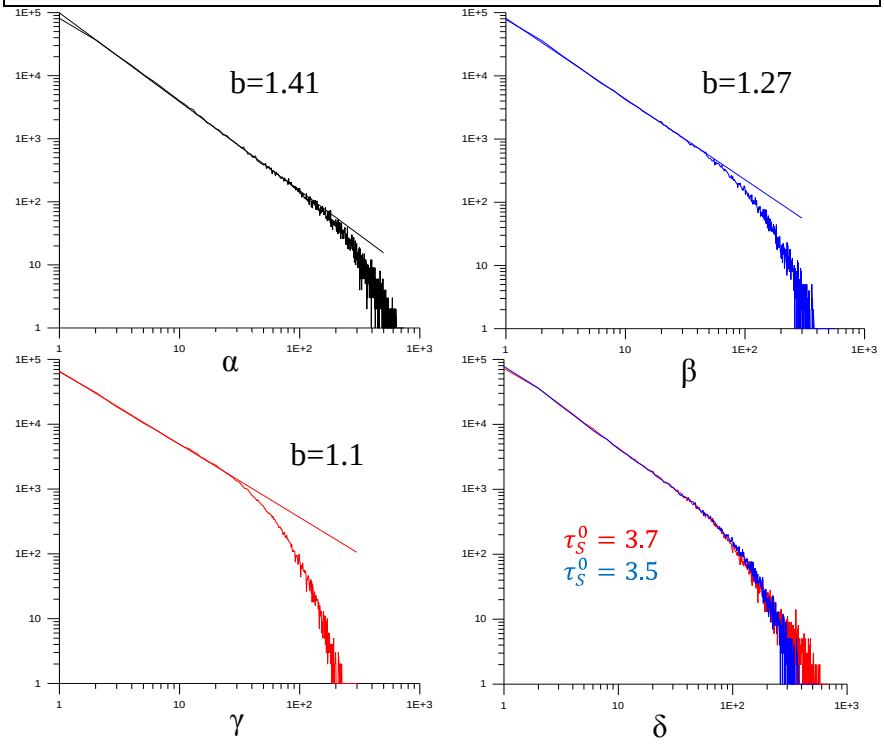

Fig.1 Decreasing b values as the percentage of the soft regions increases. Results are depicted for a 30x30 lattice and for 0%, 20% and 40% soft phase (α, β, γ). In (δ), the independence on the exact value of the shear strength within the soft phase is depicted.

It is noted that the main scope of the present work is to introduce a general robust framework for earthquakes constitutive models. Moreover, we believe that relaxing the assumption of constant shear strength and interpreted it as an internal variable that is spatially evolve we can correctly reproduce seismological observations during earthquakes. To this end we have shown in this paper that spatially evolving shear strength predicts well known findings concerning pre-shock sequences and more specifically the corresponding variations of the macroscopic b value. Of course there are a series of phenomena inextricably linked with earthquakes, e.g. asseismic slip which are still missing from the "picture". It is our aim to show in a series of forthcoming papers how the assumption of spatially evolve shear strength may correctly model these phenomena. Moreover, the spatially evolving shear strength may serve as the appropriate constitutive variable to model the real contact area between lithospheric zones. Indeed, it can be shown that due to asperities the real contact area is not a constant quantity and is a crucial parameter that affects the macroscopic earth behavior. Most importantly, what is missing is a specific mechanism which results to spatially evolving shear strength and which reproduces a non-convex hardening-softening law for the fault plane. Again this is the topic for a future paper where the existence of liquids within the interface of lithospheric zones may explain the proposed shear strength behavior. Finally, in the series of the above mentioned forthcoming papers the origin of the spatial (evolving) and stochastic terms is investigated revealing their interconnecting nature.

Acknowledgement

This work was supported by the project S.M.ART. BUIL.T. (European Territorial Cooperation Programme, Greece-Italy, 2007 - 2013) by the European Commission.

References

1. Avlonitis, M. and Tassos, S. (2010), Towards realistic self-organized critical models for earthquakes, ESC 2010, Montpellier, France.
2. Burridger, R., and Knopoff, L. (1967), Model and theoretical seismicity, Bull Seismol. Soc. Am. 57, 341-371.
3. Gutenberg, B. and Richter, C. (1944), Frequency of earthquakes in California, B. Seismol. Soc. Am., 34, 185–188.
4. Hainzl, S., Zoller, G. and Kurths, J. (1999), Similar power laws for foreshock and aftershock sequences in a spring-block model for earthquakes, J. Geophys. Res. 104, 7243-7253.
5. Jones, L.M. and Molnar, P. (1979), Some characteristics of foreshocks and their possible relationship to earthquake prediction and premonitory slip on faults, J. Geophys. Res., 84, 3596–3608.

6. Jordan, T. and Jones, L. (2010), Operational Earthquake Forecasting: Some Thoughts on Why and How, Seismol. Res. Lett., 81, 571–574.
7. Molchan, G.M., Kronrod, T.L. and Nekrasona, A.K. (1999), Immediate foreshocks: time variation of the b-value, Phys. Earth Planet. Int., 111, 229–240.
8. Olami Z., Feder, HJS. and Christensen, K. (1992), Self-organized criticality in a continuous, nonconservative cellular automation modeling earthquakes, Phys. Rev. A 46, 1720-1723.
9. Papadopoulos, G.A., Charalampakis, M., Fokaefs, A. & Minadakis, G., 2009. Strong foreshock signal preceding the L'Aquila (Italy) earthquake (Mw 6.3) of 6 April 2009, Natural Hazards & Earth System Science, 10, 19–24.PAPAZACHOS, B. C. (1975), Foreshocks and earthquake prediction, Tectonophysics, 28, 213–226.
10. Zaiser, M. & Aifantis, E.C., 2003. Avalanches and slip patterning in plastic deformation, J. Mech. Behavior Mater., 14, 255–270.
11. Zhao, Y. Z. & Wu, Z. L., 2008. Mapping the b-values along the Longmenshan fault zone before and after the 12 May 2008, Wenchuan, China, Ms 8.0, earthquake, Nat. Hazards Earth Syst. Sci., 8, 1375-1385.

Proceedings, 5th Chaotic Modeling and Simulation International Conference, 12 – 15 June 2012, Athens Greece

Stability and Chaos in a Classical Yang – Mills - Higgs System

O. Ozgur Aybar[†•], Avadis S. Hacinliyan[†‡], Ilknur Kusbeyzi Aybar[*], Kamer Koseyan[‡], Berc Deruni[‡]

[†]Yeditepe University, Department of Information Systems and Technologies, Istanbul, Turkey
[‡]Yeditepe University, Department of Physics, Istanbul, Turkey
[*]Yeditepe University, Department of Computer Education and Instructional Technology, Istanbul, Turkey
[•]Gebze Institute of Technology, Department of Mathematics, Kocaeli, Turkey
E-mail: oaybar@yeditepe.edu.tr
E-mail: ahacinliyan@yeditepe.edu.tr
E-mail: ikusbeyzi@yeditepe.edu.tr
E-mail: kaderci.johannes@gmail.com
E-mail: berc_890@hotmail.com

Abstract: A motivation for looking at chaos in the classical realizations of the Yang-Mills or Yang Mills augmented by Higgs equations is the importance of this system in the initial (in)stability at big bang, since in the initial stages all interactions were of the same strength and were based on non abelian gauge theories, of which the SU(2) Yang Mills is a first example.
In this study we consider the following two particle effective Hamiltonian suggested by Biro, Matinyan and Müller:

$$H = \frac{{p_x}^2 + {p_y}^2}{2} + \frac{1}{2}x^2y^2 + \frac{1}{2}(a^2x^2 + b^2y^2) + \frac{1}{2}x^4 + \frac{1}{4}py^4$$

Keywords: Dynamical systems, Yang-Mills, Lyapunov exponents, Chaos.

1. Introduction

Global properties for mappings such as Poincare sections, Lyapunov exponents and other topological properties as introduced by Poincare and Birkhoff are important objects of study in nonlinear dynamical systems in addition to their local properties such as various bifurcations and invariant manifolds[1].
As Matinyan suggested, one of the ways to search for chaos is to investigate Poincare sections[4,5,6]. Since the system is described by a time independent Hamiltonian, the energy integral reduces the four dimensional system into a three dimensional system and a two dimensional Poincare map[1,2,3]. Unfortunately, the Hamiltonian involves the squares of the momentum. Taking the square root leads to missing information since the trajectory should cross into regions where the momentum can have either sign. There are two ways known to solve this problem. One of the solutions to this problem is the symplectic numerical integration technique and the other one is to check the

energy conservation numerically at every point. Results of these investigations lead to the same results obtained by KAM (Kolmogorov–Arnold–Moser) theory and hence this numerical study is proven to be an indicator for chaos.
If the system is integrable, the trajectory is closed. Hence a torus is obtained. If the system is not integrable, elliptic orbits are observed with a chaotic regime. According to KAM theory the invariant tori of an integrable system retain their topology under a perturbation that destroys the integrability of the Hamiltonian, however chaos is observed in some regions of the phase space of the system with random points on the surface of section.
In addition to the Poincare section study done by Matinyan et. al, a Lyapunov exponent study can reveal the parts of the parameter space in which chaos is observed. Preliminary results indicate that for the case in which the Higgs terms (x^4 and y^4) are absent, all regions for the parameters $a>0$ and $b>0$ give positive maximal Lyapunov exponents that indicate chaos For $a = b = 0$, the chaoticity is maximum. As a or b increase, the system is still chaotic, but the system loses its chaoticity gradually and tends to converge to a limit cycle. On the other hand, for the case the Higgs terms are present with $a=b=0$, the system still has a positive maximal Lyapunov exponent whose value is smaller than that in the Yang Mills case.

2. Chaos in Yang Mills Higgs system

Although there is no universally accepted definition of chaos, most experts think that chaos is the aperiodic, long – term behavior of a bounded, deterministic system that exhibits sensitive dependence on the on initial conditions. Lyapunov Exponents is the mathematical method for the determination of chaos in dynamical systems. It is the measure of the exponential separation of two trajectories with a very small initial separation. A system with positive values of Lyapunov Exponents is chaotic, and the value of these exponents the average rate at which predictability is lost.
In this section, we compute Lyapunov exponents with the aid of Fortran code that implement Wolf algorithm as we discussed before. In addition we also use Reduce code which calculates variational equations needed for the Wolf algorithm. Both programs are included in appendixes. We mostly emphasize on Yang Mills Higgs coupled system in order to demonstrate the corresponding chaotic behavior.
First of all we investigated how exponents are changing with respect to the scale parameter p, we found that system possesses chaotic motion in wide range of value of p. Especially we scan for the interval from $p=0.05$ to $p=4$. Here are some of graphs for the specific values of p.

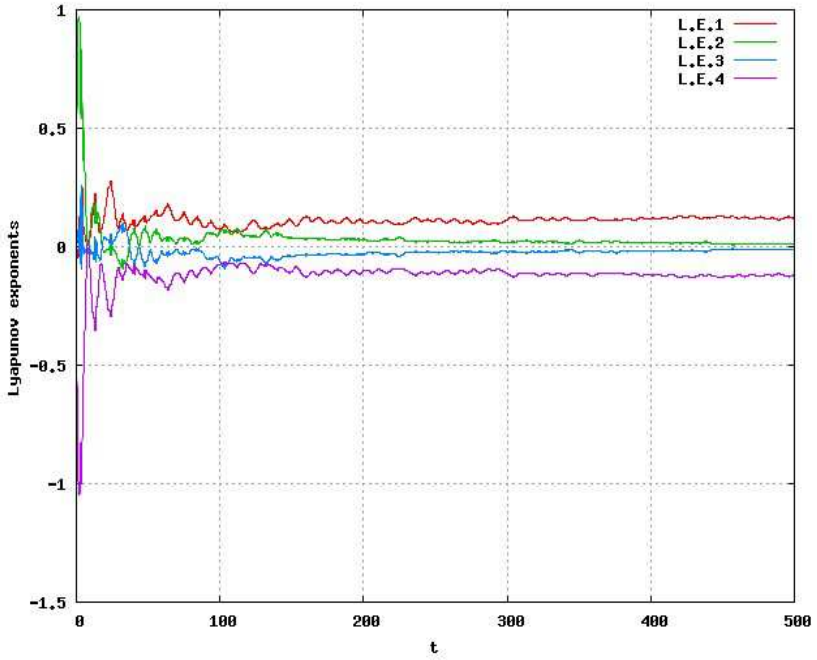

Fig. 1. Lyapunov exponents vs time for *p=0.2*

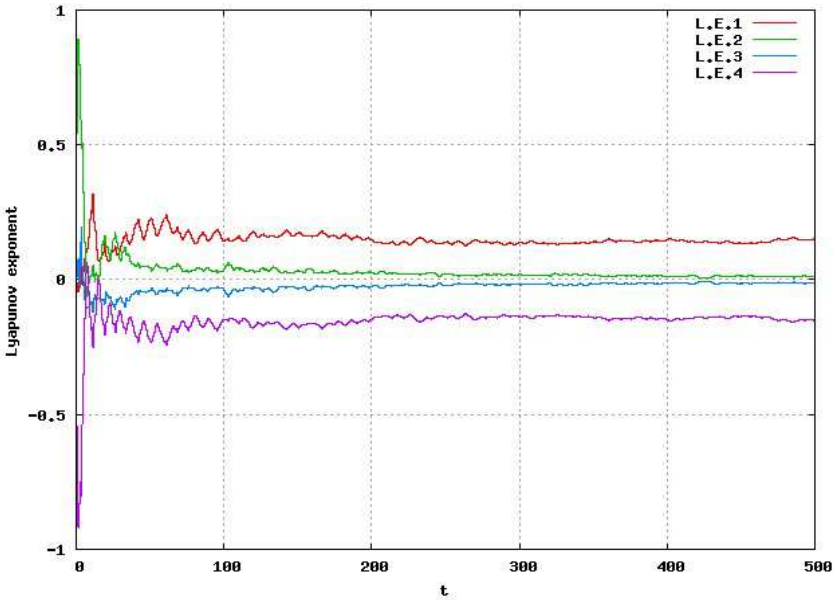

Fig. 2. Lyapunov exponents vs time for *p=0.5*

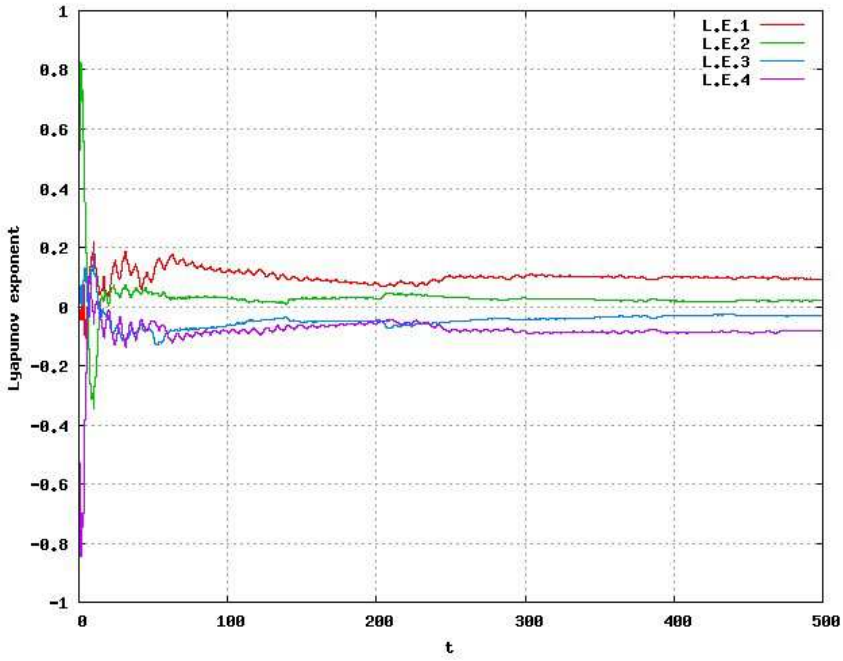

Fig. 3. Lyapunov exponents vs time for *p=0.8*

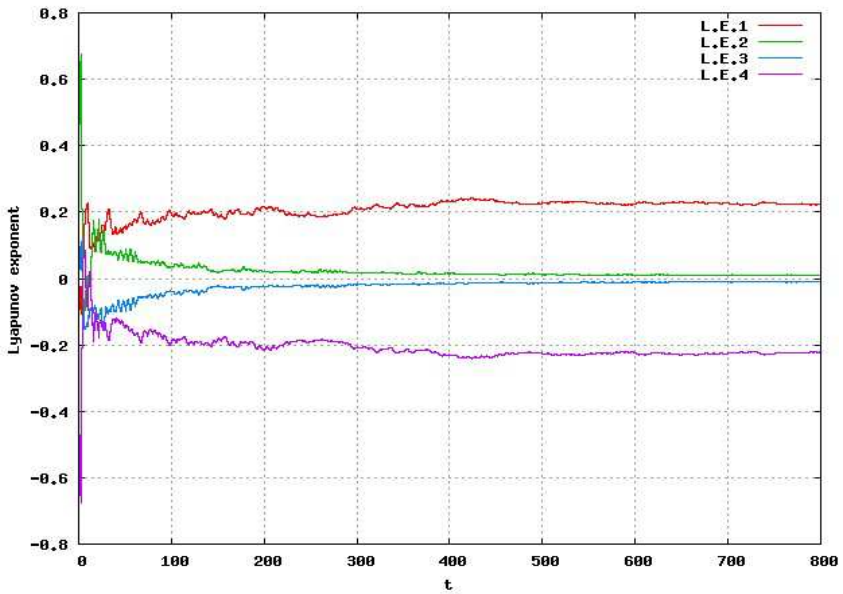

Fig. 4. Lyapunov exponent vs time for *p=2.2*

On the other hand we also analyze the results of adding oscillator term to dynamical system by giving a coefficient "a". We saw that all Lyapunov exponents tend to decrease for bigger value of "a" and there occurs a transition from chaotic motion to periodic or quasi periodic motion. We investigate this transition for the value of parameters where the Lyapunov exponents seem to be maximum. Some of the results are shown below

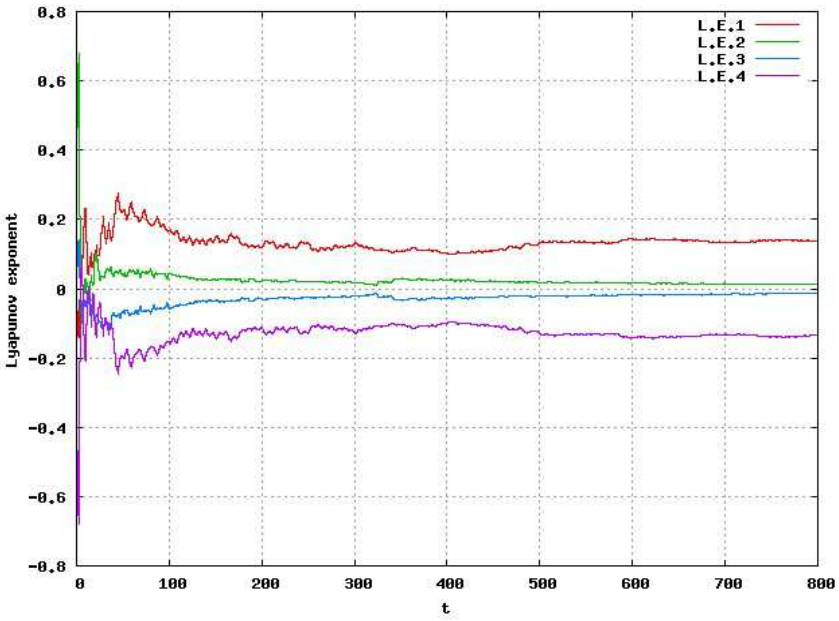

Fig. 6. Lyapunov exponents vs time for *a=0.1* and *p=2.2*

We can deduce from these graphs that, for small values of "*a*" the system persist for a chaotic behavior. But when "*a*" grows system start to possess periodic motion.On the other hand we can see that almost all Lyapunov spectrums are symmetrical which is the expected result since in Hamiltonian systems the sum of Lyapunov exponents must be zero as we stated before so when there is an expanding trajectory in phase space there must be also equally contracting trajectory to compensate for this.

We also investigate phase space trajectories for the corresponding system. Here are some of the trajectories for this system

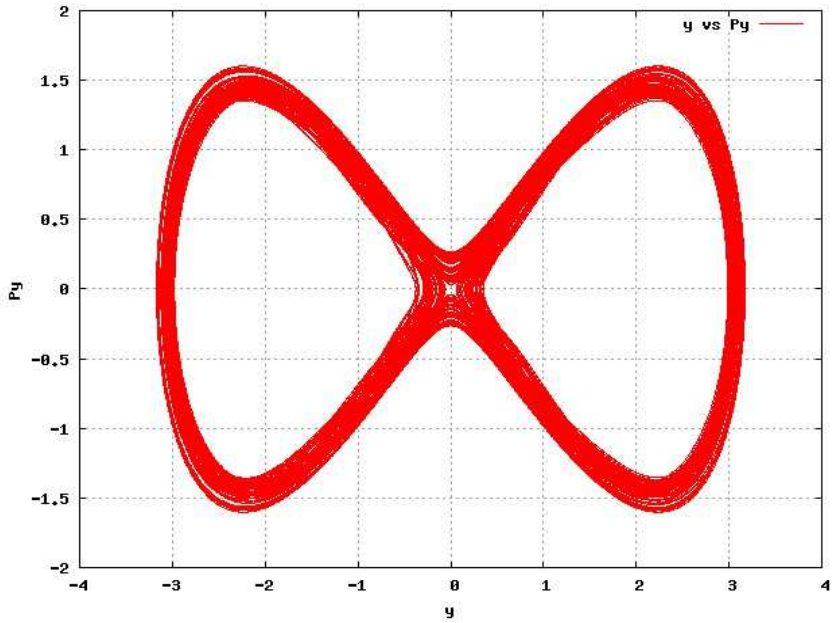

Fig. 7. Trajectory of y vs P_y

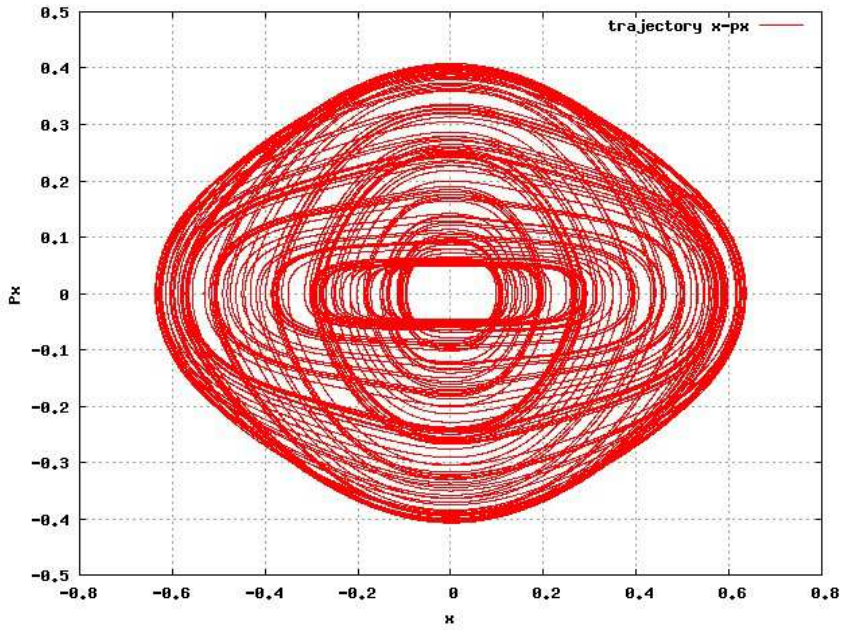

Fig. 8. Trajectory of x vs P_x

3. Conclusions

In this article we try to demonstrate chaotic behavior in the dynamically coupled Yang Mills Higgs system classically. We know that pure Yang Mills fields possess highly chaotic behavior. Although Yang Mills Higgs system also possess chaotic behavior for variety of range of scale parameter, in general the Higgs field is responsible for considerably regularizing motion in the dynamical system[4,6]. So we can say that Higgs mechanism has a stabilizing effect. On the other hand we also consider an additional oscillator term in the Yang Mills Higgs system and it is observed that for small coefficients of the oscillator term chaotic motion still persists. But when oscillator term gets larger chaos disappears and regular motion involving multi periodic motion takes place instead, since the oscillatory motion begins to dominate[5,6].

References

1. A. Wolf, J. B. Swift, H. L. Swinney and J. Vatsano. Determining Lyapunov Exponents From a Time Series. *Physica D,* 16: 285-317,1985.
2. C. H. Skiadas and C. Skiadas. *Chaotic Modeling and Simulation: Analysis of Chaotic Models, Attractors and Forms*, Taylor and Francis/CRC, London, 2009.
3. F. Verhulst. *Nonlinear Differential equations and dynamical systems*, Springer,Verlag, 1996.
4. S. G. Matinyan and B. Müller. *Chaos and Gauge Field Theory*, World Scientific, 1994.
5. S. G. Matinyan. *Chaos in Non-Abelian Gauge Fiels, Gravity and Cosmology*, NC, 1996.
6. S. G. Matinyan. *Dynamical Chaos of Non–Abelian Gauge Field*, Yerevan Physics Institute, 1983.

A New Adaptive Sliding Mode Control Law of Chaotic Systems to Synchronization

Mustafa Resa Becan

Technical University of Istanbul, Turkey
email: becanm@itu.edu.tr

Abstract: In this research, a new adaptive sliding mode control scheme which combines two algorithms mentioned before is introduced to synchronize chaotic Lorenz models and the synchronization of chaos by designing a new method is presented. As the simulations show, the proposed controller is efficient to synchronize chaotic systems and has better performance compared to former methods. These results are obtained from Integral of Squared Sliding Surface Signal and Integral of Squared Sliding Control Signal criteria. Furthermore, the boundary layer is proposed in the new control algorithm to avoid the chattering phenomenon on behaviors.

Keywords: Chaos Syncronization, Lorenz Model, Adaptive, Sliding Mode Control

1. Introduction

Chaos phenomenon is very interesting area in the nonlinear systems described by differential equations which can be extremely sensitive to initial conditions. The concept of controlling and synchronization of chaotic systems have been attracted by researchers since the early 1990s. In recent years, several techniques of chaos control and synchronization have been applied such as linear and nonlinear feedback control [1,2], adaptive control [3-5] and sliding mode control [6-8].

In the past decades, the sliding mode control (SMC) has been effectively applied to control systems with uncertainties because of the nature of robustness of sliding mode [9]. The adaptive techniques have been also applied to control and synchronize chaotic systems [10,11]. Recently, researchers have utilized the adaptive control with sliding mode technique for many engineering systems to decrease the chattering in pure SMC and smooth the output from a sliding mode controller. Dadras and Momeni [12] proposed an adaptive sliding mode control to synchronize master-slave chatotic systems. This scheme reduces the chattering phenomenon and guarantees stability in presence of parameter uncertainties and external disturbance. Roopaei et al. [13] developed an adaptive sliding mode controller to stabilize the novel class chaotic system.

In this research, a new adaptive sliding mode control scheme which combines two algorithms mentioned before is introduced to synchronize chaotic Lorenz models and the synchronization of chaos by designing a new method is presented.

2. System Description and Problem Formulation

Considering system uncertainties a class of the following two *n*-dimensional chaotic systems can be written as:

$$\begin{aligned} &\dot{x}_i = x_{i+1} && 1 \le i \le n-1 \\ &\dot{x}_n = f(x,t) && x = [x_1, x_2, \dots, x_n] \in R^n \end{aligned} \tag{1}$$

$$\begin{aligned} &\dot{y}_i = y_{i+1} && 1 \le i \le n-1 \\ &\dot{y}_n = f(y,t) + \Delta f(y) + u && y = [y_1, y_2, \dots, y_n] \in R^n \end{aligned} \tag{2}$$

Where $u \in R$ is the control input, f is a given nonlinear function of $x, y, t. \Delta f(y)$ is an uncertain term representing the unmodeled dynamics or structural variation of (2).

In this paper, the chaos synchronization is considered as a model tracking problem in which the slave system (2) can track the master system (1) asymtotically. The two coupled system to be synchronized by designing an appropriate control *u(t)* in system (2) such that

$$\lim_{t\to\infty}\|y(t) - x(t)\| \to 0 \quad (3)$$

where $\|.\|$ is the Euclidian norm of a vector. Let us define the error states between (1) and (2) such as:

$$e_1 = y_1 - x_1, \ldots., e_n = y_n - x_n \quad (4)$$

The problem is to realize the synchronization between two chaotic systems is to choose a control law *u(t)* to make error states converge to zero. Here an adaptive sliding mode control design is used to achieve this objective.

3. Design of Adaptive Sliding Mode Control via Synchroziation Problem

To propose a new adaptive control algorithm for synchronization of two chaotic systems are described in (1) and (2), an adaptive switching surface is considered as

$$s(t) = e_n(t) + \varphi(t) \quad (5)$$

Because this surface was considered as in [13] referred study as shown below

$$s(t) = x(t) + \varphi(t) \quad (5a)$$

(5a) was designed for a control problem and we changed it to equation (5) in order to adapt to our synchronization problem and so we obtained (5).

In (5) $e_n(t)$ is the n – dimensional system error state and $\varphi(t)$ is an adaptive function given by

$$\dot{\varphi} = e_i(x,y)e_{i+1}(x,y) + \alpha e_i + \rho e_{i+1} \quad (6)$$

where α and ρ are assumed to be the arbitrary constants. This adaptive function is also from Poopaei study [ ] and here it is adapted to the synchronization problem. When the system operates in sliding mode, it satisfies the following condition:

$$s(t) = e_n(t) + \varphi(t) = 0 \quad (7)$$

Differentiating Eq.(7), leads to the following:

$$\dot{s}(t) = \dot{e}_n(t) + \dot{\varphi}(t) = 0 \quad (8)$$

The equivalent control law can be obtained by utilizing (4) and (8) as shown below:

$$u_{eq} = -f(y,t) - \Delta f(y) + f(x,t) - \dot{\varphi} \quad (9)$$

(The open version of (10) is given in Section 5 as equation (30))

The next step is to design the reaching mode control scheme which drives the system trajectories on to the sliding surface ($s=0$). In the proposed method, we aim to derive a new algorithm combining Dadras and Roopaei methods to increase the control performance. Therefore the overall control signal has the form of following:

$$u(t) = u_{eq} - \gamma\varepsilon(\lambda, s) + k_s sign(s) \quad (10)$$

where $\varepsilon(\lambda, s)$ is a hyperbolic function (Dadras):

$$\varepsilon(\lambda, s) = \tanh(\lambda s) \quad (11)$$

and the Dadras adaptive law is:

$$\dot{\gamma} = m_1 e\varepsilon(\frac{\delta x}{\delta u}) \quad (12)$$

$$\dot{\lambda} = m_2 e(1 - \varepsilon^2)s(\frac{\delta x}{\delta u}) \quad (13)$$

The Roopaei adaptive law in combined overall control signal (10) is:

$$\dot{k}_s = -\mu|s| \quad (14)$$

where μ is a positive constant number.

4. Case Study and Simulation Results

This section of the paper presents the case study to verify and demonstrate the effectiveness of the proposed control scheme. The simulation results are carried out using the MATLAB software. The fourth order Runge-Kutta integration algorithm was performed to solve the differential equations.

Consider the chaotic Lorenz master-slave systems as follows:

$$\begin{cases} \dot{x_1} = a(x_2 - x_1) \\ \dot{x_2} = cx_1 - x_1x_3 - x_2 \\ \dot{x_3} = x_1x_2 - bx_3 \end{cases} \quad (15)$$

and

$$\begin{cases} \dot{y_1} = a(y_2 - y_1) \\ \dot{y_2} = cy_1 - y_1y_3 - y_2 + \Delta f(Y) + u(t) \\ \dot{y_3} = y_1y_2 - by_3 \end{cases} \quad (16)$$

where a,b, c are the positive contants, $\Delta f(y)$ is the uncertainty term and *u(t)* is the adaptive sliding mode control law.

The error states defines as given below

$$e1 = y1 - x1,\ e2 = y2 - x2,\ e3 = y3 - x3 \quad (17)$$

The sliding surface and adaptive funtion are choosen respectively, regarding Eq. (5) and (6):

$$s = e_1 + e_2 + \varphi \quad (18)$$

$$\dot{\varphi} = e_1e_2 + \alpha e_1 + \rho e_2 \quad (19)$$

where α and ρ are the positive constants. The continious part of control law (u_{eq}) is obtained from $\dot{s} = 0$ as shown below:

$$u_{eq} = a(x_2 - x_1) - a(y_2 - y_1) - cy_1 + y_1y_3 + y_2 + cx_1 - x_1x_3 - x_2 - (e_1e_3 + ae_1 - e_2 + \rho e_2) \quad (20)$$

The simulation is done with the initial value $[x_1\, x_2\, x_3]^T = [7\ 6\ 12]^T$, $[y_1\ y_2\ y_3]^T = [10\ 10\ 10]$ and system parameters are a=10, b=$\frac{8}{3}$, c=28. Control parameters for Dadras adaptive law are choosen as $m_1 = m_2 = 5$. In addition the second adaptive law is used to update the k_s, $\dot{k}_s = -0.1|s|$. The slave system is perturbed by an uncertainty term:

$$\Delta f = 0.5 - \sin(\pi y_1)\sin(2\pi y_2)\sin(3\pi y_3)$$

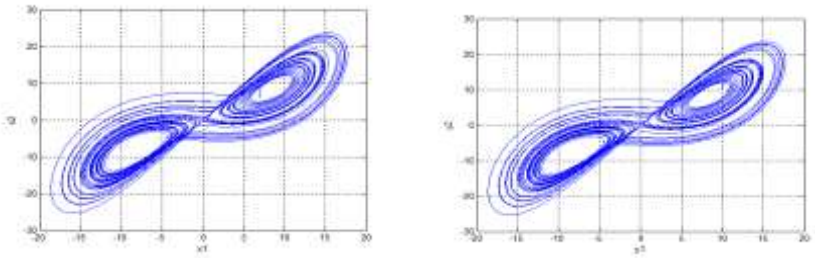

(a) (b)

Fig. 1. Phase Plane of two Lorenz model after synchronization (a) master (b) slave

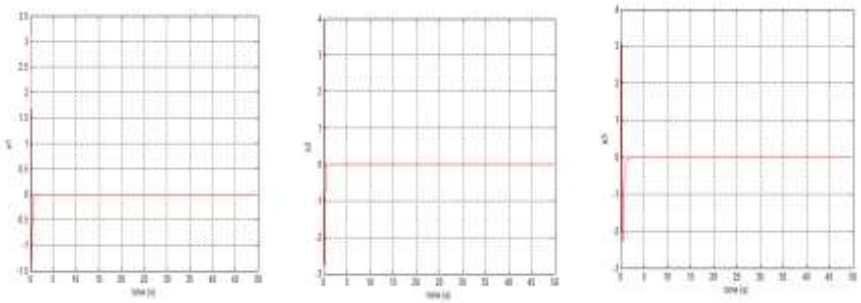

Fig. 2. The Error States

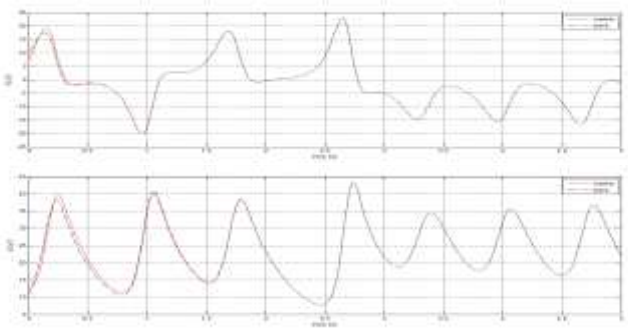

Fig. 3. Synchronization of state variables with proposed control law

Table 1

	Proposed Control	Proposed Control(with boundary layer)	Dadras Control	Dadras Control(with boundary layer)
$\int_0^5 s^2(t)dt$	$0.99.10^{-6}$	$1.05.10^{-5}$	$1.5.10^{-5}$	$1.13.10^{-5}$
$\int_0^5 u^2(t)dt$	1.15	0.2013	0.2544	0.2588

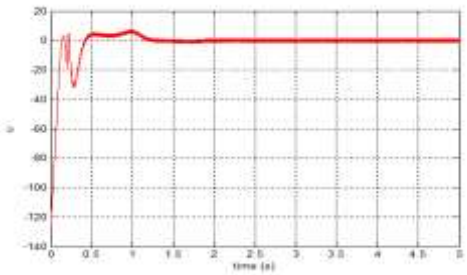

Fig.4. Control input for proposed algorithm without boundary layer

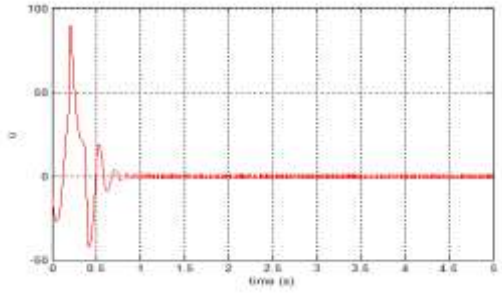

Fig.5. Control input for Dadras algorithm without boundary layer

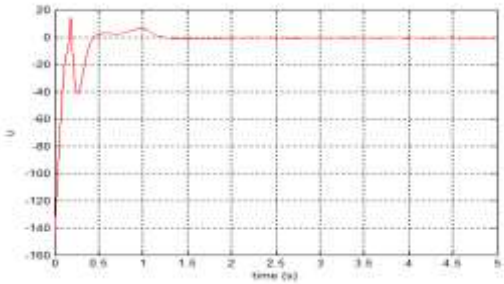

Fig.6. Control input fo rproposed algorithm with boundary layer

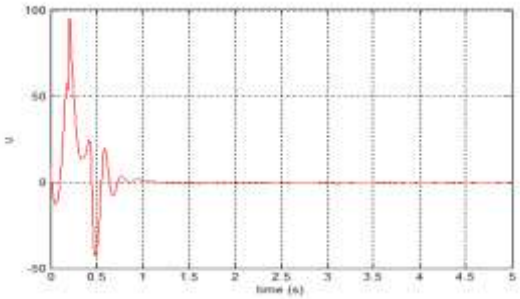

Fig.7. Control input for Dadras algorithm with boundary layer

The first parts of the simulation results are shown in Figs. 1-3 under the proposed adaptive sliding mode control (ASMC). Fig 1. shows the phase plane of master-slave Lorenz systems whereas Fig 2. exhibits the error states and Fig 3. presents the state variables after synchronization after ASMC application. From these results, it can be concluded that the obtained theoretic results are feasible and efficient for synchronizing Lorenz chaotic systems under uncertainty.

In the second part of simulation study, proposed adaptive sliding mode control is compared with Dadras method. "*Integral of Squared Sliding Surface Signal*" and " *Integral of Squared Sliding Control Signal*" criteria are used. Table 1 presents the results. Referring to Table 1 and Figs 4-7, it can be concluded that in the case of using a boundary layer, our combined adaptive sliding mode control scheme can manage better performance compared to Dadras method.

6. Conclusion

This work presents the synchronization of chaos by designing a new adaptive sliding mode controller. As the simulations show, the proposed controller is efficient to synchronize chaotic systems and has better performance compared to Dadras method. These results are obtained from *Integral of Squared Sliding Surface Signal*" and " *Integral of Squared Sliding Control Signal*" criteria. Furthermore, the boundary layer is proposed in the new control algorithm to avoid the chattering phenomenon on behaviors.

References

[1] G.P. Jiang, G. Chen, W.K.S. Tang, A new criterion for chaos synchronization using linear state feedback control, Int. J. Bifurcat. Chaos 13 (2003) 2343–2351.

[2] M. Rafikov, J.M. Balthazar,On control and synchronization in chaotic and hyperchaotic systems via linear feedback control, Commun. Nonlinear Sci. Numer. Simulat. 13 (2008) 1246–1255.

[3] M. Feki, An adaptive feedback control of linearizable chaotic system, Chaos Solitons Fract. 15 (2003) 883–890.

[4] C. Hua, X. Guan, Adaptive control for chaotic systems, Chaos Solitons Fract. 22 (2004) 55–60.

[5] Y.W. Wang, C. Wen, M. Yang, J.W. Xiao, Adaptive control and synchronization for chaotic systems with parametric uncertainties, Phys. Lett. A 372 (2008) 2409–2414.

[6] S. Dadras, H.R. Momeni, Control uncertain Genesio–Tesi chaotic system: adaptive sliding mode approach, Chaos Solitons Fract. 42 (2009) 3140–3146.

[7] S. Dadras, H.R. Momeni, V.J. Majd, Sliding mode control for uncertain new chaotic dynamical system, Chaos Solitons Fract. 41 (2009) 1857–1862.

[8] M. Feki, Sliding mode control and synchronization of chaotic systems with parametric uncertainties, Chaos Solitons Fract. (2008), doi:10.1016/j.chaos.2008.05.022.

[9] W. Perruquetti, J.P. Barbot, Sliding Mode Control in Engineering, Marcel Dekker Inc., New York, NY, 2002.

[10] C. Hua, X. Guan, Adaptive control for chaotic systems, Chaos Solitons Fract. 22 (2004) 55–60

[11] H. Salarieh, M. Shahrokhi, Adaptive synchronization of two different chaotic systems with time varying unknown parameters, Chaos Solitons Fract. 37 (2008) 125–136.

[12] S.Dadras, H.R.Momeni, Adaptive sliding mode control of chaotic dynamical systems with application to synchronization,Mathematics and Computers in Simulation (2010) 2-13.

[13]M.Roopaei, B.R.Sahraei, T.C.Lhin, Adaptive sliding mode control in a novel class of chaotic systems, Commun Nonlinear Sci Numer Simulat (2010) 4158-4170.

Proceedings, 5th Chaotic Modeling and Simulation International Conference, 12 – 15 June 2012, Athens Greece

Rotations-Expansion-Reflections Chaotic Modelling with Singularities in Higher Dimensions

Bernd Binder

Quanics, Salem, Germany
E-mail: binder@quanics.com,

Abstract: Rotation – Expansion – Translation – Reflection chaotic models show despite of its simple generators complex structures that resemble in 2 dimensions - without referring to any material property - well known fluid/flux vortex flow patterns as recently shown by Skiadas. Here the model is generalized and extended to $n > 2$ dimensions with $N = n(n-1)/2$ rotational degrees of freedom and the maximum of $L = n(n-1)(n-2)/2$ singularity rotations on the sphere and hyper sphere with rotation matrix operations given by the orthogonal group O(n), special orthogonal group SO(n), or Lie spin group Spin(n) with hierarchical relations. The radial distance to the singularities located on the rotation axes leads to the Skiadas power law rotation parameterized by a power exponent and rotation strength. Patterns often show characteristic flux lines emitted from a chaotic core near to a singularity. The non-commutative permutations of the non-abelian rotation group elements are relevant for encryption purposes.

Keywords: Chaotic modeling, Discrete map, Rotation-Translation, Rotation-Rotation, molecular interaction, v. Kármán Street, Dipole-dipole, Chaotic simulation, Chaotic encryption, Spin group.

1. Introduction

In quantum physics the spatial probability density and its symmetries are a basic concept to describe the evolution of observables obtained from stochastic (jump) processes in phase space. The Rotation – Expansion – Translation – Reflection pattern generation approach of Skiadas provides also for spatial density structures but from iterative difference equations generating more or less chaotic jumps [1, 2, 3]. The first results of Skiadas are very similar to v. Kármán Streets, see fig. 1, or even elliptic galaxies formations. Since a translation is a special case of a rotation with the rotation centre located at very large distances, applying subsequent rotations repeatedly around different rotation centres should also provide for interesting patterns, especially if the rotations are a function of a spatial distance with respect to one or more singularities, where rotations grow infinite due to a power law with negative exponent. We will focus in this paper onto the rotation-rotation chaotic phase jump processes on hyper spherical loops with larger or smaller chaotic core regions, which depend on characteristic numbers and symmetries. Since the signal $\mathbf{p}_t$ jumps in hyper space or on hyper spheres, the resulting patterns could be relevant to physics and quantum spin groups in higher dimensions [4]. First we will introduce the rotation-translation approach in two dimensions (2-D) with one or more singularities and then replace the translation by another rotation and generalize

to n dimensions on (hyper) spherical surfaces. After generating some new chaotic jump pattern by extending the Skiadas algorithm and relate it to proper physics attributes, some new input came from discussions during and shortly after the conference, especially from some authors of references [1]-[6].

2. The 3-D Expansion/Rotations/Translation Model

In 3-D Euclidian space we can map the Skiadas model onto the sphere with 2 or 3 rotations. A vector coordinate $\mathbf{p}_t$ will describe the signal location at a time t and after on jump iteration at $\mathbf{p}_{t+\tau}$. The signal starts at $\mathbf{p}_0$. First we apply a expansion/reflection matrix $\mathbf{E}$, then apply $N = 3$ different rotation in planes $\mathbf{P}_i$, $i = 0,1,..,N-1$, each containing $l = 0,1,..,m_i - 1$ singularities $\mathbf{s}_{i,l}$ defining the rotation centre. At this location the axes $\mathbf{X}_{i,l}$ intersect $\mathbf{P}_i$ orthogonally. The rotation angle $\vartheta_{i,l}$ with

$$\vartheta_{i,l} = 2\pi c_i \left(\frac{|\mathbf{v}|\tau}{|\mathbf{p}_t - \mathbf{s}_{i,l}|} \right)^2 , \qquad (1)$$

shows a characteristic Skiadas power-law dependence [1] on the distance between signal and singularity coordinates $|\mathbf{p}_t - \mathbf{s}_{i,l}|$ with power exponent value usually in the range 1-3, where the magnitude is given by the coupling constants c_i. We have chosen a form producing patterns linearly scaling with the jump distance $|\mathbf{v}|\tau$ while preserving shape. For one singularity per dimension $m_i = 1$ the three rotations with angles ϑ_i are computed by the rotation matrices $\mathbf{R}_i$ applied in a given permutation sequence. We take a proper coordinate system diagonalizing $\mathbf{E}$ with pure diagonal expansion/reflection components $e_{ij} = 0$ for $i \neq j$ and $|e_{xx}| = |e_{yy}| = |e_{zz}| > 0$. For this case we will use the short notation $\mathbf{E} = \mathrm{ED}(e_{xx}, e_{yy}, e_{zz})$, a negative sign shows a so-called reflection in the corresponding coordinate. These components and boundary conditions provide for the basic 3-D recurrent algorithm and difference equation as a simple extension to [1, 2, 3] generating one jump with distance $|\mathbf{v}\tau|$ after the interval τ. If we assume orthogonal rotation axes with rotation matrices $\mathbf{R}_i$ elements of the SO(3) rotation group, we have a common rotation centre located at $\mathbf{r}$ as the intersection of the rotation axes with one singularity fro every dimension ($m_i = 1$) and $\mathbf{X}_{0,0} \perp \mathbf{X}_{1,0} \perp \mathbf{X}_{2,0}$, where the chaotic map given by

$$\mathbf{p}_{t+\tau} = \mathbf{v}\tau + \mathbf{R}_2\left[\mathbf{R}_1\left[\mathbf{R}_0\left[\mathbf{E}\left[\mathbf{p}_t - \mathbf{r}\right]\right]\right]\right] + \mathbf{r} . \qquad (2)$$

To get pure rotations, the straight translation shift $|\mathbf{v}\tau|$ in eqs. (2) and (1) could be approximated by constant orbital rotations in one dimension with label j and $|\mathbf{r}_j|\vartheta_j = 2\pi|\mathbf{v}\tau|$ leading to the Skiadas rotations coupling

$$\vartheta_{i,l} = 2\pi c_i \left(\frac{|\mathbf{r}_j| \vartheta_j}{2\pi |\mathbf{p}_t - \mathbf{s}_{i,l}|} \right)^{d_{i,l}} \text{, in 3-D usually } d_j = 2 \text{,} \qquad (3)$$

where the coupling factor c_i can be varied in a wide range. Spin is given by an orbital rotation with label $i = j$ that has one singularity at the centre $\mathbf{s}_{j,0} = (0,0,0)$, where

$$\left(\frac{\vartheta_j}{2\pi} \right)^{1-d_j} = c_j \frac{|\mathbf{r}_j|^{d_j}}{|\mathbf{p}_t|^{d_j}} \text{, for } d_j = 1 \text{ simply } |\mathbf{p}_t| = c_j |\mathbf{r}_j| \text{.} \qquad (4)$$

The iterative 3-D difference equation (2) for one start point or delta distribution $\mathbf{p}_0 = \mathbf{p}_{t=0}$ with 3 singularities and 3 orthogonal rotations is now

$$\mathbf{p}_{t+\tau} = \mathbf{R}_{\vartheta_2} \left[\mathbf{R}_{\vartheta_1} \left[\mathbf{R}_{\vartheta_0} \left[\mathbf{E}[\mathbf{p}_t - \mathbf{r}] \right] \right] \right] + \mathbf{r} \text{.} \qquad (5)$$

To obtain interesting patterns on the spherical surface we set $\mathbf{R}_{3,1} = \mathbf{R}_\theta$ as the constant longitude or orbital advance, and $\mathbf{R}_{1,2} = \mathbf{R}_\vartheta$ for the altitude. Both rotations rotate around singularities given by

- $m_{3,1} = 1$, one longitude rotation $\mathbf{R}_{3,1} = \mathbf{R}_\theta$ rotating around $\mathbf{s}_{3,1,1} = (0,0,0)$ with power law exponent $d_{3,1,1} = 0$ and rotation/coupling strength $c_{3,1,1} = 2\pi j M^{-1}$,
- $m_{1,2} = 1$, one latitude rotation $\mathbf{R}_{1,2} = \mathbf{R}_\vartheta$ rotating around $\mathbf{s}_{1,2,1} = (0,0,1)$ with power law exponent $d_{1,2,1} = 2$ and rotation/coupling strength $c_{1,2,1} = 2\pi k^{-2} M^{-2}$.

As an example, a two-angle rotation and signal position $\mathbf{p}_t$ subject to rotation in 3-D spherical coordinates φ, ϕ and singularity rotations $\vartheta_0 = \vartheta$, $\vartheta_1 = \theta$, is given by

$$\mathbf{p}_t(\varphi,\phi) = \begin{pmatrix} \sin\varphi\cos\phi \\ \cos\phi \\ \sin\varphi\sin\phi \end{pmatrix}, \mathbf{R}(\theta,\vartheta) = \begin{pmatrix} \cos\vartheta\cos\theta & -\sin\vartheta\cos\theta & \sin\theta \\ \sin\vartheta & \cos\vartheta & 0 \\ -\cos\vartheta\sin\theta & \sin\vartheta\sin\theta & \cos\theta \end{pmatrix}.$$

With one singularity located at $\mathbf{s}_0 = (0,0,1)$ with $d = 2$ and one at the centre $\mathbf{s}_1 = (0,0,0)$ with $d = 0$ we get the two scalar rotations in spherical coordinates

$$\vartheta = c \frac{\theta^2}{4\pi(1 - \sin\varphi\sin\theta)}, \ \theta = \frac{2\pi j}{M}, \ c = \frac{1}{j^2 k^2} \text{.} \qquad (6)$$

3. Hyper-Sphere Expansion-Reflection-Rotations Map

The extension to the n-*D* signal map $\mathbf{p}_t \to \mathbf{p}_{t+\tau}$ with rotations embedded in *n*-D Euclidean space for $n \geq 3$ is straight forward. The matrix operations are based on the orthogonal group O(*n*), or the Lie spin group Spin(*n*) as the double cover of the special orthogonal group SO(*n*) defining the $n \times n$ rotation matrices $\mathbf{R}_{a,b}$. The number of rotational degrees of freedom and number of orthogonal rotation planes $\mathbf{P}_{a,b}$ is

$$N(n) = \binom{n}{2} = \frac{n(n-1)}{2}, \; N(n \geq 2) = 1,3,6,10,15,21,28,36,45,\ldots . \quad (7)$$

One plane can have orthogonal axes $\mathbf{X}_l$ intersecting the plane at the singularity locations $\mathbf{s}_{a,b,l}$, l labels all orthogonal axes with $l \neq a, l \neq b$. We rotate on this plane if the rotation plane has at least one orthogonal intersection $m_{a,b} > 0$ at the singularity locations. The maximum is $m_{a,b} = (n-2)$, if $m_{a,b} = 0$ there are no singularities and no rotations in $\mathbf{P}_{a,b}$. So the total number of possible orthogonal axis intersections for all planes and the maximum number of singularities is $L = (n-2)N = n(n-1)(n-2)/2$. There is a set of N orthogonal matrices $\mathbf{R}_{a,b}{}^T = \mathbf{R}_{b,a} = \mathbf{R}_{a,b}{}^{-1}$ with $\det \mathbf{R}_{a,b} = 1$ defining the special orthogonal group SO(*n*) given according to [4] by

$$\mathbf{R}_{a,b}(\vartheta_{a,b,l}) = \begin{bmatrix} & r_{a,a} = \cos(\vartheta_{a,b,l}) \\ & r_{b,b} = \cos(\vartheta_{a,b,l}) \\ & r_{a,b} = -\sin(\vartheta_{a,b,l}) \\ r_{i,j} & r_{b,a} = \sin(\vartheta_{a,b,l}) \\ & r_{j,j} = 1,\ j \neq a,\ j \neq b \\ & r_{i,j} = 0,\ \text{elsewhere} \end{bmatrix}, \quad (8)$$

with trace $n - 2\left[1 - \cos(\vartheta_{a,b,l})\right]$ and angles $\vartheta_{a,b,l}$, $l \neq a, l \neq b$. The signal is located on the hyper-spheres. The sequence of orthogonal matrices rotating a vector $\mathbf{x}_t$ in Euclidean space must be ordered

$$\mathbf{R}_{A,B}\left[\mathbf{x}_t\right] = \mathbf{R}_{\ldots}\left[\ldots\left[\mathbf{R}_{a,b}\left[\ldots\left[\mathbf{R}_{\ldots}\left[\mathbf{x}_t\right]\right]\right]\right]\right], \quad (9)$$

covering all possible rotations or a subset as a permutation. Building the chaotic map with an *n*-D expansion/reflection $\mathbf{E}$ then applying the rotation sequence $\mathbf{R}_{A,B}$ we have

$$\mathbf{p}_{t+\tau} = \mathbf{R}_{A,B}\left[\mathbf{E}\left[\mathbf{p}_t - \mathbf{r}\right]\right] + \mathbf{r} . \quad (10)$$

We are left to specify the generalized rotation angles $\vartheta_{a,b,l}$, the matrix coefficients for a rotation $\mathbf{R}_{a,b}(\vartheta_{a,b,l})$, the number of singularities $m_{a,b}$, and the temporal order of rotations. The angles $\vartheta_{a,b,l}$ corresponding to $\mathbf{s}_{a,b,l}$ will have with strength $c_{a,b,l} \in \mathbb{R}$, metric distance $|\mathbf{p}_t - \mathbf{s}_{a,b,l}|$, and power exponent $d_{a,b,l} \geq 0$ a form given by

$$\vartheta_{a,b,l} = 2\pi c_{a,b,l} \left(\frac{|\mathbf{v}\tau|}{|\mathbf{p}_t - \mathbf{s}_{a,b,l}|} \right)^{d_{a,b,l}} . \tag{11}$$

To systematically generate meaningful setup values in higher dimensions providing for interesting patterns for $n > 2$ with physical relevance, we recommend for simplicity to take a Gauss-type classical coupling field gradient power exponent

$$d_{a,b,l} = n - 1 , \tag{12}$$

where the gradient power exponent is the Gauss' law field strength exponent plus 1 (for 3-D we have $d_{a,b,l} = 2$, see below). But of course, as Skiadas has shown there are several exponents that can lead to nice patterns. The power law coupling strength is scaling with the field gradient power exponent and coupling number k

$$c_{a,b,l} = k^{-d_{a,b,l}} . \tag{13}$$

The temporal order of rotations $\mathbf{R}_{a,b}$ part of the global sequence $\mathbf{R}_{A,B}$ as a permutation sequence must be given in order to setup the map and reproduce results. For the purposes of this paper we let run a in an outer loop from 0 to $n-1$, then b in the next inner loop from $a+1$ to $n-1$ covering the $N = n(n-1)/2$ orthogonal rotation planes $\mathbf{P}_{a,b}$ with orthogonal matrices $\mathbf{R}_{a,b}$, and finally l in the most inner loop from 0 to $n-1$ with $l \neq a, l \neq b$, since every plane has $n-2$ orthogonal axes intersecting at the singularities providing for the total number of singularities rotations $L = n(n-1)(n-2)/2$.

4. Results

4.a Four basic 2-D rotation-translation types with radial power -3

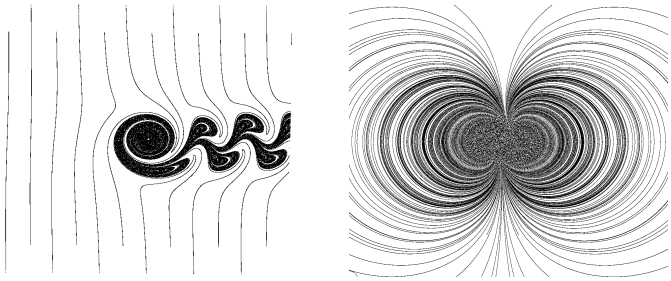

Fig. 1. Left (Skiadas [1]): EC = (1,-1). Right EC = (-1,1) , randomized starts.

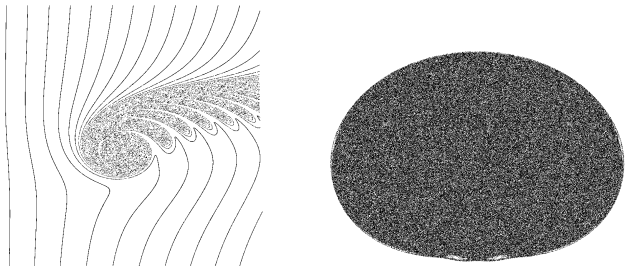

Fig. 2. Left (Skiadas [3]): EC = (1, 1). Right EC = (-1,-1), randomized starts.

4.b Periodic boundary (at $d_0 = 16\tau$) in 2-D at power -3

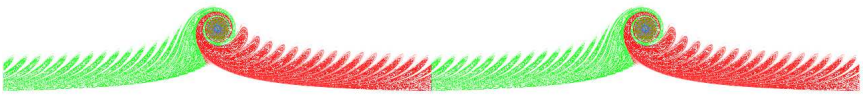

Fig. 3. EC = (1, 1), if distance $x > d_0$ then $x \rightarrow x$ - 2-D_0, $y \rightarrow y$, slightly random.

Fig. 4. The periodic Skiadas pattern, same parameter like fig.3 but EC = (1, -1).

Fig. 5. Parity change for EC = (1, -1): if distance $x > d_0$, then $x \rightarrow -x$ $y \rightarrow y$.

4.c Helical twist and 2-D rotation in 3-D

Fig. 6. 3-D cyclic within $d_0 = 16\tau$, power -3, with extra double-helix rotation $\psi = 5\pi x / d_0$ proportional to distance x, EC = (1, -1), randomized starts.

4.d. Multi-singularity and multi-expansion in 2-D, overlapping patterns

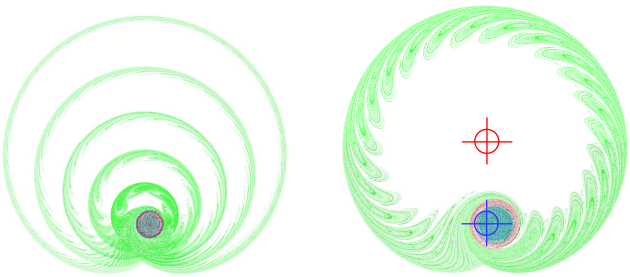

Fig. 7. Two equal singularities: positive at (0,0) and negative located at (0, 2j), j = 1,2,3,4,5, power -3, EC = (1, 1). Right: enlarged j = 1 with one positive (blue) and one negative (red) singularity.

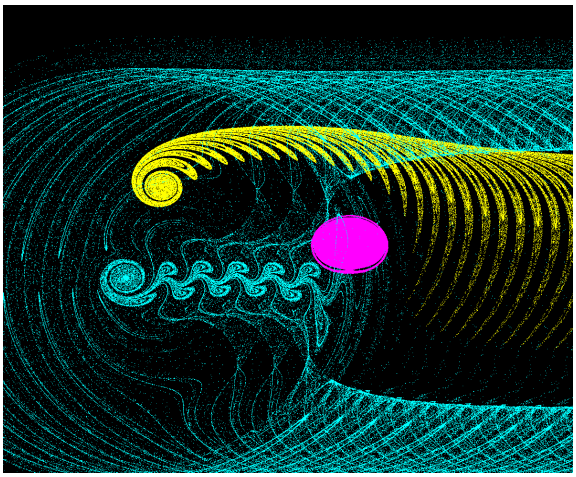

Fig. 8. Three singularities at different locations, power -3, multi expansion, 3 different EC: (1, 1) and (1, -1) and (-1, -1), randomized starts.

4.e Rotation-Rotation in 3-D, rotation centre at (0,0,0), singularity at (0,0,1)

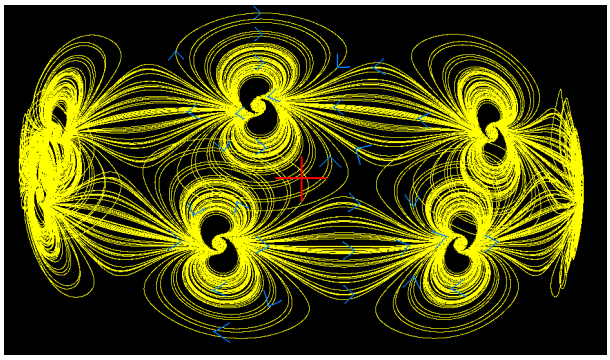

Fig. 9. Dipole ring, power -2, $M = 7$, EC = (1,-1, 1), $k = 8$, slightly random. Flow directions are indicated by blue arrows.

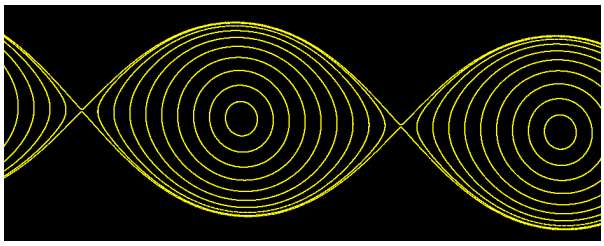

Fig. 10. Rings deformed to a wave, power -2, $M = 113$, EC = (1, 1, 1), $k = 20$, $\overset{\mathrm{r}}{s}_{0,i} = (x_i, \sqrt{1-x_i^2}, 1)$, $x_i = i / M / 10, i = 1,2,...,10$, $j = 1$.

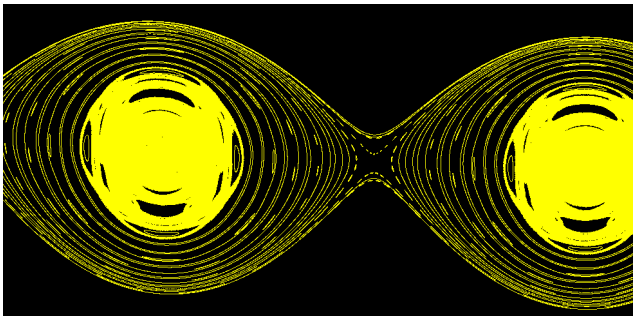

Fig. 11. Similar to fig. 10 but chaotic core with $k = 2$, power -2, $M = 13$, EC = (1, 1, 1), $\overset{\mathrm{r}}{s}_{0,i} = (x_i, \sqrt{1-x_i^2}, 1)$, $x_i = i / M / 10, i = 1,2,...,10$, $j = 1$.

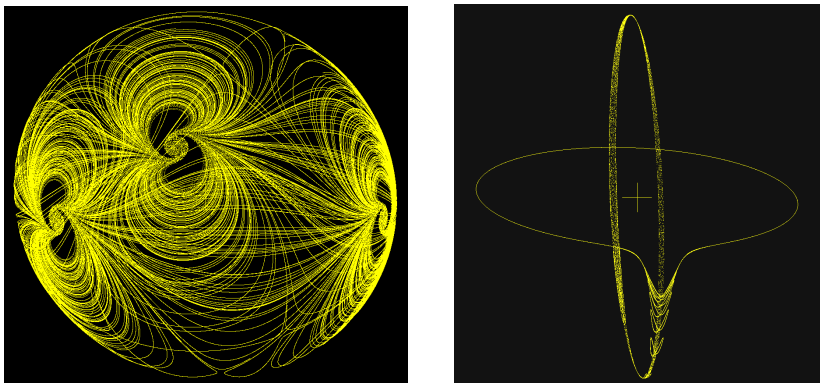

Fig. 12. Left: dipole patterns from random starts, power -2, $M = 3$, EC = (1,-1, 1), $k = 4$, $j = 1$. Right: $\vartheta_t(\theta_t)$ with EC = (1, 1, 1), chaotic core, power -2, $M = 13$.

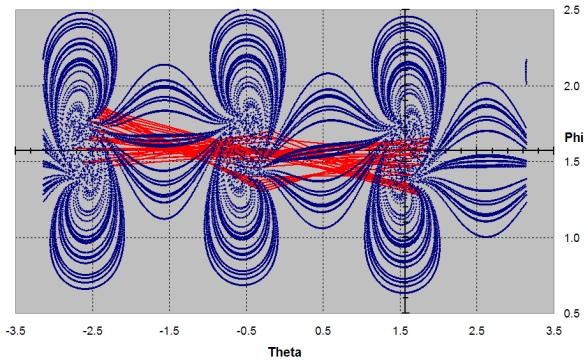

Fig. 13. Dipole pattern mapped to the rectangular phase space, power -2, $M = 3$, EC = (1,-1, 1), $k = 3$, $j = 1$ after 32000 steps. Red are some jump path lines.

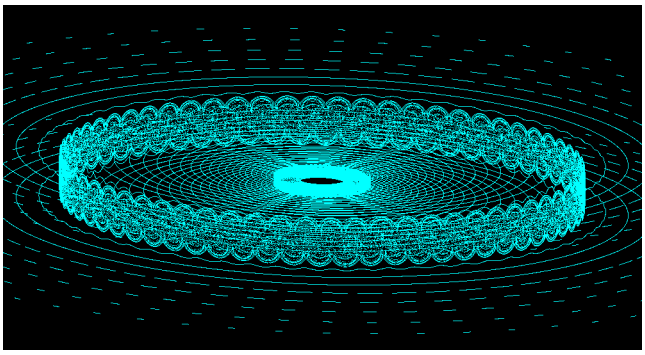

Fig. 14. $M = 128$, $k = 1$, EC = (1, -1, 1), radial variation, $d = (2,0)$

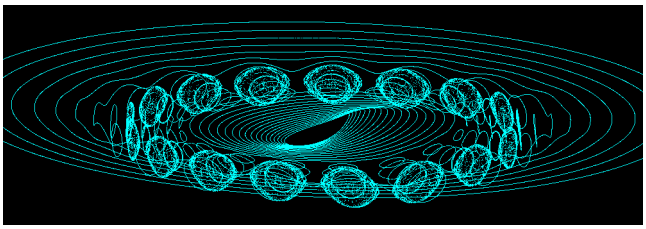

Fig. 15. $M = 20$, $k = 2.3$, EC = (1, 1, 1), radial variation, $d = (2,0)$

4.f Higher-Dimensional Rotated-Rotations

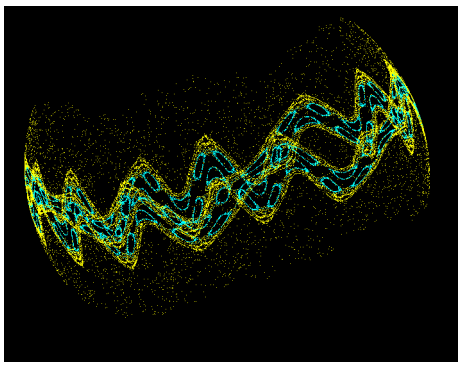

Fig. 16. $n = 3$, $k = 2$, EC = (1, -1, 1), angular variation, $d = (2,2,2)$

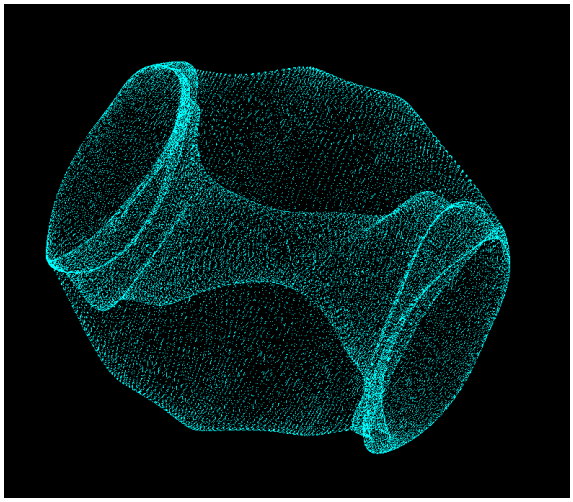

Fig. 17. $n = 4$, 3-D Projection, $k = 1$, EC = (1, -1, 1,-1)

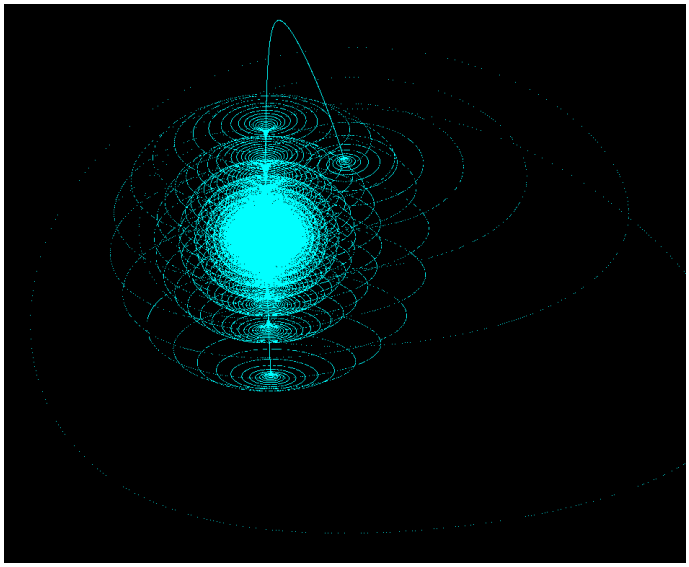

Fig. 18. $n = 4$, 3-D Projection, $k = 12$, EC = (1, -1, 1,-1), $d = (3,0,3,0)$

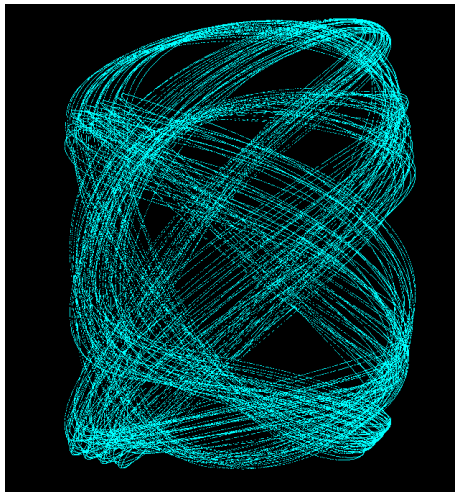

Fig. 19. n = 5, 3-D Projection, k = 1, EC = (1, -1, 1,-1,1), d = (4,0,4,0,4)

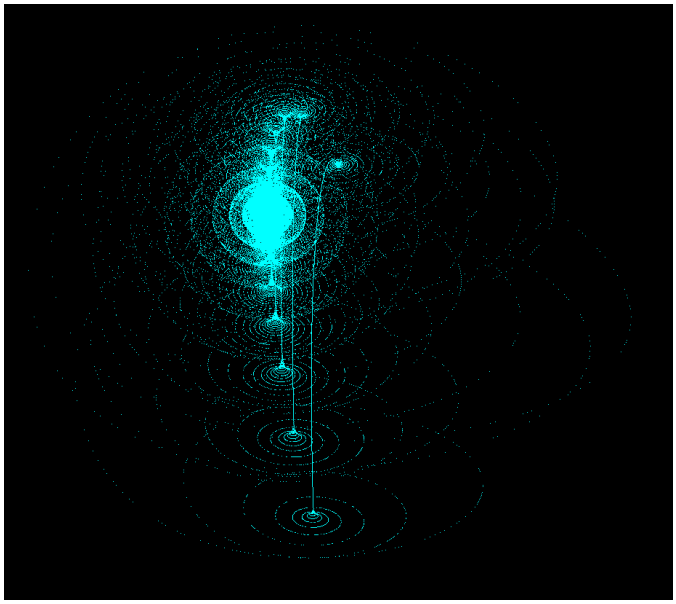

Fig. 20. n = 6, 3-D Projection, k = 6, EC = (1, -1, 1,-1, 1,-1), d = (5,0,5,0,5,0,5)

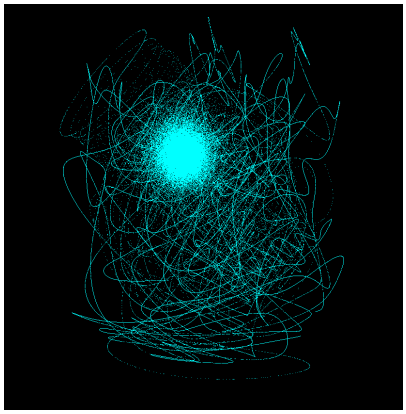

Fig. 21. n = 10, 3-D Projection, k = 12, EC = (1,1,1,1,1,1,1,1,1,1), d = (9,9,9,9,9,9,9,9,9,9)

5. Measure of Chaos/Exponents

Since the map can be extended to an arbitrary number of dimensions n and singularities, we can have a higher-dimensional chaos located in or on hyper-spheres with rotation axes defined by hyper-planes, so it could be called hyper-chaos [5,6] or hyper-sphere chaos. As a measure of chaos we have computed the mean space trajectory separation exponent in n-D between two nearby vectors $\mathbf{p}_{1,t}, \mathbf{p}_{2,t}$ for one complete n-D iteration step during the time τ averaging $0 < i < I$ successive steps with $t = i\tau$

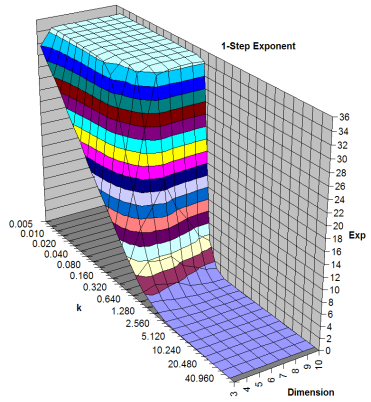

Fig. 22. The 1-step exponent E_τ for n = 3,4,…,10 dimensions and I = 500

$$E_\tau = \frac{1}{I}\sum_{i=0}^{I-1} \log\left[\left|\mathbf{p}_{1,t+(i+1)\tau} - \mathbf{p}_{2,t+(i+1)\tau}\right| / \left|\mathbf{p}_{1,t+i\tau} - \mathbf{p}_{2,t+i\tau}\right|\right], \qquad (14)$$

which is a cheap estimate of the Lyapunov exponent. This exponent is highly stable and increases with the number of dimensions n and with the amplitude/strength factor k of rotation, see fig 24. In our simulation the 1-step exponent E_τ was in our case limited to about 35 due to the double precision limit of the floating point computing unit. It starts to increase strongly near to the control parameter value k = 0.5, see eq.(12). There the pattern becomes "randomized" and chaotic especially at higher hyper sphere rotation dimensions. At higher exponents we find that the map is a good pseudo-random number generator in any dimension $n > 2$. Fig. 22 was obtained without expansion or compression EC = (1,1,1, ...) like all of shown patterns in all figures. With compression-reflection coefficients smaller 1 like EC = (0.99,0.99,0.99, ...) we get negative exponents for k ? 0.5 and in-spiralling towards the centre.

6. Cryptography with Hyper-Chaos on the Hyper-Sphere

The rotations $\mathbf{R}_{a,b}$ part of the global sequence $\mathbf{R}_{A,B}$ do not commute, so the time ordering is crucial. The non-commutative permutations of the non-abelian group elements are relevant for encryption purposes. If the permutation is a sequence with a selection of K elements out of $L = N(n\text{-}2) = n(n\text{-}1)(n\text{-}2)/2$ rotations that contains each element once, the number of combinations is given by $C = L!/(L-K)!$. Knowing the rotation angles $\vartheta_{a,b,l}$ and the global sequence $\mathbf{R}_{A,B}$, the rotation can only be reversed by applying the rotations and expansion/reflections part of $\mathbf{R}_{A,B}$ in reversed order. This is an encryption given by a rotation permutation from a series of linked non-commuting mathematical operations, where decryption is done by simply reversing the process applied to signal packages containing some bits of information. The key complexity defining the variations in the rotation sequence would be given by the permutation of combinations. In addition there is the freedom to choose the rotation angles, the initial condition in the signal $\mathbf{p}_0 = \mathbf{p}_t(t=0)$, and the singularity locations $\mathbf{s}_{a,b,l}$ with given precision. Secret key sharing could be done by hiding the initial conditions $\mathbf{p}_0 = \mathbf{p}_t(t=0)$, the singularity locations $\mathbf{s}_{a,b,l}$, and eventually some rotation axes $\mathbf{X}_b$ with Blakley's scheme from the intersection of distributed planes $\mathbf{P}$ [7], where any of the N nonparallel 2-dimensional hyperplanes intersect at a specific point or axis, and each participant is given enough information to define one of the hyper-planes $\mathbf{P}$. Of course, key-shifting during the sequence could also be introduced, which could be done by mobile singularities providing for extreme confusion and diffusion properties. Thus reversibility is practically limited to a small number of encryption/decryption operations due to a limited calculation precision and the high exponential divergence and pseudo-randomness, see fig. 24.

7. Mobile Singularities Exchanging Momentum Quanta

Up to now the simulated singularities had a static location. But a physical situation usually requires mobile singularities.

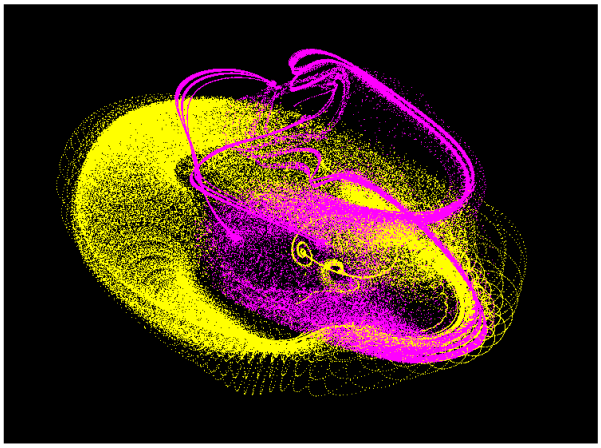

Fig. 23: Two massive mobile singularities generating and absorbing yellow and pink signals carrying momentum and providing for a vector-field.

An important extension would be given by mobile singularities $\mathbf{s}_{a,c,l} \to \mathbf{s}_{a,c,l}(t) = \mathbf{s}_{t,a,c,l}$ or mobile rotation axes carrying momentum like spinning particles with spin – orbit coupling. In the real world the emission or absorption of a rotation-translation or rotation-rotation signal would transfer a linear or angular momentum quantum to and from the singularity if it has a nonzero angular momentum. In addition to the various possibilities to introduce local rotations and accelerations from distance-dependent interactions between singularities is to provide for an extra rotational interaction dynamics between two mobile singularities $\mathbf{s}_{t,a,c,l}$ and $\mathbf{s}_{t,b,c,l}$, there could be a common rotation $\bar{\mathbf{R}}_{t,c}(\bar{\vartheta}_{t,c})$ with common axis $\bar{\mathbf{X}}_c$ (length is the rotation angle) performing the interaction of singularities. Here are two possibilities:

(1) parallel to one of the rotation axes $\bar{\mathbf{X}}_c \, \mathrm{P} \mathbf{X}_a$ or $\bar{\mathbf{X}}_c \, \mathrm{P} \mathbf{X}_b$ or

(2) orthogonal to the interacting singularities rotation axis $\bar{\mathbf{X}}_c \perp \mathbf{X}_a \perp \mathbf{X}_b$, $\bar{\mathbf{X}}_c = \mathbf{X}_a \times \mathbf{X}_b$ having SO(3) symmetry with new interaction singularity located on the intersection of the three axes.

To get something like a mass or providing for inertia and angular momentum a density of visited points after many jumps at time t or spatial sampling function dependent on the initial conditions $\rho_{t=0}$ could be defined by

$$\rho_{t=I\tau}(\mathbf{x}) = \frac{1}{I} \sum_{i=0}^{I-1} \delta(\mathbf{x} - \mathbf{p}_{i\tau}) \,. \tag{15}$$

With the expanded density by $\wp_t = \mathbf{E}[\rho_t]$, $\mathbf{E}^{-1}[\wp_t] = \rho_t$ we get the difference operator equation $\mathbf{R}_{A,B}[\wp_t] = \mathbf{E}^{-1}[\wp_{t+\tau}]$. Equilibrium is approached for $\wp_t \approx \wp_{t\to\infty}$.

8. Discussion

How do patterns emerge from eq.10? At the present stage we just start to explore the very rich system of pattern formation from map parameter and initial value customization. Without systematic approach this task is hard to do. A basic pattern property at lower dimensions can be assigned to the sign of the reflection exponent, a negative sign leads to an up/down oscillatory behaviour in the jumps shaping the pattern in the altitude, see fig. 13. In the other direction the orbital loops with $\theta_{j,M} = 2\pi j / M$ around axes at coupling exponent $d = 0$ can provide at any radius M/j orbital jump position that are only slightly shifted after every loop, see figs 9-16. At higher dimensions even at high k-values (see figs 19, 21, and 23) the patterns look often more random than the nice structures and symmetries that can be easily obtained at lower dimensions, see figs 1-16. In 4, 5, and 6 dimensions we found interesting structures just by trial, see 17-20. The Skiadas singularity rotation varies with radial distance to the singularity and coupling factor or rotation strength $1/k$ as an important tuning parameter to obtain the pattern structures, see figs. 12-15 and 22. The smaller k, the higher the extra rotation providing for a more nonlinear behaviour and chaotic or even pseudo-random stochastic structure in the pattern, especially near the equatorial location of the singularity, see fig. 12 right. Subject to periodic boundaries and closed loop/orbits our chaotic jump functions show especially at higher k values in the non-chaotic regime (k ? 1) a small chaotic core at the centre. At strong rotations the divergence and exponents can grow unbounded, see fig 22, leading to pseudo-random patterns. Due to the singularity on the orbit there is no perfect rotational M-gonal symmetry, the angular parts are slightly different, most different is the orbital part where the singularity is located, see fig. 13, where every dipole has a slightly different shape, especially the chaotic core is different.. Smaller shifts produce traces and linear flows with basic symmetries known from other fields. At special values of j, k, and initial conditions we get almost M-independent regular structures like rings and waves or dipole type flows, see figs 9-15.

It can be found that the path and singularity determines the shift, which is typical for geometric shifts or phases. In physics this extra shift is known as a geometric phase emerging on curved surfaces. In [8] we have presented a strange attractor involving geometric phases from three rotations on the sphere, where a linear rotation – translation coupling (rolling or helical paths) provides for simplifications with very interesting holonomic attractor singularities from iterations. We think that the geometric phase interpretation and correspondent phase shift concepts are also valid here, but near to the singularities or “monopole charges” the geometric phase extra rotation is small compared to the

singularity rotation. Since sum of the rotations given by the rotation vector field provides for a vector potential it is not surprising that the patterns at small coupling strengths and far away from singularities look like iso-potential lines for inverse power interaction laws, in fig.9 for a magnetic dipole chain and in fig.10 for a shear flow or pendulum chain. For smaller couplings $1/k$ we get the some rather linear physical properties:

- monopoles and dipoles (dipole see fig. 1b and chain in fig. 9),
- twistorial spin (vortex structures, see fig. 1 and 20, helical twist fig. 6),
- parity properties and even/odd symmetries (see figs. 3-5),
- j and M could be interpreted as spin and orbital number, respectively,
- inbuilt constant propagation velocity in the translation or rotation in eq. (2),
- Gauss flux exponent d in $n = d + 1$ dimensions,
- wave/particle duality with discrete jumps providing for density patterns,
- scalar and vector fields with standard gauge symmetries,
- angular momentum transfer, interaction and kinetic energy.
- hierarchy of patterns, see figs. 18 and 20,

Opening the loop and translating it into a helical path keeps the basic pattern units if proper periodic boundaries with reflection are introduced. Remarkably, periodic rotation-rotation dipole-dipole interaction patterns emerge on the spherical or helical loop, where the characteristic flux lines are emitted from a chaotic core, see figs. 9, 12-16. Dipole chain patterns play a very important role for living organisms since the molecular dipole interaction leads to protein folding. “Every process of protein formation, from the binding of individual amino acids to secondary structures to tertiary structures and even the formation of quaternary structures is dependent on dipole-dipole interactions [9].”

4-D patterns projected to 3-D show often torus shapes, see fig. 17, typically relevant to Hamiltonian system of spin-spin and spin-orbit coupling. Spin(n) is simply connected and so coincides with the universal cover of SO(n) with isomorphisms and decompositions among the classical Lie groups like Spin(2) = U(1) = SO(2), Spin(3) = SU(2), Spin(4) = SU(2) x SU(2), SU(4) = Spin(6). So Spin(2) and Spin(3) structures can be embedded together in Spin(4). The same can be done in arbitrary high dimensions providing in our case for interplay of low-dimensional ordered states part of a higher-dimensional chaos. This could point to a kind of “itinerancy” [10]. Figs. 18 and 20 show connected (by thin wormholes) lower-dimensional chaotic structures embedded in 4-D and 6-D higher-dimensional systems with very low LE in the projection to three dimensions. This could have relevance to the standard model high energy particle physics with separable but interconnected subgroups in the 10-D gauge field embeddings $\mathrm{SU}(3)\times\mathrm{SU}(2)\times\mathrm{U}(1)$; $SU(5)$ [4].

Introducing mass and momentum, mobile singularities emitting and absorbing the jumping chaotic signal quanta carrying momentum and travelling at constant

speed provide for a very rich chaotic behaviour and dynamics, see the special example in fig. 23.

9. Conclusions

We conclude that using an iterative reflection-rotation-rotation/translation difference equation modelling approach according to Skiadas we can obtain many new interesting patterns with attributes similar to those known from physics. The multiple rotation formula generating hyper-sphere chaos can be extended to an arbitrary number of dimensions, rotations, and singularities. Mobile singularities could even produce more chaos. If the singularity is located at very large distances a small rotation can approximate a translation. At special numbers with smaller coupling $1/k$ and special initial conditions regular structures like rings, spirals, and waves or the many dipole-dipole interaction flows emerge, which could be promising for molecular science and new basic level concepts. Important for a pattern generation on the orbit is a tiny but nonlinear shift in both angular variables due to a cyclic and path dependent singularity extra rotation that is small compared to the orbital angular steps and more linear at smaller coupling (higher k) values. The hyper-sphere chaos from rotation permutations could act s a pseudo-random generator of chaotic patterns relevant for crypto applications with key given by initial conditions and the special rotation permutation sequence in higher dimensions.

References

1. C. H. Skiadas and C. Skiadas, Chaos in Simple Rotation-Translation Models, http://arxiv.org/abs/nlin/0701012, nlin.CD, 2007.
2. C. H. Skiadas and C. Skiadas. *Chaotic Modeling and Simulation: Analysis of Chaotic Models, Attractors and Forms*, Taylor and Francis/CRC, London, 2008.
3. C. H. Skiadas, Von Karman Streets Chaotic Simulation, *Topics on Chaotic Systems*, C. H. Skiadas, I. Dimotikalis and C. Skiadas, (Eds), World Scientific, 309-313, 2009.
4. M. Kaku, *Hyperspace: A Scientific Odyssey Through Parallel Universes, Time Warps, and the Tenth Dimension*, Oxford University Press, 1994.
5. O.E. Rössler, „An equation for hyperchaos“, Phys. Lett. A 71, 155, 1979.
6. G. Qi, D. L. Owuor, A. E. Botha, Robustness and Bit Error Rate Performance of Qi Hyper Chaos Based Encryption, *CHAOS2012 Proceedings*, C. H. Skiadas, I. Dimotikalis, and C. Skiadas, (Eds), 2012.
7. G. R. Blakley, "Safeguarding cryptographic keys". Proceedings of the National Computer Conference 48, 313–317, 1979.
8. B. Binder, Magic Angle Chaotic Precession, *Topics on Chaotic Systems*, C. H. Skiadas, I. Dimotikalis, and C. Skiadas, (Eds), World Scientific, 31-42, 2009.
9. Chem Wiki for Dipole-Dipole Interaction, http://chemwiki.ucdavis.edu, search “Dipole-Dipole_Interactions”, accessed 5.5.2012.
10. K. Kaneko, I. Tsuda, “Chaotic Itinerancy”, Chaos 13(3), 926-936, 2003.


Proceedings, 5th Chaotic Modeling and Simulation International Conference, 12 – 15 June 2012, Athens Greece

Dichotomy and boundary value problems on the whole line

Alexander A. Boichuk[1] and Oleksander A. Pokutnyi[2]

[1] Institute of mathematics of NAS of Ukraine, , 01601 Kiev, Ukraine
(E-mail: boichuk@imath.kiev.ua)
[2] Institute of mathematics of NAS of Ukraine, , 01601 Kiev, Ukraine
(E-mail: lenasas@gmail.com)

Abstract. Necessary and sufficient conditions for normal solvability are obtained for linear differential equations in Banach space. Constructed examples demonstrate that even in the linear case (but certainly not correct) you can select a family of bounded solutions, which tend to an equilibrium positions, so-called homoclinic and heteroclinic trajectories.

Keywords: exponential dichotomy, normally-resolvable operator, pseudoinverse operator.

A lot of papers are devoted to development of constructive methods for the analysis of different classes of boundary value problems. They traditionally occupy one of the central places in the qualitative theory of differential equations. This is due to practical significance of the theory of boundary-value problems for various applications - theory of nonlinear oscillations, theory of stability of motion, control theory and numerous problems in radioengineering, mechanics, biology etc.

Correct and incorrect boundary value problems are studied. Ususally correctness is understood as uniqueness of the solution for arbitrary right-hand side of the equation. Correct boundary value problems for ordinary differential equations, impulsive systems, Noether operator equations became popular relatively recently, they were studied in detail [5]. Analysis of a large class of incorrect boundary value problems was associated with the properties of the generalized inverse operator (which exists for any linear operator in a finite dimensional space).

Efforts aimed to solving problem of the existence of bounded solutions of linear differential equations are mainly devoted to the correct case. Additional boundary conditions can be full filled only in a trivial situations for such problems. After Palmer's work [2] it became clear that in the general case, even a finite set of differential equations can not have one bounded solution, and it makes sense to study the boundary value problem in the incorrect case. Using the pseudoinverse operators approach one can obtain the conditions under which a family of bounded solutions satisfying the supplementary boundary conditions can be identified.

1 Statement of the Problem

In a Banach space $\mathbf{X}$ we consider a boundary value problem

$$\frac{dx}{dt} = A(t)x(t) + f(t) \ , \tag{1}$$

$$lx(\cdot) = \alpha \ , \tag{2}$$

where the vector - function $f(t)$ acts from R into the Banach space $\mathbf{X}$,

$$f(t) \in BC(R, \mathbf{X}) := \{f(\cdot) : R \to \mathbf{X}, f(\cdot) \in C(R, \mathbf{X}), |||f||| = \sup_{t \in R} \|f(t)\| < \infty\},$$

$BC(R, \mathbf{X})$ is the Banach space of functions continuous and bounded on R; the operator-valued function $A(t)$ is strongly continuous with the norm $|||A||| = \sup_{t \in R} ||A(t)|| < +\infty$; $BC^1(R, \mathbf{X}) := \{x(\cdot) : R \to \mathbf{X}, \ x(\cdot) \in C^1(R, \mathbf{X}), |||x||| = \sup_{t \in R}\{\|x(t)\|, \|x^1(t)\|\} < \infty\}$, - the space of functions continuously differentiable on R and bounded together with their derivatives; l - linear and bounded operator acts from the space of $BC^1(R, \mathbf{X})$ into the Banach space $\mathbf{Y}$. We determine the conditions of the existence of solutions $x(\cdot) \in BC^1(R, \mathbf{B})$ of boundary value problem (1), (2) under the assumption that the corresponding homogeneous equation

$$\frac{dx}{dt} = A(t)x(t) \tag{3}$$

admits an exponential dichotomy [1–3] on the semi-axes R_+ and R_- with projectors P and Q, respectively, i.e., there exist projectors $P(P^2 = P)$ and $Q(Q^2 = Q)$ and constants $k_{1,2} \geq 1$ and $\alpha_{1,2} > 0$ such that the estimates

$$\begin{cases} \left\|U(t)PU^{-1}(s)\right\| \leq k_1 e^{-\alpha_1(t-s)}, \quad t \geq s, \\ \left\|U(t)(E-P)U^{-1}(s)\right\| \leq k_1 e^{\alpha_1(t-s)}, \quad s \geq t, \ \text{ for all } \quad t, s \in R_+, \end{cases}$$

and

$$\begin{cases} \left\|U(t)QU^{-1}(s)\right\| \leq k_2 e^{-\alpha_2(t-s)}, \quad t \geq s, \\ \left\|U(t)(E-Q)U^{-1}(s)\right\| \leq k_2 e^{\alpha_2(t-s)}, \quad s \geq t, \quad \text{for all } \ t, s \in R_- \end{cases}$$

hold, where $U(t) = U(t, 0)$ is the evolution operator of Eq. (3) such that

$$\frac{dU(t)}{dt} = A(t)U(t), \quad U(0) = E \text{ is the identity operator [1, p.145] .}$$

2 Preliminaries

Now we formulate the following result, which is proved in [4] for the nonhomogeneous equation (1).

Theorem 1. *Suppose that the homogeneous equation (3) admits an exponential dichotomy on the semi-axes R_+ and R_- with projectors P and Q, respectively. If the operator*

$$D = P - (E - Q) : \mathbf{X} \to \mathbf{X} \tag{4}$$

acting from the Banach space $\mathbf{X}$ onto itself is invertible in the generalized sense [5, p.26], then

(i) in order that solutions of Eq. (1) bounded on the entire real axis exist, it is necessary and sufficient that the function $f(t) \in BC(R, \mathbf{X})$ satisfies the condition

$$\int_{-\infty}^{+\infty} H(t)\, f(t)\, dt = 0; \tag{5}$$

where

$$H(t) = \mathcal{P}_{N(D^*)} Q U^{-1}(t) = \mathcal{P}_{N(D^*)} (E - P) U^{-1}(t),$$

(ii) under condition (5), solutions bounded on the entire axis of Eq. (1) have the form

$$x(t, c) = U(t) P \mathcal{P}_{N(D)} c + (G[f])(t), \quad \forall \ c \in \mathbf{X}, \tag{6}$$

where

$$(G[f])(t) = U(t) \begin{cases} \int_0^t PU^{-1}(s) f(s)\, ds - \int_t^\infty (E - P) U^{-1}(s) f(s)\, ds + \\ \quad + PD^- \left[\int_0^\infty (E - P) U^{-1}(s) f(s)\, ds + \int_{-\infty}^0 QU^{-1}(s) f(s) ds \right], \quad t \geq 0, \\ \int_{-\infty}^t QU^{-1}(s) f(s)\, ds - \int_t^0 (E - Q) U^{-1}(s) f(s)\, ds + \\ + (E - Q) D^- \left[\int_0^\infty (E - P) U^{-1}(s) f(s)\, ds + \int_{-\infty}^0 QU^{-1}(s) f(s)\, ds \right], \ t \leq 0 \end{cases} \tag{7}$$

is the generalized Green operator of the problem for solutions bounded on the entire axis, D^- - is the generalized inverse of D , $mathcal P_{N(D)} = E - D^- D$ and $\mathcal{P}_{N(D^*)} = E - DD^-$, c is an arbitrary constant element of the Banach space $\mathbf{X}$.

3 Main result

We now show that under condition from the theorem 1, the boundary value problem can be solved using the operator $B_0 = lU(\cdot) P \mathcal{P}_{N(D)} : \mathbf{X} \to \mathbf{Y}$.

Theorem 2. *Let's conditions from the theorem 1 are satisfied. If the operator*

$$B_0 : \mathbf{X} \longrightarrow \mathbf{Y}$$

acting from the Banach space $\mathbf{X}$ *into the Banach space* $\mathbf{Y}$ *is invertible in the generalized sense, then*

(i) in order that solutions of boundary value problem (1), (2) exist, it is necessary and sufficient that

$$\mathcal{P}_{N(B_0^*)}(\alpha - l((G[f])(\cdot))) = 0 \ ; \tag{8}$$

(ii) under condition (8) solutions of boundary value problem (1), (2) have the form

$$x(t,\overline{c}) = U(t)P\mathcal{P}_{N(D)}\mathcal{P}_{N(B_0)}\overline{c} + U(t)P\mathcal{P}_{N(D)}B_0^-(\alpha - l(G[f])(\cdot)) + (G[f])(t), \forall \overline{c} \in \mathbf{X},$$

where $(G[f])(\cdot)$ *- is generalized Green operator defined below;* B_0^- *- is generalized inverse of* B_0*,* $\mathcal{P}_{N(B_0^*)}$ *- projector, which project* $\mathbf{X}$ *onto the kernel of adjoint operator* B_0^**.*

Proof. From the theorem 1, we have that the family of bounded solutions of the equation (1) has the form $x(t,c) = U(t)P\mathcal{P}_{N(D)}c + (G[f])(t)$. We substitute this solutions to the equation (2):

$$l(U(\cdot)P\mathcal{P}_{N(D)}c + (G[f])(\cdot)) = \alpha.$$

Since the operator l is linear we have :

$$l(U(\cdot)P\mathcal{P}_{N(D)})c + l((G[f])(\cdot)) = \alpha,$$

and we have finally the operator equation :

$$B_0 c = \alpha - l((G[f])(\cdot)).$$

Since operator B_0 is invertible in the generalized sence , then in order that solutions of the boundary value problem (1),(2) exist it is necessary and sufficient [5] that

$$\mathcal{P}_{N(B_0^*)}(\alpha - l((G[f])(\cdot))) = 0.$$

If this condition is satisfied, then

$$c = \mathcal{P}_{N(B_0)}\overline{c} + B_0^-(\alpha - l((G[f])(\cdot))), \quad \forall \overline{c} \in \mathbf{X}.$$

Then the family of bounded solutions of the boundary value problem (1), (2) has the form:

$$x(t,\overline{c}) = U(t)P\mathcal{P}_{N(D)}\mathcal{P}_{N(B_0)}\overline{c} + U(t)P\mathcal{P}_{N(D)}B_0^-(\alpha - l((G[f])(\cdot))) + (G[f])(t)$$

Remark. If $\mathbf{Y} = \mathbf{X} \times \mathbf{X}$, $lx = (x(+\infty), x(-\infty)) = (\alpha, \alpha) \in \mathbf{X} \times \mathbf{X}$, where α - equilibrium point of (1), then all bounded solutions of boundary value problem (1), (2) are homoclinic paths [6].

4 Examples

1. We now illustrate the assertions proved above. Consider the next boundary value problem

$$\frac{dx}{dt} = A(t)x(t) + f(t), \tag{9}$$

$$lx(\cdot) = x(b) - x(a) = \alpha, \tag{10}$$

where $A(t)$ - is operator in the form of a countably-dimensional matrix that, for every real value t, acts on the Banach space $\mathbf{B} = l_p,\ p \in [1; +\infty)$ and

$$x(t) = col\{x_1(t), x_2(t), \dots x_k(t), \dots\} \ \in \ BC^1(R, l_p),$$

$$f(t) = col\{f_1(t), f_2(t), \dots, f_k(t), \dots\} \ \in \ BC(R, l_p)$$

- are countable vector - columns; $a, b \in R, b > 0, a < 0$;

$$\alpha = col\{\alpha_1, \alpha_2, \dots, \alpha_k, \dots\} \in l_p$$

- constant vector ($\alpha_i \in R, i \in N$).

Consider boundary value problem (9), (10) with the operator

$$A(t) = \begin{pmatrix} \overbrace{th\ t & 0 & 0}^{k} & \dots & \dots \\ 0 & th\ t & 0 & \dots & \dots \\ \dots & \dots & \dots & \dots & \dots \\ 0 & 0 & th\ t & \dots & \dots \\ 0 & 0 & 0 & -th\ t & \dots \\ \dots & \dots & \dots & \dots & \dots \end{pmatrix} : l_p \to l_p. \tag{11}$$

The evolution operator of system (9), (11) has the form:

$$U(t) = \begin{pmatrix} \overbrace{(e^t + e^{-t})/2 & 0 & 0}^{k} & \dots & \dots \\ 0 & (e^t + e^{-t})/2 & 0 & \dots & \dots \\ \dots & \dots & \dots & \dots & \dots \\ 0 & 0 & (e^t + e^{-t})/2 & \dots & \dots \\ 0 & 0 & 0 & 2/(e^t + e^{-t}) & \dots \\ \dots & \dots & \dots & \dots & \dots \end{pmatrix};$$

The operator inverse to $U(t)$ has the form

$$U^{-1}(t) = \begin{pmatrix} \overbrace{2/(e^t + e^{-t}) & 0 & 0}^{k} & \dots & \dots \\ 0 & 2/(e^t + e^{-t}) & 0 & \dots & \dots \\ \dots & \dots & \dots & \dots & \dots \\ 0 & 0 & 2/(e^t + e^{-t}) & \dots & \dots \\ 0 & 0 & 0 & (e^t + e^{-t})/2 & \dots \\ \dots & \dots & \dots & \dots & \dots \end{pmatrix};$$

and the corresponding homogeneous system is exponentially - dichotmous on both semi-axes R_+ and R_- with the projectors

$$P = \begin{pmatrix} \overbrace{0 \quad 0}^{k} & \dots & \dots \\ \dots & \dots & \dots & \dots \\ 0 & 0 & \dots & \dots \\ 0 & 0 & 1 & \dots \\ 0 & 0 & 0 & \dots \\ \dots & \dots & \dots & \dots \end{pmatrix} \quad \text{and} \quad Q = \begin{pmatrix} \overbrace{1 \quad 0 \quad \dots}^{k} & \dots \\ \dots & \dots & \dots & \dots \\ 0 & \dots & 1 & \dots \\ 0 & 0 & 0 & \dots \\ 0 & 0 & 0 & \dots \\ \dots & \dots & \dots & \dots \end{pmatrix}$$

, respectively. Thus, we have

$$D = P - (E - Q) = 0, \quad \mathcal{P}_{N(D)} = \mathcal{P}_{N(D^*)} = E.$$

Since $dimR[\mathcal{P}_{N(D^*)}Q] = k$, then operator $\mathcal{P}_{N(D^*)}Q$ is finite-dimensional:

$$H(t) = [\mathcal{P}_{N(D^*)}Q]U^{-1}(t) = \begin{pmatrix} \overbrace{1 \quad 0 \quad \dots}^{k} & \dots \\ \dots & \dots & \dots & \dots \\ 0 & \dots & 1 & \dots \\ 0 & 0 & 0 & \dots \\ 0 & 0 & 0 & \dots \\ \dots & \dots & \dots & \dots \end{pmatrix} U^{-1}(t) = diag\{H_k(t), 0\},$$

where

$$H_k(t) = \begin{pmatrix} 2/(e^t + e^{-t}) & \dots & 0 \\ \vdots & \ddots & \vdots \\ 0 & \dots & 2/(e^t + e^{-t}) \end{pmatrix} \text{ is a } k \times k - \text{ dimensional matrix .}$$

According theorem 1, for the existence of solutions of system (9), (11) bounded on the entire axis, it is necessary and sufficient that following conditions be satisfied:

$$\int_{-\infty}^{+\infty} H_k(t)f(t)dt = 0 \quad \Leftrightarrow \quad \begin{cases} \int_{-\infty}^{+\infty} \frac{f_1(t)}{e^t + e^{-t}}dt = 0 \\ \dots \\ \int_{-\infty}^{+\infty} \frac{f_k(t)}{e^t + e^{-t}}dt = 0. \end{cases} \tag{12}$$

Thus, in order that system (3), (11) have solutions bounded on the entire axis, it is necessary and sufficient that exactly k conditions be satisfied; the other functions $f_i(t)$ for all $i \geq k + 1$ can be taken arbitrary from the class $BC(R, l_p)$. Moreover, system (3), (11) has countably many linearly independent bounded solutions. For example, as a vector function f from the class $BC(R, l_p)$, one can take an arbitrary vector function whose first k components are odd functions.

For solving boundary value problem we find the matrix B_0 :

$$B_0 = lU(\cdot)P\mathcal{P}_{N(D)} = U(b)P\mathcal{P}_{N(D)} - U(a)P\mathcal{P}_{N(D)},$$

and finally

$$B_0 = \begin{pmatrix} \overbrace{0 \quad 0 \quad \dots}^{k} & \dots & \dots & \dots \\ \dots \quad \dots \quad \dots & \dots & \dots & \dots \\ 0 \quad \dots \quad 0 & \dots & \dots & \dots \\ 0 \quad \dots \quad 0 & \frac{cha-chb}{cha\cdot chb} & \dots & \dots \\ 0 \quad \dots \quad 0 & \dots & \frac{cha-chb}{cha\cdot chb} & \dots \\ \dots \quad \dots \quad \dots & \dots & \dots & \dots \end{pmatrix} : l_p \to l_p.$$

Since $a \neq b$ then operator $\mathcal{P}_{N(B_0^*)}$ have the form :

$$\mathcal{P}_{N(B_0^*)} = \begin{pmatrix} \overbrace{1 \quad 0 \quad \dots}^{k} & \dots & \dots & \dots \\ \dots \quad \dots & \dots & \dots & \dots \\ 0 \quad \dots & 1 & \dots & \dots \\ 0 \quad \dots & 0 & 0 & \dots \\ 0 \quad \dots & 0 & \dots & 0 \\ \dots \quad \dots & \dots & \dots & \dots \end{pmatrix} : l_q \to l_q \ (1/p + 1/q = 1),$$

and

$$G[f](b) - G[f](a) = \begin{pmatrix} -\int_{-\infty}^{a} \frac{2f_1(s)}{e^s+e^{-s}}ds - \int_{b}^{+\infty} \frac{2f_1(s)}{e^s+e^{-s}}ds \\ \dots \\ -\int_{-\infty}^{a} \frac{2f_k(s)}{e^s+e^{-s}}ds - \int_{b}^{+\infty} \frac{2f_k(s)}{e^s+e^{-s}}ds \\ \frac{1}{2}\int_{a}^{b}(e^s + e^{-s})f_{k+1}(s)ds \\ \dots \end{pmatrix}.$$

$$\mathcal{P}_{N(B_0^*)}(\alpha - l(G[f])(\cdot)) = 0 \quad \Leftrightarrow \quad \begin{cases} \int_{-\infty}^{a} \frac{2f_1(s)}{e^s+e^{-s}}ds + \int_{b}^{+\infty} \frac{2f_1(s)}{e^s+e^{-s}}ds = -\alpha_1 \\ \dots \\ \int_{-\infty}^{a} \frac{2f_k(s)}{e^s+e^{-s}}ds + \int_{b}^{+\infty} \frac{2f_k(s)}{e^s+e^{-s}}ds = -\alpha_k. \end{cases} \tag{13}$$

Thus, according to Theorem 2, boundary value problem (9), (10), (11) possesses at least one solution bounded on R if and only if the vector-function f satisfies conditions (12), (13).

2.Consider one-dimensional boundary value problem

$$\frac{dx(t)}{dt} = -tht\ x(t) + f(t),$$

$$lx = (x(+\infty), x(-\infty)) = (\alpha_1, \alpha_2) \in R^2. \tag{14}$$

a) let $f(t) = \frac{2e^{-t}}{e^t+e^{-t}}$ and $(\alpha_1, \alpha_2) = (0, -2)$. The set of bounded solutions which satisfy boundary condition (14) have the form:

$$x(t,c) = \frac{2}{e^t + e^{-t}}\ c - \frac{2e^{-t}}{e^t + e^{-t}} + \frac{2}{e^t + e^{-t}},\ for\ all\ c\ \in R.$$

Integral curves for different values of the parameter c are shown in Figure 1.

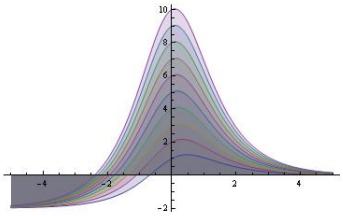

Fig. 1. Integral curves for different values of the parameter c

b) let $f(t) = 2\ tht$ and $(\alpha_1, \alpha_2) = (2, 2)$. In this case equation (1) has equilibrium solution $x_0(t) = 2$ and a set of homoclinic paths have the next form:

$$x(t,c) = \frac{2}{e^t + e^{-t}}\ c + 2 - \frac{4}{e^t + e^{-t}},\ for\ all\ c \in R.$$

Integral curves for different values of the parameter c are shown in Figure 2.

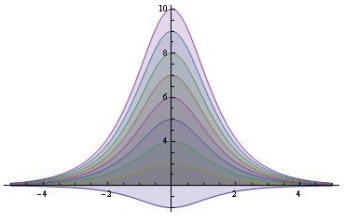

Fig. 2. Integral curves for different values of the parameter c

3. Consider two-dimensional boundary value problem

$$\frac{dx_1(t)}{dt} = -tht\ x_1(t) + f_1(t),$$

$$\frac{dx_2(t)}{dt} = -tht\ x_2(t) + f_2(t),$$

$$l(x_1, x_2) = (x_1(+\infty), x_1(-\infty), x_2(+\infty), x_2(-\infty)) = (\alpha_1, \alpha_2, \alpha_3, \alpha_4) = (0, -2, 2, 2) \in R^4,$$

where $f_1(t) = \frac{2e^{-t}}{e^t+e^{-t}}$, $f_2(t) = 2\ tht$ (direct product of examples 2a, 2b). This problem has a two-parametric family of bounded solutions

$$x_1(t,c_1) = \frac{2}{e^t+e^{-t}}\ c_1 - \frac{2e^{-t}}{e^t+e^{-t}} + \frac{2}{e^t+e^{-t}},$$
$$x_2(t,c_2) = \frac{2}{e^t+e^{-t}}\ c_2 + 2 - \frac{4}{e^t+e^{-t}},$$
$$for\ all\ c_1, c_2 \in R.$$

The phase portrait of this system is shown for different parameters in Figure 3 (in plane x_1, x_2).

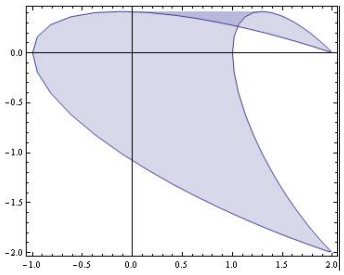

Fig. 3. The phase portrait of system

We see that the portrait resembles a horseshoe.

References

1.Yu. M. Daletskii and M. G. Krein, *Stability of Solutions of Differential Equations in Banach Space*. Nauka, Moscow. 1970 (in Russian).

2.K. J. Palmer. *Exponential dichotomies and transversal homoclinic points.* J. Different. Equat. **55**.-1984. P. 225–256.

3.Sacker R.J., Sell G.R. *Dichotomies for Linear Evolutionary Equaitons in Banach Spaces. Journal of Differential Equations.* 113, 17-67, 1994.

4.A. A. Boichuk and A.A. Pokutnij. Bounded solutions of linear differential equations in Banach space. *Nonlinear Oscillations,* **9**, no 1. - 2006. - P. 3-14; http://www.springer.com/.

5.A. A. Boichuk and A. M. Samoilenko, *Generalized Inverse Operators and Fredholm Boundary-Value Problems*. VSP, Utrecht - Boston. 2004.

6.Guckenheimer J., Holmes Ph. *Nonlinear Oscillations, Dynamical Systems, and Bifurcations of Vector Fields*. 2002. - 235p.


Proceedings, 5th Chaotic Modeling and Simulation International Conference, 12 – 15 June 2012, Athens Greece

Analysis of the Triple Pendulum as a Hyperchaotic System

André E Botha[1] and Guoyuan Qi[2]

[1] Department of Physics, University of South Africa, P.O. Box 392, Pretoria 0003, South Africa
(E-mail: bothaae@unisa.ac.za)
[2] F'SATI and Department of Electrical Engineering, Tshwane University of Technology, Private Bag X680, Pretoria 0001, South Africa
(E-mail: qig@tut.ac.za)

Abstract. An analysis is made of the hyperchaotic behaviour of a triple plane pendulum. It is shown that there are only eight physically distinct equilibrium configurations for the pendulum and that the types of eigen solutions obtained, for the Jacobian matrix evaluated at each equilibrium configuration, are independent of the system parameters. A new method for extracting the periodic orbits of the system is also developed. This method makes use of least-squares minimisation and could possibly be applied to other non-linear dynamic systems. As an example of its use, four periodic orbits, two of which are numerically unstable, are found. Time series plots and Poincaré maps are constructed to investigate the periodic to hyperchaotic transition that occurs for each unstable orbit.
Keywords: Triple pendulum; hyperchaos; fixed points; periodic orbits.

1 Introduction

The present work is motivated by recent interest in studying pendulum systems for possible exploitation in various technological applications. There have been a number of experimental and theoretical investigations aimed at understanding the stability of human gait (manner of stepping) through the use of inverted pendulum models [1,2]. Experimental investigations of either simple or coupled electro-mechanically driven pendulums have been undertaken with the view of developing more precise conditions for the onset of chaos in such systems [3,4]. Also, a triple pendulum suspension system has been developed to seismically isolate optical components on the GEO 600 interferometric gravitational wave detector [5]. The latter development has allowed the detector to achieve a seismic noise sensitivity level which is well below the level from thermal noise.

Coupled pendulums with obstacles have been used to model real mechanical systems that exhibit nonlinear phenomena such as resonances, jumps between different system states, various continuous and discontinuous bifurcations, symmetry breaking and crisis bifurcations, pools of attractions, oscillatory-rotational attractors, etc. [6–9]. In Ref. [9], for example, it has

been shown that a triple pendulum model can provide insight into the real, highly-complicated dynamics of a piston connecting-rod crankshaft system.

An experimental triple pendulum has been constructed by Awrejcewicz *et al.* [10]. This pendulum has been analysed numerically and experimentally, and good agreement has been obtained between the mathematical model and the real system. In the present work, higher order effects that pertain to specific experimental systems, like [10], are neglected. For example, we have not included finer details of the frictional forces that act on the joints of the pendulum, or asymmetries in its driving mechanism. One of the motivating factors for neglecting such higher order effects is the correspondence that exists between the equations for a damped simple pendulum, driven by a constant torque, and the well-known phenomenological model of a superconducting Josephson junction [4,11]. It is thought that our somewhat simplified model of the triple pendulum could, with minor modifications, serve as a useful mechanical analogy for a series system of three resistively coupled Josephson junctions.

This paper is organised as follows. In Section 2, the basic model and equations are described. The system is linearised at its equilibria in Section 3. In Section 4 a new method is developed for finding the periodic orbits of the system, based on least-squares minimisation. Four examples of found periodic orbits are discussed, including their time series and Poincaré maps. In two of the examples interesting periodic-hyperchaotic transitions are observed. Section 5 concludes with a discussion of the main advantages and possible disadvantages of the new method.

2 Description of model and equations

The current work is a continuation of our previous work [12], in which a three-dimensional animation of a model triple plane pendulum was created by using the *Visual* module in the *Python* programming language [14]. As shown in Fig. 1, the model consists of a series of absolutely rigid bars which form the three links of the pendulum (shown in red, green and blue). Additional point-like masses are attached to the bottom of each link (shown as yellow cylindrical disks).

The equations for the pendulum have been derived in a very general form which allows each link in the pendulum to have an arbitrary moment of inertia [8]. In the present work we consider the equations for a pendulum consisting of three point masses, i.e. we neglect the moments of inertia of the three links shown in Fig. 1. The equations for this special case are given in Appendix A of Ref. [12] in the form,

$$\frac{\mathrm{d}\mathbf{x}}{\mathrm{dt}} = \mathbf{f}\left(\mathbf{x}, \alpha, t\right) \ . \tag{1}$$

In Eq. (1), $\alpha \equiv (m_1, m_2, m_3, \ell_1, \ell_2, \ell_3, c_1, c_2, c_3)$, represents the system parameters, where c_{1-3} model the viscous damping in each joint. The vector

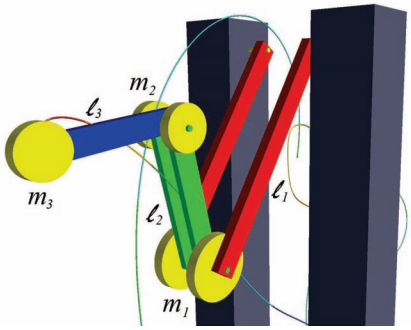

Fig. 1. Visualisation of the triple plane pendulum. The pendulum is made of rigid bars (two of length ℓ_1, two of length ℓ_2 and one of length ℓ_3) to which point-like masses may be attached (two of mass $\frac{m_1}{2}$, two of mass $\frac{m_2}{2}$ and one of mass m_3). The pendulum is assumed to be under the influence of gravity ($g = 9.81\,\mathrm{ms}^{-2}$) and in vacuum. Also shown is the trajectory followed by the centre of m_3.

$\mathbf{x} \equiv (\theta_1, \theta_2, \theta_3, \dot{\theta}_1, \dot{\theta}_2, \dot{\theta}_3)$, where θ_{1-3} are the angles made between the vertical and each of the three links.

3 Linearisation at the equilibria

The spatial distribution and local dynamical characteristics of the equilibria of a system greatly influence its nonlinear dynamics. Since the un-damped pendulum is conservative, having only time independent constraints, its equilibria are defined by the vanishing of the generalised forces Q_i [13], i.e. by,

$$Q_i = \frac{\partial V}{\partial x_i} = 0 \;\; (\text{for } i = 1, 2, 3) \;, \tag{2}$$

where $V(x_1, x_2, x_3) = (m_1 + m_2 + m_3)\, g\ell_1 \cos x_1 + (m_2 + m_3)\, g\ell_2 \cos x_2 + m_3 g\ell_3 \cos x_3$ is the potential energy. The solutions to Eq. (2) produce eight physically distinct equilibria, as shown in Fig. 2.

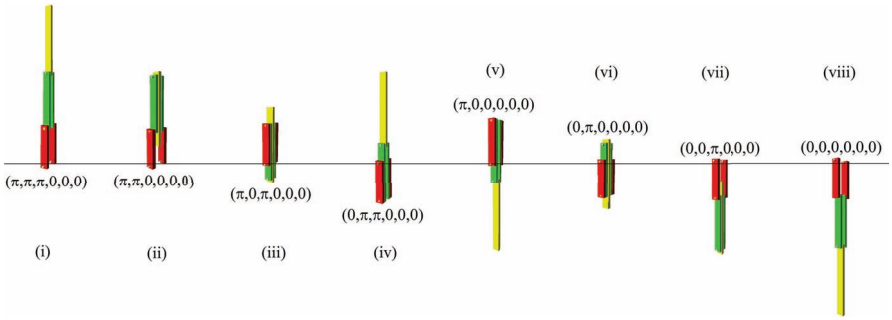

Fig. 2. The eight physically distinct equilibrium configurations of the pendulum. Configurations (i) to (vii) are unstable. Configuration (viii) is stable.

To characterize the linearised dynamics of the system near each equilibrium, we calculate the Jacobian matrix of the system and determine its eigenvalues at the equilibria. The Jacobian matrix, evaluated at any of the

equilibria, has the form

$$\mathbf{J} = \begin{pmatrix} 0 & 0 & 0 & 1 & 0 & 0 \\ 0 & 0 & 0 & 0 & 1 & 0 \\ 0 & 0 & 0 & 0 & 0 & 1 \\ \pm J_1 & \pm J_2 & 0 & 0 & 0 & 0 \\ \pm J_3 & \pm J_4 & \pm J_5 & 0 & 0 & 0 \\ 0 & \pm J_6 & \pm J_7 & 0 & 0 & 0 \end{pmatrix} , \tag{3}$$

where $J_1 = g\left(m_1 + m_2 + m_3\right) / \left(\ell_1 m_1\right)$, $J_2 = g\left(m_2 + m_3\right) / \left(\ell_1 m_1\right)$, $J_3 = g\left(m_1 + m_2 + m_3\right) / \left(\ell_2 m_1\right)$, $J_4 = g\left(m_1 + m_2\right)\left(m_2 + m_3\right) / \left(\ell_2 m_1 m_2\right)$, $J_5 = gm_3 / \left(\ell_2 m_2\right)$, $J_6 = g\left(m_2 + m_3\right) / \left(\ell_3 m_2\right)$ and $J_7 = g\left(m_2 + m_3\right) / \left(\ell_3 m_2\right)$. To evaluate $\mathbf{J}$ at any particular equilibrium, the signs preceding J_{1-7} in Eq. (3) must be chosen according to the convention given in Table 1.

Equilibrium config.	J_1	J_2	J_3	J_4	J_5	J_6	J_7
(i) $(\pi, \pi, \pi, 0, 0, 0)$	+	-	-	+	-	-	+
(ii) $(\pi, \pi, 0, 0, 0, 0)$	+	-	-	+	-	+	-
(iii) $(\pi, 0, \pi, 0, 0, 0)$	+	-	+	-	+	-	+
(iv) $(\pi, 0, 0, 0, 0, 0)$	+	-	+	-	+	+	-
(v) $(0, \pi, \pi, 0, 0, 0)$	-	+	-	+	-	-	+
(vi) $(0, \pi, 0, 0, 0, 0)$	-	+	-	+	-	+	-
(vii) $(0, 0, \pi, 0, 0, 0)$	-	+	+	-	+	-	+
(viii) $(0, 0, 0, 0, 0, 0)$	-	+	+	-	+	+	-

Table 1. The choice of signs preceding J_{1-7} in Eq. (3) for each of the eight possible equilibrium configurations listed in the left hand column. These combinations of signs should also be used in the definitions of b, c and d in Eq. (4).

The eigenvalues η of the Jacobian matrix were determined by solving the characteristic equation $\det(\mathbf{J} - \eta\mathbf{1}) = 0$, where $\mathbf{1}$ is the 6×6 identity matrix. By choosing all the signs in Eq. (3) to be positive, we found the characteristic equation,

$$0 = a\eta^6 + b\eta^4 + c\eta^2 + d \ , \tag{4}$$

where $a = 1$, $b = J_1 J_4 J_7 - J_1 J_5 J_6 - J_2 J_3 J_7$, $c = J_1 J_4 - J_2 J_3 - J_1 J_7 - J_4 J_7 + J_5 J_6$ and $d = J_7 - J_1 - J_4$. In the expressions for b, c and d the correct combination of signs, for a particular equilibrium, must once again be chosen from Table 1. For example, for the second equilibrium, row (ii) in Table 1, one obtains $d = (-)\, J_7 - (+)\, J_1 - (+)\, J_4$.

Since Eq. (4) is a cubic polynomial in η^2, its solutions could be written algebraically [15]. The discriminant of each eigen solution was then used to prove that the type of solution associated with a particular equilibrium configuration is independent of the system parameters. These results are presented in Table 2. To present the complete analysis of the fixed points associated with each equilibrium in Table 2 is beyond the scope of the present article. Briefly, our analysis reveals that (i) to (vii) may be associated with various types of saddle points (depending on the parameter values) and that (viii) will always remain a nonlinear centre.

Table 2. The various types of eigenvalues obtained by solving Eq. (4) at each of the eight possible equilibrium configurations.

Equilibrium config.	Stability	Eigenvalues of **J**
(i) $(\pi, \pi, \pi, 0, 0, 0)$	unstable	all real
(ii) $(\pi, \pi, 0, 0, 0, 0)$	unstable	4 real, 2 imaginary
(iii) $(\pi, 0, \pi, 0, 0, 0)$	unstable	4 real, 2 imaginary
(iv) $(\pi, 0, 0, 0, 0, 0)$	unstable	2 real, 4 imaginary
(v) $(0, \pi, \pi, 0, 0, 0)$	unstable	4 real, 2 imaginary
(vi) $(0, \pi, 0, 0, 0, 0)$	unstable	2 real, 4 imaginary
(vii) $(0, 0, \pi, 0, 0, 0)$	unstable	2 real, 4 imaginary
(viii) $(0, 0, 0, 0, 0, 0)$	stable	all imaginary

4 New method for locating periodic orbits

Knowledge of the periodic orbits and their stability is an important aspect of understanding chaotic systems and therefore a great deal of research has already gone into developing more efficient methods for discovering the periodic orbits and periods of non-linear dynamic systems. See, for example, Refs. [16–18], and references therein. In this section we will develop a new method for finding the periodic orbits by making use of the Levenberg-Marquardt algorithm for least-squares estimation of nonlinear parameters [19].

Assume that the system has a periodic orbit with principle period T. As pointed out by Li and Xu [17], it is convenient to use T as one of the optimisation parameters. We therefore re-write Eq. (1) in terms of a dimensionless time parameter τ, by setting $t = T\tau$. This substitution produces the equivalent equation,

$$\frac{\mathrm{d}\mathbf{x}}{\mathrm{d}\tau} = T\mathbf{f}\left(\mathbf{x}, \alpha, T\tau\right) \ . \tag{5}$$

Since τ is measured in units of T, Eq. (5) has the advantage that it can be integrated over exactly one period, by letting τ run from zero to one.

In order to search for periodic orbits we define the residual (error vector),

$$\mathbf{R} = \left(\mathbf{x}\left(1\right) - \mathbf{x}\left(0\right), \mathbf{x}\left(1 + \Delta\tau\right) - \mathbf{x}\left(\Delta\tau\right), \ldots, \mathbf{x}\left(1 + n\Delta\tau\right) - \mathbf{x}\left(n\Delta\tau\right)\right), \tag{6}$$

where $\Delta\tau$ is the integration step size. In Eq. (6), n is an integer which must be chosen large enough to ensure that $\mathbf{R}$ has a greater number of components than the number of quantities which are to be optimised simultaneously. This choice is required by the Levenberg-Marquardt algorithm, which is used to locate the global minimum in $\mathbf{R}$ (note that $\mathbf{R} = \mathbf{0}$ for periodic orbits). In the case of the un-damped pendulum, for example, if all possible quantities are to be optimised simultaneously, i.e. six initial conditions, plus six parameters, plus the period (13 quantities); then one must choose $n \geq 2$. The smallest possible choice for this case is $n = 2$, which produces a residual with $6(n+1) = 18$ components (see Eq. 6).

The definition of $\mathbf{R}$ requires the system to be integrated from $\tau = 0$ to $\tau = 1 + n\Delta\tau$. In the present work we have used a fourth-order Runge-Kutta integration scheme with $n = 3$ and $\Delta\tau = 1/N$, where $N = 2000$. We have implemented the method in the *Python* programming language [14]. The module *Scipy.optimize* contains the function *leastsq*, which makes use of a modified Levenberg-Marquardt algorithm [20].

When applied to the triple pendulum, the method produces a surprisingly large number of (numerically) stable and unstable periodic orbits. Many of the found orbits at first appear to be qualitatively similar (when viewed on a screen), but are in fact quantitatively different, when studied numerically. In Fig. 3 we have plotted four examples of different periodic orbits that were found. Figure 3 (a) shows a stable symmetric orbit of period

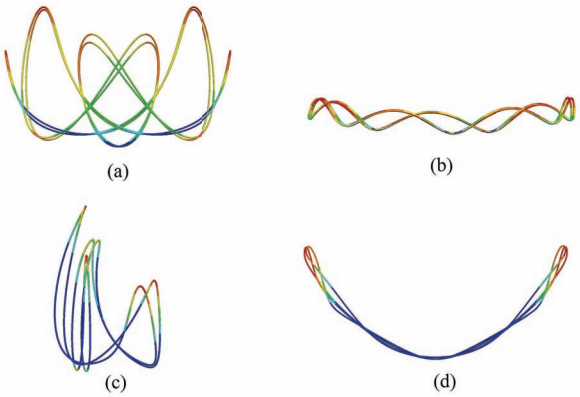

Fig. 3. Four different periodic orbits followed by the centre of m_3, i.e. here $Y = -\ell_1 \cos x_1 - \ell_2 \cos x_2 - \ell_3 \cos x_3$ is plotted against $X = \ell_1 \sin x_1 + \ell_2 \sin x_2 + \ell_3 \sin x_3$, for the first 10 s. (a) Symmetric and stable. (b) Broken-symmetric and stable. (c) Broken-symmetric and unstable. (d) Symmetric and unstable. The colour of each orbit represents the speed of m_3 in the range zero (red) to 2 ms^{-1} (blue).

$T = 3.0363595$ s. One point on the orbit is (−0.20813379, −0.47019033, 0.80253405, −4.0363589, 4.42470966, 8.3046730), with the parameters $m_{1-3} = 0.1$ kg, $\ell_1 = 0.15$ m and $\ell_{2-3} = 0.1$ m. Figure 3 (b) shows a stable broken-symmetric orbit of period $T = 2.78866884$ s. One point on the orbit is (−0.22395671, 0.47832902, 0.22100014, −1.47138911, 1.29229544, −0.27559337), with the parameters $m_1 = 0.1$ kg, $m_2 = 0.2$ kg, $m_3 = 0.1$ kg, $\ell_1 = 0.15$ m, $\ell_2 = 0.2$ m and $\ell_3 = 0.3$ m. The Lyapunov exponents for the orbits shown in Figs. 3 (a) and (b) confirm that the orbits are periodic.

Figure 3 (c) shows an unstable broken-symmetric orbit of period $T = 3.23387189$ s. One point on the orbit is (−0.78539816, 0.79865905, 0.72867705, 0.74762606, 2.56473963, −2.05903234), with the parameters $m_1 = 0.35$ kg, $m_2 = 0.2$ kg, $m_3 = 0.3$ kg, $\ell_1 = 0.3$ m, $\ell_2 = 0.2$ m and $\ell_3 = 0.25$ m. The Lyapunov exponents, sampled every 0.0005 s for 2000 s, con-

firm that this orbit is hyperchaotic, with $\lambda_1 = 0.90$, $\lambda_2 = 0.19$ and $\lambda_3 = 0.002$. Figure 3 (d) shows an unstable symmetric orbit of period $T = 3.44620156\,\mathrm{s}$. One point on the orbit is (1.30564176, 1.87626915, 1.13990186, 0.75140557, 1.65979939, −2.31442362), with the parameters $m_1 = 0.35\,\mathrm{kg}$, $m_2 = 0.2\,\mathrm{kg}$, $m_3 = 0.3\,\mathrm{kg}$, $\ell_1 = 0.3\,\mathrm{m}$, $\ell_2 = 0.2\,\mathrm{m}$ and $\ell_3 = 0.25\,\mathrm{m}$. The Lyapunov exponents, sampled every $0.0005\,\mathrm{s}$ for $2000\,\mathrm{s}$, confirm that the orbit is also hyperchaotic, with $\lambda_1 = 2.95$, $\lambda_2 = 1.10$ and $\lambda_3 = 0.004$.

To investigate the rapid transition that occurs from periodic to hyperchaotic the time series and Poincaré maps of each orbit have been studied. Figure 4(a) shows the time series of x_6 for each of the four orbits.

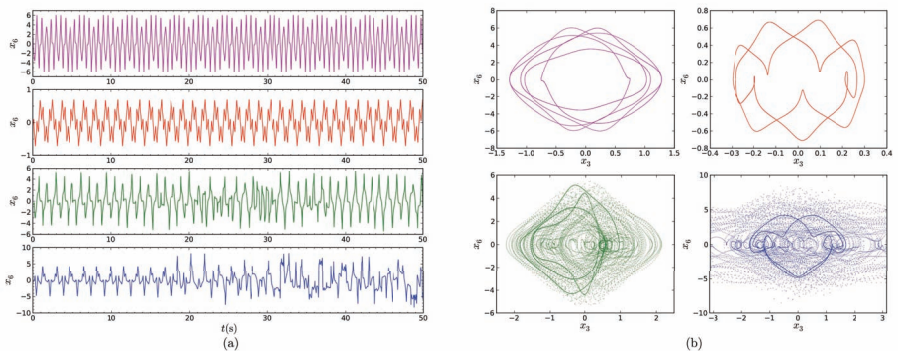

Fig. 4. (a) Time series of x_6 for the orbits discussed in connection with Figs. 3 (a) magenta (top), (b) red, (c) green and (d) blue (bottom). (b) The corresponding Poincaré maps. Parameter values and initial conditions are as for Fig. 3.

The corresponding Poincaré maps, shown in Fig. 4 (b), were constructed by sampling the trajectories every $0.001\,\mathrm{s}$, for $100\,\mathrm{s}$. For this relatively short time interval the periodic parts of the two unstable orbits are still clearly visible within the surrounding (so-called) stochastic layer that is thought to replace the region of destroyed separatrices [21].

5 Discussion and conclusion

The equations for a triple plane pendulum, consisting of three point masses connected by massless links, have been analysed. It was shown that there are only eight physically distinct equilibrium configurations for the pendulum and that the type of eigen solutions obtained for the linearised system at each equilibrium is independent of the system parameter values. A new method for extracting the periodic orbits of the system was also developed. The new method exploits the high-efficiency of the modified Levenberg-Marquardt algorithm. It is simple to implement and does not require the computation of the Jacobian matrix. In addition, the minimisation algorithm may easily

be constrained in order to restrict the search to specific regions of the phase space; for example, to a constant energy surface. One possible disadvantage of the method is that it does not discriminate between unstable and stable periodic orbits. However, this aspect of the method may in fact be an important advantage, since it enables the method to be used for studying the coexistence of both regions of stable dynamics and hyperchoas within the phase space.

Acknowledgments

This work is based upon research supported by the National Research Foundation of South Africa (Nos. IFR2011033100063 and IFR2009090800049) and the Eskom–Trust/Tertiary Education Support Programme of South Africa.

References

1.K. G. Eltohamy and C. Kuo, Int. J. of Systems Science **30**, 505 (1999).
2.T. Furata *et al.*, Robotics Autonomous Systems **37**, 81 (2001).
3.A. S. de Paula, M. A. Savi, and F. H. I. Pereira-Pinto, Journal of Sound and Vibration **294**, 585 (2006).
4.M. Gitterman, *The Chaotic Pendulum* (World Scientific, Singapore, 2010).
5.M. V. Plissi *et al.*, Review of Scientific Instruments **71**, 2539 (2000).
6.G. Kudra, Ph.D. thesis, Technical University of Lódź, 2002.
7.J. Awrejcewicz and C. H. Lamarque, in *World Scientific Series on Nonlinear Science*, Vol. 45 of *Series A*, ed. L. Chua (World Scientific, Singapore, 2003).
8.J. Awrejcewicz, G. Kudra, and C. H. Lamarque, Int. J. of Bifurcation and Chaos **14**, 4191 (2004).
9.J. Awrejcewicz and G. Kudra, Nonlinear Analysis **63**, 909 (2005).
10.J. Awrejcewicz *et al.*, Int. J. of Bifurcation and Chaos **18**, 2883 (2008).
11.S. H. Strogatz, *Nonlinear Dynamics and Chaos* (Addison-Wesley, Reading, 1994).
12.A. E. Botha and G. Qi, in *Proceedings of the 56th Annual Conference of the South African Institute of Physics*, edited by I. Basson and A. E. Botha (University of South Africa, Pretoria, 2011), p. 123, ISBN: 978-1-86888-688-3. Available online at www.saip.org.za.
13.H. Goldstein, *Classical Mechanics*, 2nd ed. (Addison-Wesley, Reading, 1980), p. 243.
14.W. J. Chun, *Core Python Programming* (Prentice Hall, New Jersey, 2007).
15.W. Press, S. Teukolsky, W. Vetterling, and B. Flannery, *Numerical Recipes*, 3rd ed. (Cambridge University Press, New York, 2007), p. 228.
16.T. Zhou, J. X. Xu, and C. L. Chen, J. Sound and Vibration **245**, 239 (2001).
17.D. Li and J. Xu, Engineering with Computers **20**, 316 (2005).
18.D. Li and S. Yang, Chinese Journal of Applied Mechanics **28**, 349 (2011).
19.D. Marquardt, SIAM Journal of Applied Mathematics **11**, 431 (1963).
20.H. P. Langtangen, *Python Scripting for Computational Science* (Springer Verlag, Berlin, 2004), p. 161. Also see www.scipy.org.
21.G. M. Zaslavsky, *The Physics of Chaos in Hamiltonian Systems*, 2nd ed. (Imperial College Press, Singapore, 2007), p. 2.


Proceedings, 5th Chaotic Modeling and Simulation International Conference, 12 – 15 June 2012, Athens Greece

Observation of Chaotic behaviour in the CCJJ+DC model of Coupled Josephson Junctions

André E Botha[1] and Yu. M. Shukrinov[2]

[1] Department of Physics, University of South Africa, P.O. Box 392, Pretoria 0003, South Africa
(E-mail: bothaae@unisa.ac.za)
[2] Bogoliubov Laboratory of Theoretical Physics, Joint Institute for Nuclear Research, Dubna, Moscow Region, 141980, Russia
(E-mail: shukrinv@theo.jinr.ru)

Abstract. Erratic behaviour in the simulated current-voltage characteristics of coupled intrinsic Josephson junctions, for certain ranges of the parameters, are observed and are shown to be chaotic in origin. In order to demonstrate the chaotic origin of the erratic behaviour, the Lyapunov exponents for the system are calculated. System trajectories and their Poincaré maps are used to confirm the chaotic signature obtained from the Lyapunov spectrum in certain ranges of the bias current, below the break point current.
Keywords: Chaos; Hyperchaos; CCJJ+DC model; Intrinsic Josephson Junctions.

1 Introduction

Systems of coupled intrinsic Josephson junctions (IJJs) are prospective candidates for the development of superconducting electronic devices [1]. Questions about their dynamics are, for a variety of reasons, of great technological importance [2]. For example, systems of junctions can produce much greater power output that a single junction and they also provide a model which may help to elucidate the physics of high temperature superconductors (HTSC) [3,4]. The intrinsic Josephson effect (IJE) [5], i.e. tunneling of Cooper pairs between superconducting layers inside of strongly anisotropic layered HTSC, provides a further motivation for considering HTSC as stacks of coupled Josephson junctions. The IJE also plays an important role in determining the current voltage characteristics (CVC) of tunneling structures based on HTSC and the properties of the vortex structures in these materials.

Although there has been a recent report on the hyperchaotic behaviour of an array of two resistive-capacitive-inductive-shunted Josephson junctions [6], the so-called RCLSJJ model [7], chaotic behaviour does not feature in the literature on other closely-related phenomenological models; such as, the capacitively-coupled model (CCJJ) [8], the resistive-capacitive shunted model (RCSJJ) [5,9], or the CCJJ plus diffusion current (DC) model [10,11] of the present work. One possible reason for the comparatively late discovery of

chaos in these systems may be that the (often subtle) chaotic features may have been masked by numerical instability and added noise in simulations.

This paper is organized as follows. In Section 2 we present the CCJJ+DC model and describe the numerical method used to calculate the Lyapunov exponents. In Section 3 we describe the observation of erratic behaviour in the CVC, which led to the discovery of chaos in the model. In section 4 we demonstrate that the erratic behaviour is chaotic in origin by looking as the Lyapunov exponents, system trajectories and Poincaré maps. In Section 5 we conclude that the erratic behaviour is chaotic in origin and that experimental investigations are required to ascertain whether this feature of the model is observable in real systems that satisfy the assumptions of the CCJJ+DC model. We also suggest that further work could be done on developing methods for controlling the observed chaos (hyperchaos) in this model.

2 Theory and simulation methods

2.1 The CCJJ+DC model

We solve the system of dynamical equations for the gauge-invariant phase differences $\varphi_\ell(\tau) = \theta_{\ell+1}(\tau) - \theta_\ell(\tau) - \frac{2e}{\hbar}\int_\ell^{\ell+1} dz A_z(z,\tau)$ between superconducting layers (S-layers), for stacks consisting of different numbers of IJJs, within the framework of the CCJJ+DC model [12,13]. In this model, θ_ℓ is the phase of the order parameter in the ℓth S-layer and A_z is the vector potential in the insulating barrier. For a system of N junctions the equations are,

$$\frac{d\varphi_\ell}{d\tau} = \sum_{\ell'=1}^{N} A_{\ell\ell'} V_{\ell'} \quad \text{and} \tag{1}$$

$$\frac{dV_\ell}{d\tau} = I - \sin\varphi_\ell - \beta \sum_{\ell'=1}^{N} A_{\ell\ell'} V_{\ell'} \ , \tag{2}$$

where $\ell = 1, 2, \ldots, N$ and the matrix A contains coupling parameters such as α. Note that A differs in form depending on whether periodic or non-periodic boundary conditions (BCs) are used [14]. The dissipation parameter β is related to the McCumber parameter β_c as $\beta = 1/\sqrt{\beta_c}$. For the purpose of numerical simulations we make use of a dimensionless time parameter $\tau = t\omega_p$, where $\omega_p = \sqrt{2eI_c/(\hbar C)}$ is the plasma frequency, I_c is the critical current and C is the capacitance. We measure the DC voltage on each junction V_ℓ in units of the characteristic voltage $V_c = \hbar\omega_p/(2e)$ and the bias current I in units of I_c. The critical currents in these (series) systems can typically range from 1 to 1000 μA, corresponding to voltages of $RI_c \sim 1$ mV across individual junctions. Further details concerning this model can be found in Refs. [14,15]

2.2 Calculation of Lyapunov exponents

The Lyapunov exponents of a nonlinear dynamical system provide a quantitative measure of the degree of chaos inherent in the system, i.e. they quantify the sensitivity of the system to changes in initial conditions [16]. Usually one Lyapunov exponent is associated with each independent coordinate in the system. The numerical value of this exponent then characterizes the long term average exponential convergence (negative exponent) or divergence (positive exponent) of that coordinate with respect to some arbitrarily small initial separation.

Although the calculation of the Lyapunov exponents is in principle straight forward, in numerical calculations one has to guard against cumulative round-off errors which occur because of the exponential manner in which the small initial differences in coordinates may be amplified. Since real experimental data sets are typically small and noisy, it has taken a sustained effort to develop efficient algorithms for estimating the Lyapunov exponents associated with chaotic data sets [17–20]. In the preset simulations, since the system of Eqns. (1) and (2) are know in analytical form, we make use of the well-known algorithm by Wolf *et al.* [17]. Unlike some other methods, which only calculate the maximal Lyapunov exponent [21,22], the algorithm by Wolf *et al.* calculates the full spectrum of Lyapunov exponents and thus allows one to distinguish between chaotic attractors, which are characterised by only one positive exponent, and hyperchaotic attractors, which is characterised by more than one positive exponent.

In addition to Eqs. (1) and (2), the algorithm by Wolf *et al.* requires analytical expressions for the action of the system Jacobian $\mathbf{J}$ on an arbitrary column vector $\mathbf{x} = (\varphi_1,\varphi_2,\ldots,\varphi_N,V_1,V_2,\ldots,V_N)^T$ in the (φ, V) coordinate space. For the present system the action of $\mathbf{J}$ on $\mathbf{x}$ is given by

$$\mathbf{Jx} = \begin{pmatrix} A_{11}V_1 + A_{12}V_2 + \ldots + A_{1N}V_N \\ A_{21}V_1 + A_{22}V_2 + \ldots + A_{2N}V_N \\ \vdots \\ A_{N1}V_1 + A_{N2}V_2 + \ldots + A_{NN}V_N \\ -\varphi_1\cos\varphi_1 - \beta A_{11}V_1 - \beta A_{12}V_2 - \ldots - \beta A_{1N}V_N \\ -\varphi_2\cos\varphi_2 - \beta A_{21}V_1 - \beta A_{22}V_2 - \ldots - \beta A_{2N}V_N \\ \vdots \\ -\varphi_N\cos\varphi_N - \beta A_{N1}V_1 - \beta A_{N2}V_2 - \ldots - \beta A_{NN}V_N \end{pmatrix} \tag{3}$$

To calculate the Lyapunov exponents for a particular current I, we typically used 30000 dimensionless time steps, with a step size of $\Delta\tau = 0.2$. In all our calculations the number of steps and step size were chosen so that the magnitude of the zero exponent always converged to a value which was at least two orders of magnitude smaller than the magnitude of the smallest non-zero exponent. A fifth-order Runge-Kutta integration scheme was used.

3 Observation of erratic behaviour in the CVC

Erratic behaviour was first observed in the simulated CVC for certain ranges of parameter values. Figure 1 presents the simulated outermost branches in the CVC for a stack of nine IJJs. Here V is the sum of the time averaged

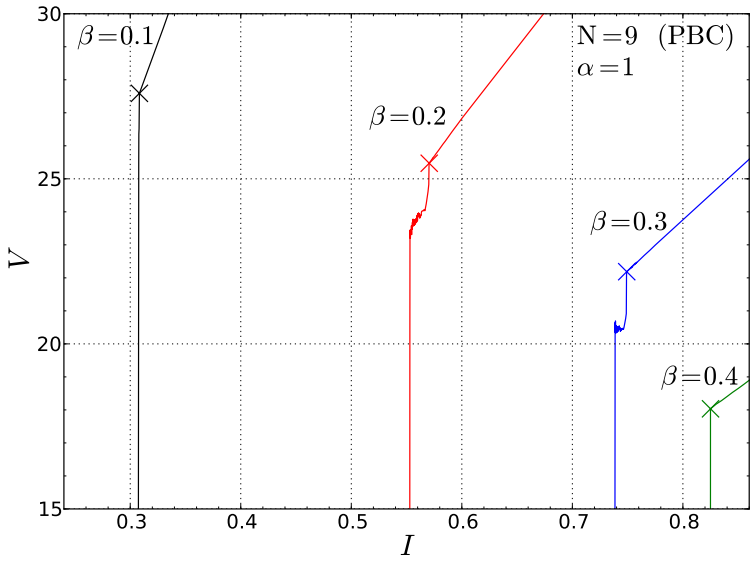

Fig. 1. Simulated outermost branches of the current voltage characteristics of an array with nine IJJ with $\alpha = 1$ and periodic boundary conditions (PBC). The curves for four different values of β are shown. The break point of each curve has been marked by a cross.

voltages across each junction, i.e. $V = \langle V_1 \rangle + \langle V_2 \rangle + \ldots + \langle V_9 \rangle$, and I is bias current through the stack. As explained in Section 2.1, V and I are in units of V_c and I_c respectively. In Fig. 1 one can see the variation of the branch slope and the breakpoint (marked by a cross), for the four different values of dissipation parameter. As expected, the value of the break point current increases with increasing β; however, for $0.1 < \beta < 0.4$ the break point boarders on a so-called break point region (BPR). In Fig. 1 this region can be clearly seen to the left of the break points for the $\beta = 0.2$ and $\beta = 0.3$ curves. For these two values of β, erratic behaviour is observed to the left of each breakpoint. Initially this erratic behaviour was thought to be numerical in origin; however, as we will demonstrate in the next section, it is in fact chaotic.

4 Results and discussion

4.1 Demonstration of chaotic behaviour via Lyapunov exponents

Since we were unable to account for the observed erratic behaviour in terms of numerical instability, we decided to check whether or not the system is chaotic by calculating its Lyapunov exponents according to the method described in Section 2.2. Typical results are shown in Fig. 2, for a stack of seven junctions, using the PBC. Here the left vertical axis is for the Lyapunov exponents

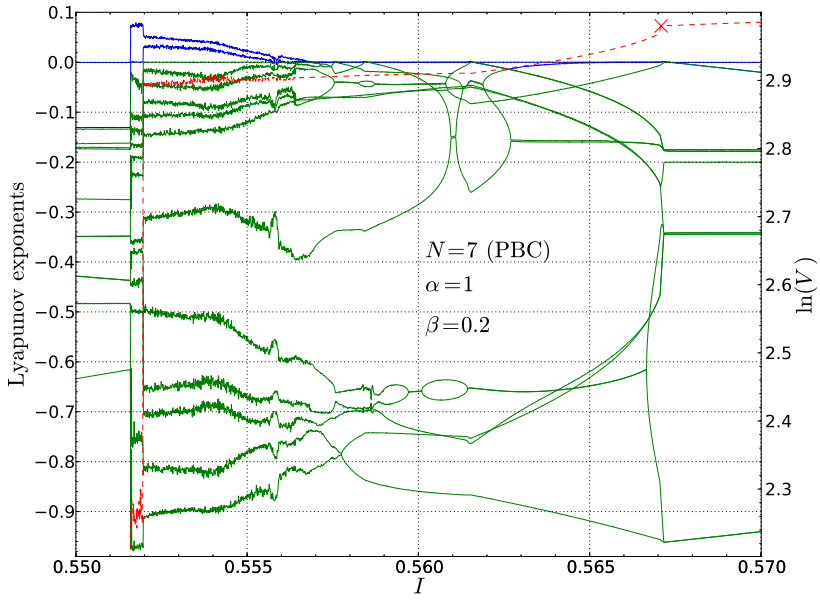

Fig. 2. Lyapunov exponents and CVC for a stack of seven IJJs with periodic boundary conditions.

$(\lambda_1, \ldots, \lambda_{14})$, while the right vertical axis is for $\ln(V)$ (red dashed curve). The largest two Lyapunov exponents, λ_1 and λ_2 (plotted in blue) both become positive exactly over the range of currents for which the erratic behaviour in V was observed, indicating that this system is hyperchaotic within the range $0.5520 < I < 0.5570$. In this range, as the current is decreased, λ_1 and λ_2 steadily increase, reaching their respective maxima of 0.052 and 0.031. At $I \approx 0.5520$ the system makes an abrupt transition to one of the inner branches of the CVC, over the range $0.5515 < I < 0.5520$. For the inner branch there is only one positive Lyapunov exponent ($\lambda_1 = 0.075$), which suggests that this transition may be associated with a change in the dynamics of the system,

from hyperchaotic to chaotic. We have also performed other simulations at different parameter values and for N in the range 7-13, using both the PBC and NPBC. In all cases, for which erratic behaviour in the CVC was observed, we found either one or two positive Lyapunov exponent.

4.2 Comparison of system trajectories

To further verify that the observed behaviour is chaotic (hyperchaotic), we also looked at the system trajectory for a variety of different parameter values and initial conditions. Our observations are consistent with the values obtained for the Lyapunov exponents. For example, Fig. 3 shows a projection onto the $\varphi_3 V_5$-plane of two different trajectories corresponding to a nine junction system ($N = 9$) with periodic boundary conditions and the parameters $\alpha = 1$ and $\beta = 0.2$. Both trajectories correspond to the outer branch of the

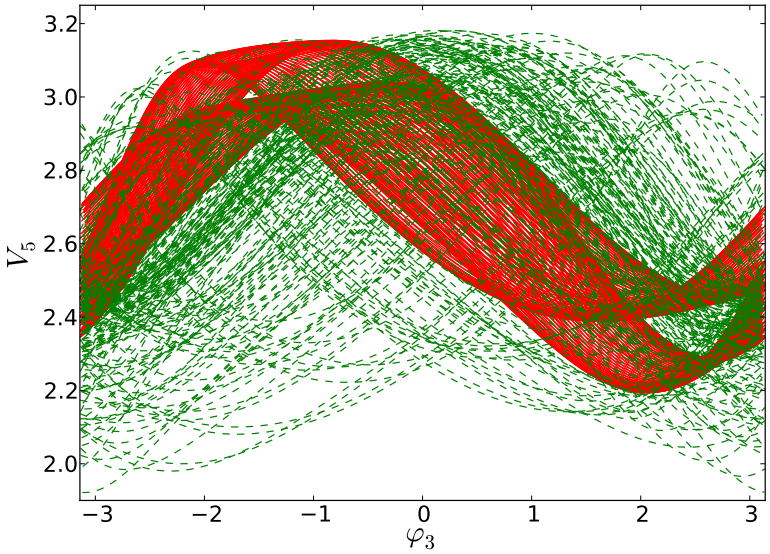

Fig. 3. A projection of two different system trajectories for a stack of nine IJJs with periodic boundary conditions. The solid red curve corresponds to a current above the break point value and is quasi-periodic, while the dashed green curve corresponds to a current below the break point, where the system is hyperchaotic.

CVC and have been integrated for 250 dimensionless time units. The solid red trajectory appears to be quasi-periodic, corresponding to $I = 0.5650$ and zero maximal Lyapunov exponent. The dashed green trajectory is hyperchaotic, corresponding to $I = 0.5575$, with the three largest exponents given by $\lambda_1 = 0.035$, $\lambda_2 = 0.022$ and $\lambda_3 = 0.00005$. In this figure the quasi-periodic

nature of the non-chaotic trajectory (solid red curve) is clearly discernible from the hyperchaotic trajectory (dashed green curve).

4.3 Poincaré maps

To investigate further the differences between regular and chaotic regimes of the system, several Poincaré maps were constructed. Figure 4 shows a comparison of the maps for the trajectories described in Fig. 3. Here the

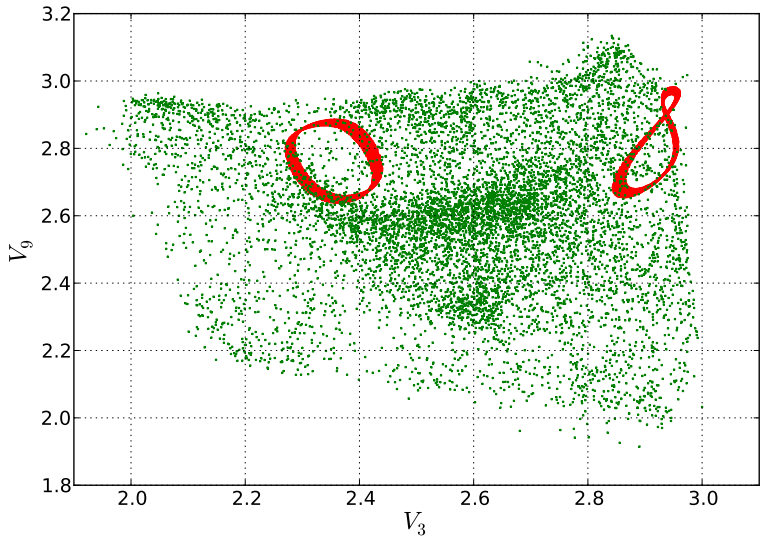

Fig. 4. Poincaré maps for the trajectories shown in Fig. 3. The intersection plane is given by $V_2 = 2.6$. The red pixels are for the intersection of the quasi-periodic trajectory while the green pixels are for the intersection of the hyperchaotic trajectory.

intersection of the V_3V_9-projection of the trajectory with the plane $V_2 = 2.6$ is shown. Note the intersection is only from one side of the $V_2 = 2.6$ plane, i.e. the map was constructed by plotting the coordinates (V_3, V_9) for each intersection point, defined by a change in V_2 from $V_2 - 2.6 \leq 0$ to $0 \leq V_2 - 2.6$, over one integration step. In order to obtain the large number of intersection points shown (between $8000 - 9000$ in each case) both trajectories were integrated for 20000 dimensionless time units, using a step size of $\Delta\tau = 0.025$. The quasi-periodic (hyperchaotic) behaviour of the red (green) trajectory is clearly visible, in agreement with Fig 3 and the calculated values of the Lyapunov exponents.

5 Conclusions

We have demonstrated that the observed erratic behaviour in our simulations of the CVC of coupled IJJs within the CCJJ+DC model is chaotic in origin. We have also shown that transitions can take place between hyperchaotic and chaotic dynamics, as the system jumps from the outermost CVC branch to inner branches. In this preliminary work we have not addressed many other important physical aspects; such as, the influence of the number of junctions, boundary conditions and charge correlations. A more detailed analysis of the chaos is currently in preparation [23].

In future work it would be interesting to establish whether or not the observed chaotic features in the present simulation are also experimentally observable in systems that satisfy the underlying assumptions of the CCJJ+DC model. Perhaps further work could also be done on controlling and exploiting (for technological use) the observed chaos (hyperchaos) in these systems.

References

1.R. Kleiner and P. Muller, Phys. Rev. B **94**, 1327 (1994).
2.L. Ozyuzer *et al.*, Science **318**, 1291 (2007).
3.K. Y. Tsang, R. E. Mirollo, S. H. Strogatz, and K. Wiesenfeld, Physica D **48**, 102 (1991).
4.S. H. Strogatz and R. E. Mirollo, Phys. Rev E **47**, 220 (1993).
5.W. Buckel and R. Kleiner, *Superconductivity: Fundamentals and Applications* (Wiley-VCH, Darmstadt, 2nd edition, 2004).
6.R. Ilmyong, F. Yu-Ling, Y. Zhi-Hai, and F. Jian, Chin. Phys. B **20**, 120504 (2011).
7.C. B. Whan and C. J. Lobb, Phys. Rev. E **53**, 405 (1996).
8.T. Koyama and M. Tachiki, Phys. Rev. B **54**, 16183 (1996).
9.C. B. Whan, C. J. Lobb, and M. G. Forrester, J. Appl. Phys. **77**, 382 (1995).
10.Y. M. Shukrinov, I. R. Rahmonov, and M. E. Demery, J. Phys.: Conf. Ser. **248**, 012042 (2010).
11.Y. M. Shukrinov and M. Hamdipour, Europhys. Lett. **92**, 37010 (2010).
12.M. Machida, T. Koyama, A. Tanaka, and M. Tachiki, Physica C **330**, 85 (2000).
13.Y. M. Shukrinov, F. Mahfouzi, and P. Seidel, Physica C **449**, 62 (2006).
14.Y. M. Shukrinov, F. Mahfouzi, and N. Pendersen, Phys. Rev. B **75**, 104508 (2007).
15.Y. M. Shukrinov and F. Mahfouzi, Phys. Rev. Lett. **98**, 157001 (2007).
16.J. C. Sprott, *Chaos and Time-Series Analysis* (Oxford University Press, London, 2003).
17.A. Wolf, J. B. Swift, H. L. Swinney, and J. A. Vastano, Physica D **16**, 285 (1985).
18.F. Sattin, Comput. Phy. Commun. **107**, 253 (1997).
19.T. Okushima, Phys. Rev. Lett. **91**, 254101 (2003).
20.Z.-M. Chen, K. Djidjeli, and W. G. Price, Applied Mathematics and Computation **174**, 982 (2006).
21.M. T. Rosenstein, J. J. Collins, and C. J. D. Luca, Physica D **65**, 117 (1993).
22.H. Kantz, Phys. Lett. A **185**, 77 (1994).
23.Y. M. Shukrinov, M. Hamdipour, M. R. Kolahchi, A. E. Botha, and M. Suzuki, Phys. Rev. B, in preparation.

Synchronization of semiconductor lasers with complex dynamics within a multi-nodal network

Michail Bourmpos, Apostolos Argyris and Dimitris Syvridis

National and Kapodistrian University of Athens, Panepistimiopolis,
Ilisia,15784, Greece
E-mail: mmpour@di.uoa.gr , argiris@di.uoa.gr , dsyvridi@di.uoa.gr

Abstract: Semiconductor lasers are non-linear devices that exhibit stable, periodic, complex or chaotic dynamics, and in coupled configurations - under strict conditions - can be efficiently synchronized. Applications in communications using such devices for increased security usually employ a twofold system, the emitter and the receiver. In this investigation we examine the potential of this synchronization property to extend to communication networks with as many as 50 or a 100 users (nodes) that are coupled to each other through a central node, in a star network topology.
Keywords: Chaos synchronization, mutual coupling, network synchronization, semiconductor lasers.

1. Introduction

Over the past decades a lot of effort has been put into exploiting chaotic dynamics of signals in areas like communications [1-3], control systems [4], artificial intelligence [5] and more. Chaotic signals emitted from semiconductor lasers (SLs) have been frequently used in security applications for data encryption [6], random number generation [7] etc. A usual configuration that the above types of applications employ consists of two elements - the emitter and the receiver - whose outputs are efficiently synchronized. More complex configurations have been adopted in recent works, where the idea of building a network of coupled SLs emitting synchronized chaotic signals has been proposed [8]. More specifically, Fischer et al [9] have demonstrated isochronal synchronization between two SLs relayed through a third SL, even in cases of large coupling time delays. Zamora-Munt et al [10] have shown operation in synchrony of 50 to 100 distant lasers, coupled through a central SL in a star network topology. In the above work, couplings between distant lasers and the central one are symmetric and the time delays (distances) from the central to the star lasers are assumed equal. The optical injection effect is based on moderate coupling strengths while little attention has been paid on the complexity and the spectral distribution of the signals.

In our work we use a large population -50 to 100- distant lasers which proves to be a sufficient number for good synchrony of the optical signals emitted, as discussed in [10]. Strong optical injection and asymmetric mutual couplings are adopted, enabling the increase on the effect that lasers have to each other through mutual coupling, while preserving the level of output optical power in logic values (up to a few mW). Although intrinsic laser characteristics are selected to be identical in our simulations, different laser operational frequencies were assumed in terms of detuning values from a reference frequency ω_0.

2. Network Architecture and Rate Equations

We first consider a star network topology with N=50 semiconductor lasers, which from now on we will refer to as 'star lasers', relayed through a central similar semiconductor laser, called 'hub laser'.

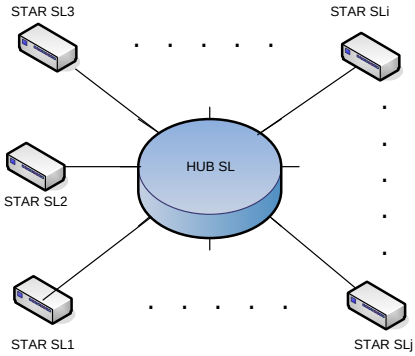

Figure 1. Star network architecture of N 'star' lasers, relayed through mutual couplings with a central 'hub' laser

A rate equation mathematical model is used to describe the operation and dynamics of the above system of devices. This model is based on the Lang Kobayashi rate equation model [11], originating from the representation used in [9] and including frequency detuning terms as in [10]. The complex optical fields and carrier numbers for the star and hub lasers can be calculated from :

$$\frac{dE_j(t)}{dt} = i\Delta\omega_j E_j(t) + \frac{1}{2}(1+ia)\left(G_j(t) - \frac{1}{t_{ph}}\right)E_j(t) + k_H E_H(t-\tau_H)e^{-i\omega_0\tau_H} + \sqrt{D}\xi_j(t) \quad (1)$$

$$\frac{dN_j(t)}{dt} = \frac{I_j}{e} - \frac{N_j(t)}{t_s} - G_j(t)\left|E_j(t)\right|^2 \quad (2)$$

$$\frac{dE_H(t)}{dt} = i\Delta\omega_H E_H(t) + \frac{1}{2}(1+ia)\left(G_H(t) - \frac{1}{t_{ph}}\right)E_H(t) + \beta\cdot\sum_{j=1}^{N} k_j E_j\left(t-\tau_j\right)e^{-i\omega_0\tau_j} + \sqrt{D}\xi_H(t) \quad (3)$$

$$\frac{dN_H(t)}{dt} = \frac{I_H}{e} - \frac{N_H(t)}{t_s} - G_H(t)|E_H(t)|^2 \quad (4)$$

$$G_{j,H}(t) = \frac{g_n\left(N_{j,H}(t) - N_0\right)}{1 + s\left|E_{j,H}(t)\right|^2} \quad (5)$$

All laser have identical intrinsic parameters, with values as follows:

TABLE 1
INTRINSIC LASER PARAMETERS

α	linewidth enhancement factor	5
t_{ph}	photon lifetime	2*psec*
ω_0	reference laser frequency	$2\cdot\pi\cdot\lambda_0$
λ_0	reference laser wavelength	1550*nm*
D	noise strength	10^{-5} $nsec^{-1}$
e	electronic charge	$1.602\cdot10^{-19}$ C
t_s	carrier lifetime	1.54*nsec*
g_n	gain coefficient	$1.2\cdot10^{-5}$ $nsec^{-1}$
N_0	carrier density at transparency	$1.25\cdot10^{8}$
s	gain saturation coefficient	$5\cdot10^{-7}$

$\xi_j(t)$ and $\xi_H(t)$ are uncorrelated complex Gaussian white noises for the star and hub lasers respectively. The star lasers are biased at I_j=25mA, while the hub laser is biased at I_H=9mA, well below the solitary lasing threshold (I_{th}=17.4mA). Each laser is detuned with respect to the reference laser frequency ω_0, at variable values $\Delta\omega_j$ (star lasers) and $\Delta\omega_H$ (hub laser). Especially for the hub laser detuning, we can assume $\Delta\omega_H$ =0 without loss of generality. Delay times (τ_j=τ_H=5ns) and coupling strengths k_j=k_H=k are identical. Coupling asymmetry is achieved through the asymmetry coupling coefficient β. While each star laser receives a single injection field from the hub (k_H), the hub laser receives the sum of injection fields (k_j) of the N star lasers, which could be rather large. To counteract for this large value, β receives values smaller than 1, decreasing the overall injected optical field into the hub, keeping it within a realistic range of values.

3. Simulations and Numerical Results

Simulations were performed for the set of rate equations presented, using the 4th order Runge-Kutta method, with a time-step of 0.8psec. Optical power is deducted from the complex optical field using the appropriate conversion [12]. First we have evaluated the behavior of N=50 star lasers with detuning values ±1GHz around the reference frequency, following a Gaussian distribution, for different values of coupling strength and coupling asymmetry coefficient. Star lasers are ordered based on their detuning, so the 1st laser has the most negative detuning, while the 50th has the largest positive one. Based on these simulations, a mapping of mean and minimum zero-lag cross-correlation between the 50 star lasers was built. As we can see in figure 2, two different yellow-white areas of high correlation exist, one for low and one for high values of the product of coupling strength and coupling asymmetry coefficient ($k\cdot\beta$).

Moving along the diagonal from lower left to upper right corner of figure 2(i) - that is from lower to higher values of the product $k\cdot\beta$ - we encounter the following areas: first a small area in black, where correlation is low, the star lasers operate in CW mode with noise and the hub is not receiving enough coupling in order to emit in lasing mode.

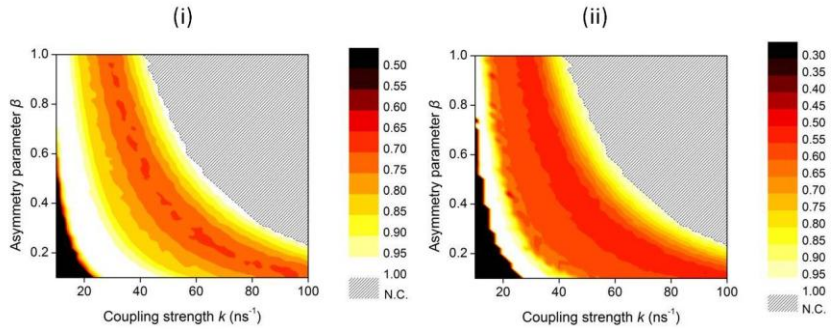

Figure 2. Mean (i) and minimum (ii) zero-lag correlation for 50 lasers with ±1GHz detuning values

Then we come across a white area, where $k \cdot \beta$ product has small values; the star lasers are characterized with periodic dynamics and the hub laser emits just above threshold. A further increase of $k \cdot \beta$ leads to star laser emission with chaotic dynamics (yellow-orange area). The hub laser now emits in the order of few hundreds μW but the mean correlation experiences significant decrease. As the product $k \cdot \beta$ increases optical injection becomes large enough to drive the star lasers into emitting signals of high correlation (small yellow-white stripe). The complexity of these signals slightly decreases and the hub laser now emits in the order of several mW. Finally the hatched area is an uncharted region where optical injection and emitted optical powers are unrealistically large and the rate equation model does not converge.

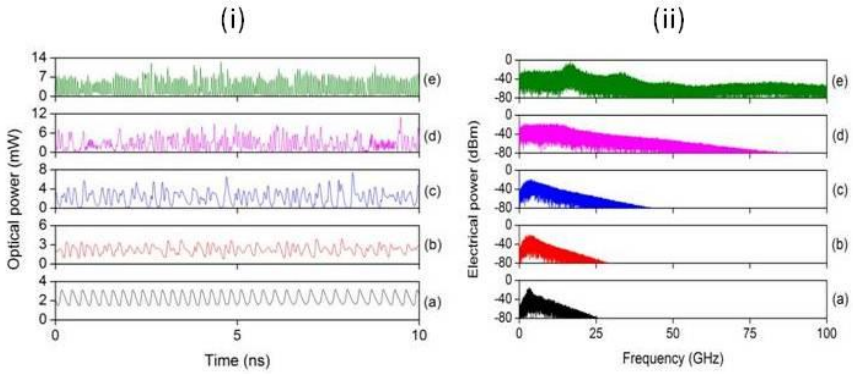

Figure 3 Time traces (i) and spectra (ii) of a single laser for network of 50 lasers with ±1GHz detuning values, coupling strengths $k_J=k_H=60\text{nsec}^{-1}$ and coupling asymmetry coefficients (a) $\beta=0.15$, (b) $\beta=0.2$, (c) $\beta=0.4$, (d) $\beta=0.8$ and (e) $\beta=1$.

Time traces and spectra of the different cases we have just described are shown in figure 3(ii), for a fixed coupling strength value of $k=60\text{nsec}^{-1}$. It is evident that for larger values of the product $k \cdot \beta$ we have faster oscillations attributed to

bandwidth enhancement, as has been commonly reported in cases of strong optical injection [13-14].

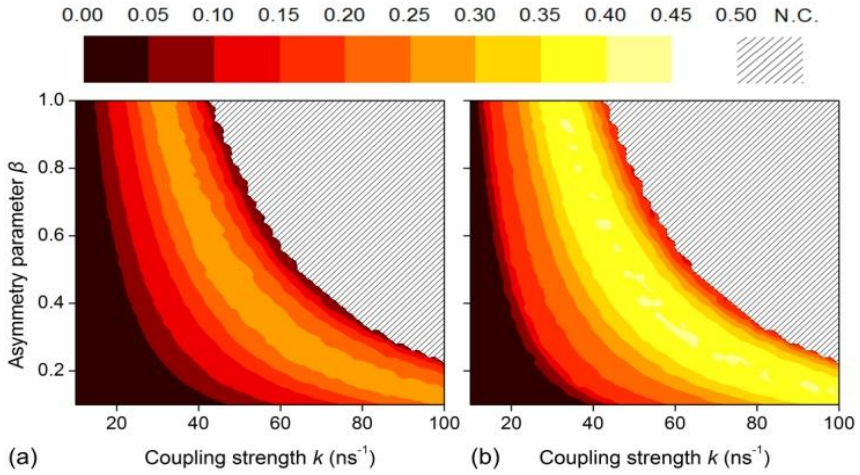

Figure 4. Mean (a) and maximum (b) synchronization error for 50 lasers with ±1GHz detuning values

Another useful parameter we have estimated to evaluate the star lasers output waveforms is the zero-lag synchronization error. Synchronization error is normalized in the mean value of the *i*th and *j*th laser, averaged in the duration T_{av} and is thus expressed in the form:

$$\varepsilon_{ij} = \langle \frac{|P_i(t) - P_j(t)|}{0.5 \cdot \left(P_i(t) + P_j(t)\right)} \rangle \qquad (6)$$

As expected, small values of synchronization error between the ith and jth laser are achieved in the same areas where good zero-lag cross-correlation exists (figure 4 vs figure 2). Based on figure 4 we can identify (k,β) pairs where the maximum synchronization error, which indicates the worst behavior in our network, is minimal. One such pair is k=60nsec^{-1}, β=0.5. For this case of parameters we depict the zero-lag correlation between the ith and jth laser (figure 5i). The worst case of synchronization - in which we encounter the minimum correlation - occurs for the pair of lasers with the far most frequency detuning, that is between lasers 1 and 50. We can also observe that lasers with similar detuning values have good correlations with respect to each other, even when possessing large absolute detuning values.

The superimposed time traces of the 50 star lasers for the above pair of parameters are shown in figure 5(ii). We can observe highly synchronized signals at zero lag for the biggest part of the time window depicted. However we can identify small periods of time where synchronization may be lost.

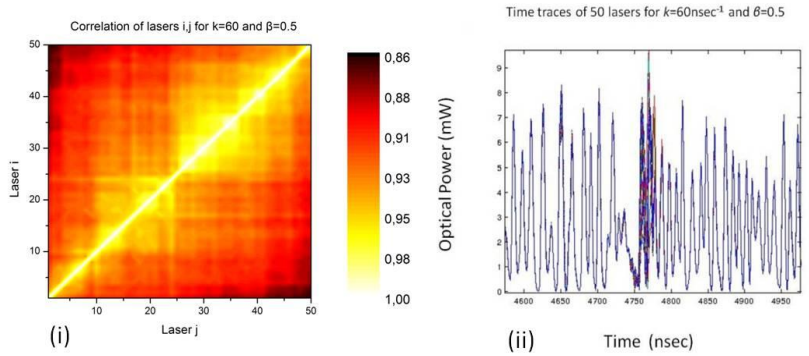

Figure 5. (i) Zero-lag correlation between 50 lasers with ±1GHz detuning values, coupling strengths k_j=k_H=60nsec^{-1} and coupling asymmetry coefficient β=0.5. (ii) Time traces of 50 superimposed star laser outputs ±1GHz detuning values, for he parameter pair k=60nsec^{-1} , β=0.5

The star lasers rapidly synchronize again after a few ns. This phenomenon is repeated in the complete time series and is mainly responsible for the synchronization error calculated, since the synchronization error in the rest of the time window is almost zero.

By increasing the frequency detuning range of the star lasers from ±1GHz to ±10GHz, the system necessitates much larger values of the product $k \cdot \beta$ in order to force the hub laser into lasing emission (figure 6i). As a result, the first area examined, where the star lasers emit in CW mode, is enlarged. The area of non-convergence remains almost the same, while areas of complex dynamics and large cross-correlation values are minimized.

To counteract the increase in the detuning values we attempt to increase the number of star lasers in the network from N=50 to N=100. It is apparent in figure 6ii that inserting more lasers in the network leads to more optical power injected in the hub laser, which now emits for smaller values of the product $k \cdot \beta$. However, small increase in the areas of good cross-correlation is observed.

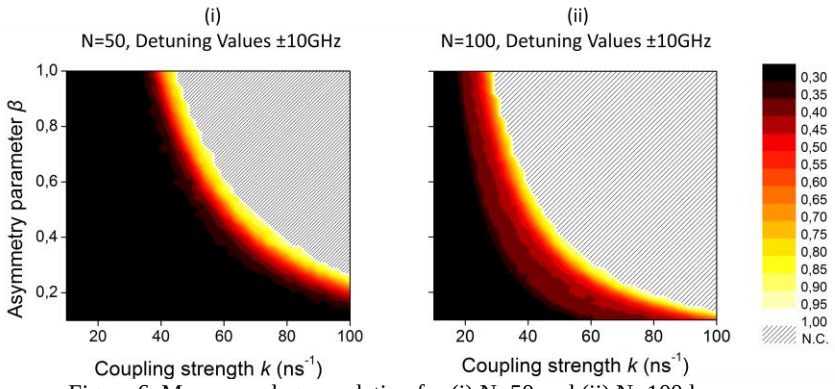

Figure 6. Mean zero-lag correlation for (i) N=50 and (ii) N=100 lasers with ±10GHz detuning values

Another attempt to counteract the increase in detuning values is to lower the pump current of the star lasers to I=18mA near the lasing threshold. This reduces the effect the star lasers dynamics have in the network. In figure 7 we can observe significant increase of the areas of good cross-correlation.

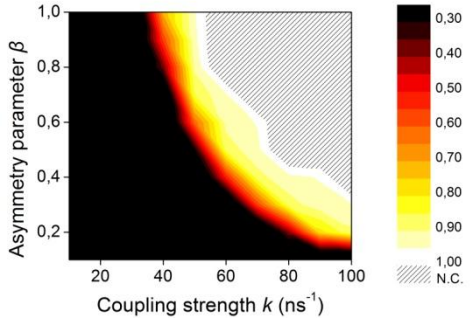

Figure 7. Mean zero-lag correlation for N=50 and pump current I=18mA for the star lasers

Finally, a small analysis was carried out on the type of synchronization occurring in the network and the role the hub laser plays on it. Figure 8 clearly shows that the hub lasers dynamics lag behind the dynamics of the star lasers by exactly the time delay between star and hub lasers, that is $\tau_j=\tau_H=5$ns. As a deduction we can say that the hub laser holds a passive role in the network, operating solely as a relay between the star lasers. The internal parameters of the star lasers, the time delay, coupling strength, asymmetry and driving current seem to be solely responsible for the dynamics of the system.

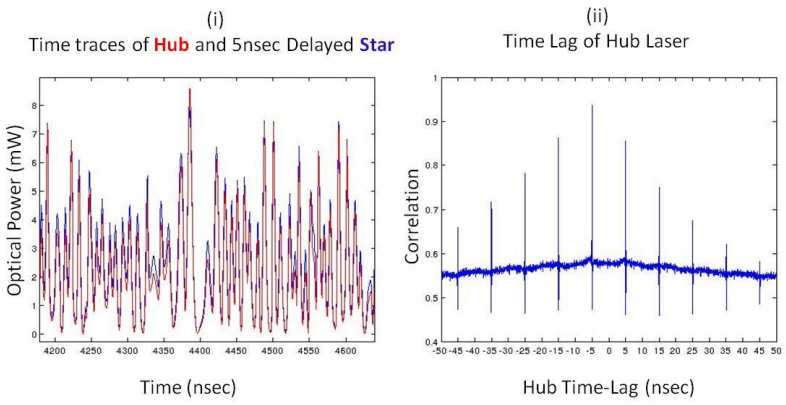

Figure 8. (i) Time traces of hub(red) and one random star (blue) delayed by 5nsec lasers, (ii) Cross-correlation time lag of hub and one random star laser

4. Conclusions

A star network topology with multiple nodes consisting of typical semiconductor lasers has been presented and investigated. Two general areas of good synchronization have been identified, each one with different characteristics in terms of dynamics. The first one, for small values of total optical injection ($k \cdot \beta$ product), produces optical signals of simpler dynamics, while the second one, for large values of $k \cdot \beta$, produces signals with high complexity dynamics. An increase in the number of nodes in the network has proved to enlarge these areas and provide synchronization improvement.

References

[1] L.M. Pecora and T.L. Caroll, "Synchronization in chaotic systems," *Phys. Rev. Lett.*, vol. 64, 821-824, 1990.

[2] P. Colet and R. Roy, "Digital communication with synchronized chaotic lasers," *Opt. Lett.*, vol. 19, pp. 2056–2058, 1994.

[3] A. Argyris, D. Syvridis , L. Larger, V. Annovazzi-Lodi, P. Colet, I. Fischer, J. García-Ojalvo, C.R. Mirasso, L. Pesquera and K.A. Shore, "Chaos-based communications at high bit rates using commercial fiber-optic links," *Nature*, vol. 438, n. 7066, pp. 343-346, 2005.

[4] A.L. Fradkov, R.J. Evans and B.R. Andrievsky, "Control of chaos: methods and applications in mechanics," *Phil. Trans. R. Soc. A*, vol. 364, 2279-2307, 2006.

[5] C. R. Mirasso, P. Colet, and P. Garcia-Fernandez, "Synchronization of chaotic semiconductor lasers: Application to encoded communications," *IEEE Photon. Technol. Lett.*, vol. 8, pp. 299–301, 1996.

[6] V. Annovazzi-Lodi, S. Donati, and A. Scire, "Synchronization of chaotic injected laser systems and its application to optical cryptography," *IEEE J. Quantum Electron.*, vol. 32, pp. 953–959, 1996.

[7] A. Uchida, K. Amano, M. Inoue, K. Hirano, S. Naito, H. Someya, I. Oowada, T. Kurashige, M. Shiki, S. Yoshimori, K. Yoshimura, and P. Davis, "Fast physical random bit generation with chaotic semiconductor lasers", Nature Photon. 2, 728–732 (2008).

[8] R. Vicente, I. Fischer, and C. R. Mirasso, "Synchronization properties of three-coupled semiconductor lasers," *Phys. Rev. E*, vol. 78, 066202, 2008.

[9] I. Fischer, R. Vicente, J.M. Buldú, M. Peil, C.R. Mirasso, M.C. Torrent and J. García-Ojalvo, "Zero-Lag Long-Range Synchronization via Dynamical Relaying," *Phys. Rev. Lett.*, vol. 97, 123902, 2006.

[10] J. Zamora-Munt, C. Masoller, J. Garcia-Ojalvo and R. Roy "Crowd synchrony and quorum sensing in delay-coupled lasers," *Phys. Rev. Lett.*, vol. 105, 264101, 2010.

[11] R. Lang and K. Kobayashi, "External optical feedback effects on semiconductor injection laser properties," *IEEE J. Quantum Electron.*, vol. 16, pp. 347-355, 1980.

[12] K. Petermann, *Laser Diode Modulation And Noise*, New Ed. Kluwer Academic Publishers Group (Netherlands), 1991.

[13] T.B. Simpson and J.M. Liu and A. Gavrielides, "Bandwidth enhancement and broadband noise reduction in injection-locked semiconductor lasers," *IEEE Photon. Technol. Lett.*, vol. 7, pp. 709-711, 1995.

[14] A. Murakami, K. Kawashima and K. Atsuki, "Cavity resonance shift and bandwidth enhancement in semiconductor lasers with strong light injection," *IEEE Quantum Electron.*, vol.39, pp. 1196-1204, 2003.


Proceedings, 5th Chaotic Modeling and Simulation International Conference, 12 – 15 June 2012, Athens Greece

Extensions of Verhulst Model in Population Dynamics and Extremes

M. Fátima Brilhante[1], M. Ivette Gomes[2], and Dinis Pestana[3]

[1] Universidade dos Açores (DM) and CEAUL, Ponta Delgada, Açores, Portugal
(E-mail: fbrilhante@uac.pt)
[2] CEAUL — Centro de Estatística e Aplicações da Universidade de Lisboa, Lisboa, Portugal
(E-mail: ivette.gomes@fc.ul.pt)
[3] CEAUL — Centro de Estatística e Aplicações da Universidade de Lisboa, Lisboa, Portugal
(E-mail: dinis.pestana@fc.ul.pt)

Abstract. Starting from the Beta(2,2) model, connected to the Verhulst logistic parabola, several extensions are discussed, and connections to extremal models are revealed.
Aside from the classical GEV (General Extreme Value Model) from the iid case, extreme value models in randomly stopped extremes schemes are discussed; in this context, the classical logistic Verhulst model is a max-geo-stable model, i.e. geometric thinning of the observations curbs down growth to sustainable patterns. The general differential models presented are a unified approach to population dynamics growth, with factors of the form $[-\ln(1-N(t))]^{P-1}$ and the linearization $[N(t)]^{p-1}$ modeling two very different growth patterns, and factors of the form $[-\ln N(t)]^{Q-1}$ and the linearization $[1-N(t)]^{q-1}$ leading to very different environmental resources control of the growth behavior.
Keywords: Verhulst logistic model, Beta and BeTaBoOp models, population dynamics, extreme value models, geometric thinning, randomly stopped maxima with geometric subordinator.

1 Introduction

Let $N(t)$ denote the size of some population at time t. Verhulst [16], [17], [18] imposed some natural regularity conditions on $N(t)$, namely that $\frac{\mathrm{d}}{\mathrm{d}t}N(t) = \sum_{k=0}^{\infty} A_k[N(t)]^k$, with $A_0 = 0$ since nothing can stem out from an extinct population, $A_1 > 0$ a "growing" parameter, $A_2 < 0$ a retroaction parameter controlling sustainable growth tied to available resources, see also Lotka [9].

The second order approximation $\frac{\mathrm{d}}{\mathrm{d}t}N(t) = A_1N(t) + A_2[N(t)]^2$ can be rewritten

$$\frac{\mathrm{d}}{\mathrm{d}t}N(t) = r\,N(t)\left[1 - \frac{N(t)}{K}\right] \tag{1}$$

where $r > 0$ is frequently interpreted as a Malthusian instantaneous growth rate parameter when modeling natural breeding populations, and $K > 0$ as the equilibrium limit size of the population.

The general form of the solution of the (1) differential equation approximation is the family of logistic functions $N(t) = \dfrac{K\,N_0}{N_0 + (K - N_0)\,\mathrm{e}^{-rt}}$ (where N_0 is the population size at time $t = 0$), and this is the reason why in the context of population dynamics $r\,x\,(1-x)$ is frequently referred to as "the logistic parabola".

Due to the seasonal reproduction and time life of many natural populations, the differential equation (1) is often discretized, first taking r^* such that $N(t+1) - N(t) = r^*\,N(t)\left[1 - \frac{N(t)}{K}\right]$ and then $\alpha = r^* + 1$, $x(t) = \frac{r^*\,N(t)}{r^*+1}$, to obtain $x(t+1) = \alpha\,x(t)[1-x(t)]$, and then the associated difference equation

$$x_{n+1} = \alpha x_n\,[1 - x_n], \tag{2}$$

where it is convenient to deal with the assumption $x_k \in [0,1],\ k = 1, 2, \ldots$ The equilibrium $x_{n+1} = x_n$ leads to a simple second order algebraic equation with positive root $1 - \frac{1}{\alpha}$, and to a certain extent it is surprising that anyone would care to investigate its numerical solution using the fixed point method, which indeed brings in many pathologies when a steep curve — i.e., for some values of the iterates $|\alpha\,(1 - 2\,x_k)| > 1$ — is approximated by an horizontal straight line. This numerical investigation, apparently devoid of interest, has however been at the root of many theoretical advances (namely Feigenbaum bifurcations and ultimate chaotic behavior), and *a posteriori* led to many interesting breakthroughs in the understanding of population dynamics.

Observe also that (2) may be rewritten $x_{n+1} = \frac{\alpha}{6}\,6\,x_n\,[1 - x_n]$, and that $f(x) = 6\,x\,(1-x)\,\mathrm{I}_{(0,1)}(x)$ is the $Beta(2,2)$ probability density function. Extensions of the Verhulst model using difference equations similar to (2), but where the right hand side is tied to a more general $Beta(p,q)$ probability density function have been investigated in Aleixo *et al.* [1] and in Rocha *et al.* [13].

Herein we consider further extensions of population dynamics first discussed in Pestana *et al.* [10], Brilhante *et al.* [5] and in Brilhante *et al.* [3], whose inspiration has been to remark that $1-x$ is the linear truncation of the series expansion of $-\ln x$, as well as x is the linear truncation of the series expansion of $-\ln(1-x)$.

In Section 2, we describe the $BeTaBoOp(p,q,P,Q),\ p,q,P,Q > 0$ family of probability density functions, with special focus on subfamilies for which one at least of those shape parameters is 1.

In section 3, some points tying population dynamics and statistical extreme value models are discussed, namely discussing the connection of the instantaneous growing factors x^{p-1} and $[-\ln(1-x)]^{P-1}$ to models for minima, and the retroaction control factors $(1-x)^{q-1}$ and $[-\ln x]^{Q-1}$ to modeling population growth using maxima extreme value models — either in the

classical extreme value setting, either in the geo-stable setting, where the geometric thinning curbs down growth to sustainable patterns.

2 The $X_{p,q,P,Q} \frown BeTaBoOp(p,q,P,Q)$ models, $p,q,P,Q>0$

Let $\{U_1,U_2,\ldots,U_Q\}$ be independent and identically distributed (iid) standard uniform random variables, $V=\prod_{k=1}^{Q} U_k^{\frac{1}{p}}$, $p>0$ the product of iid $Beta(p,1)$ random variables. As $-\ln V \frown Gamma(Q,\frac{1}{p})$, the probability density function (pdf) of V is $f_V(x)=\frac{p^Q}{\Gamma(Q)}\,x^{p-1}(-\ln x)^{Q-1}\mathrm{I}_{(0,1)}(x)$.

Brilhante *et al.* [5] discussed the more general $Betinha(p,Q)$ family of random variables $\{X_{p,Q}\}$, $p,Q>0$, with pdf

$$f_{X_{p,Q}}(x)=\frac{p^Q}{\Gamma(Q)}\,x^{p-1}(-\ln x)^{Q-1}\mathrm{I}_{(0,1)}(x),\ p,Q>0$$

that can be considered an extension of the $Beta(p,q)$, $p,q>0$ family, since $1-x$ is the linearization of the MacLaurin expansion $-\ln x=\sum_{k=1}^{\infty}\frac{(1-x)^k}{k}$ to derive population growth models that do not comply with the sustainable equilibrium exhibited by the Verhulst logistic growth model.

On the other hand, if $X_{q,P}\frown Betinha(q,P)$, the pdf of $1-X_{q,P}$ is

$$f_{1-X_{q,P}}(x)=\frac{q^P}{\Gamma(P)}\,(1-x)^{q-1}(-\ln(1-x))^{P-1}\mathrm{I}_{(0,1)}(x),\ q,P>0,$$

and the family of such random variables also extends the $Beta(p,q)$ family in the sense that x is the linearization of $-\ln(1-x)$.

Having in mind Hölder's inequality, it follows that

$$x^{p-1}(1-x)^{q-1}[-\ln(1-x)]^{P-1}(-\ln x)^{Q-1}\in\mathcal{L}^1_{(0,1)},\ p,q,P,Q>0,$$

and hence

$$f_{X_{p,q,P,Q}}(x)=\frac{x^{p-1}(1-x)^{q-1}[-\ln(1-x)]^{P-1}(-\ln x)^{Q-1}\mathrm{I}_{(0,1)}(x)}{\displaystyle\int_0^1 x^{p-1}(1-x)^{q-1}[-\ln(1-x)]^{P-1}(-\ln x)^{Q-1}\mathrm{d}x} \tag{3}$$

is a pdf for all $p,q,P,Q>0$. Obviously, $1-X_{p,q,P,Q}=X_{q,p,Q,P}$. For simplicity, in what follows we shall use the lighter notation $f_{p,q,P,Q}$ instead of $f_{X_{p,q,P,Q}}$ for the density of $X_{p,q,P,Q}$.

Brilhante *et al.* [3] used the notation $X_{p,q,P,Q}\frown BeTaBoOp(p,q,P,Q)$ for the random variable with pdf (3) — obviously the $Beta(p,q)$, $p,q>0$

family of random variables is the subfamily $BeTaBoOp(p,q,1,1)$, and the formerly introduced $Betinha(p,Q)$, $p,Q>0$ is in this more general setting the $BeTaBoOp(p,1,1,Q)$ family. The cases for which some of the shape parameters are 1 and the other parameters are 2 are particularly relevant in population dynamics. In the present paper, we shall discuss in more depth $X_{p,1,1,Q}$ and $X_{1,q,P,1}$, and in particular $X_{2,1,1,2}$ and $X_{1,2,2,1}$.

Some of the 15 subfamilies when one or more of the 4 shape parameters p,q,P,Q are 1 have important applications in modeling; below we enumerate the most relevant cases, giving interpretations, for integer parameters, in terms of products of powers of independent $U_k \frown Uniform(0,1)$ random variables.

1. $X_{1,1,1,1} = U \frown Uniform(0,1)$; $f_{1,1,1,1}(x) = \mathrm{I}_{(0,1)}(x)$.
2. $X_{p,1,1,1} = U^{\frac{1}{p}} \frown Beta(p,1)$; $f_{p,1,1,1}(x) = p\,x^{p-1}\mathrm{I}_{(0,1)}(x)$.
3. $X_{1,q,1,1} = 1-U^{\frac{1}{q}} \frown Beta(1,q)$; $f_{1,q,1,1}(x) = q\,(1-x)^{q-1}\mathrm{I}_{(0,1)}(x)$.
4. $X_{1,1,P,1}$, that for $P \in \mathbb{N}$ is 1 minus the product of P iid standard uniform random variables,

$$X_{1,1,P,1} = 1 - \prod_{k=1}^{P} U_k, \quad U_k \frown Uniform(0,1), \text{independent}.$$

   More generally, for all $P>0$, $f_{1,1,P,1}(x) = \dfrac{(-\ln(1-x))^{P-1}}{\Gamma(P)}\,\mathrm{I}_{(0,1)}(x)$, where $\Gamma(P) = \displaystyle\int_0^\infty x^{P-1}\mathrm{e}^{-x}\mathrm{d}x$ is Euler's gamma function.
5. $X_{1,1,1,Q}$, that for $Q \in \mathbb{N}$ is the product of P iid standard uniform random variables,

$$X_{1,1,1,Q} = \prod_{k=1}^{Q} U_k, \quad U_k \frown Uniform(0,1), \text{independent};$$

   alternatively, $X_{1,1,1,Q}$ may be described in the following hierarchical construction: denote $Y_1 \stackrel{\mathrm{d}}{=} X_{1,1,1,1} \frown Uniform(0,1)$, $Y_2 \frown Uniform(0,Y_1)$, $Y_3 \frown Uniform(0,Y_2)$, $\ldots$, $Y_Q \frown Uniform(0,Y_{Q-1})$. Then $Y_Q \stackrel{\mathrm{d}}{=} X_{1,1,1,Q} \frown BeTaBoOp(1,1,1,Q)$.

   More generally, for all $Q>0$, $f_{1,1,1,Q}(x) = \dfrac{(-\ln(x))^{Q-1}}{\Gamma(Q)}\,\mathrm{I}_{(0,1)}(x)$.
6. $X_{p,q,1,1} \frown Beta(p,q)$, with $f_{p,q,1,1}(x) = \dfrac{x^{p-1}(1-x)^{q-1}}{B(p,q)}\,\mathrm{I}_{(0,1)}(x)$, where as usual $B(p,q) = \displaystyle\int_0^1 x^{p-1}(1-x)^{q-1}\mathrm{d}x = \dfrac{\Gamma(p)\,\Gamma(q)}{\Gamma(p+q)}$ is Euler's beta function.

7. $X_{p,1,P,1}$, with pdf $f_{p,1,P,1}(x) = C_{_{p,1,P,1}}\, x^{p-1}\,[-\ln(1-x)]^{P-1}\,\mathrm{I}_{(0,1)}(x)$, where $C_{_{p,1,P,1}} = \dfrac{1}{\int_0^1 x^{p-1}\,[-\ln(1-x)]^{P-1}\mathrm{d}x}$. For $p \in \mathbb{N}$, $C_{_{p,1,P,1}} = \dfrac{1}{\sum_{k=1}^{p}(-1)^{k+1}\binom{p-1}{k-1}\dfrac{\Gamma(P)}{k^P}}$.
8. $X_{1,q,P,1}$, with pdf $f_{1,q,P,1}(x) = \dfrac{q^P}{\Gamma(P)}(1-x)^{q-1}\,[-\ln(1-x)]^{P-1}\,\mathrm{I}_{(0,1)}(x)$.
9. $X_{p,1,1,Q}$, with pdf $f_{p,1,1,Q}(x) = \dfrac{p^Q}{\Gamma(Q)}x^{p-1}\,[-\ln x]^{Q-1}\,\mathrm{I}_{(0,1)}(x)$, that for $Q \in \mathbb{N}$ is the product of Q iid $Beta(p,1)$, i.e. standard uniform random variables raised to the power $\frac{1}{p}$, cf. also Arnold *et al.* [2].
10. ...

(we postpone the discussion of the more complicated models 10-15 to the full paper, since they are not discussed in this shorter version; observe also that the only models for which an explicit evaluation of raw and of central moments is straightforward are those with $q = P = 1$ or with $P = Q = 1$, and so they are the natural candidates to model population dynamics).

3 Population Dynamics, $BeTaBoOp(p, q, P, Q)$ and extreme value models

Brilhante *et al.* [3] used differential equations

$$\frac{\mathrm{d}}{\mathrm{d}t}N(t) = r\,N(t)\,[-\ln[N(t)]]^{1+\gamma} \tag{4}$$

obtaining as solutions the three extreme value models for maxima, Weibull when $\gamma < 0$, Gumbel when $\gamma = 0$ and Fréchet when $\gamma > 0$. The result for $\gamma = 0$ has also been presented in Tsoularis [14] and in Waliszewski and Konarski [19], where as usual in population growth context the Gumbel distribution is called Gompertz function. Brilhante *et al.* [3] have also shown that the associated difference equations

$$x_{n+1} = \alpha\, x_n\,[-\ln\, x_n]^{1+\gamma},$$

exhibit bifurcation and ultimate chaos, when numerical root finding using the fixed point method, when $\alpha = \alpha(\gamma)$ increases beyond values maintaining the absolute value of the derivative limited by 1.

On the other hand, if instead of the right hand side $N(t)\,[-\ln[N(t)]]^{1+\gamma}$ associated to the $BeTaBoOp(2,1,1,2+\gamma)$ we use as right hand side $[-\ln[1-N(t)]]^{1+\gamma}\,[1-N(t)]$, associated to the $BeTaBoOp(1,2,2+\gamma,1)$,

$$\frac{\mathrm{d}}{\mathrm{d}t}N(t) = r\,[-\ln[1-N(t)]]^{1+\gamma}\,[1-N(t)]$$

the solutions obtained are the corresponding extreme value models for minima (and bifurcation and chaos when solving the associated difference equations using the fixed point method). In view of the duality of extreme order statistics for maxima and for minima, in the sequel we shall restrict our observation to the case (4) and the associated $BeTaBoOp(2,1,1,2+\gamma)$ model.

As $-\ln N(t) = \sum_{k=1}^{\infty} \frac{[1-N(t)]^k}{k} > 1 - N(t)$, for the same value of the malthusian instantaneous growth parameter r we have $r\,N(t)\,[1-N(t)] < r\,N(t)[-\ln[N(t)]]$, and hence while (1) models sustainable growth in view of the available resources, (4) models extreme value, arguably destructive unsustained growth — for instance cell growth in tumors.

The connection to extreme value theory suggests further observations:

Assume that U_1, U_2, U_3, U_4 are independent identically distributed standard uniform random variables.

1. The pdf of $\min(U_1, U_2)$ is $f_{\min(U_1,U_2)}(x) = 2\,(1-x)\,\mathrm{I}_{(0,1)}(x)$ and the pdf of $\max(U_1, U_2)$ is $f_{\max(U_1,U_2)}(x) = 2\,x\,\mathrm{I}_{(0,1)}(x)$. Hence the $Beta(2,2) \equiv BeTaBoOp(2,2,1,1)$ tied to the Verhulst model (1) is proportional to the product of the pdf of the maximum and the pdf of the minimum of independent standard uniforms.
2. The pdf of the product U_3U_4 is $f_{(U_3U_4)}(x) = -\ln x\,\mathrm{I}_{(0,1)}(x)$ — and more generally, the pdf of n independent standard uniform random variables is a $BeTaBoOp(1,1,1,n)$ — and hence the pdf of the $BeTaBoOp(2,1,1,n)$ tied to (4) is proportional to the product of $f_{\max(U_1,U_2)}$ by $f_{(U_3U_4)}$. Interpreting $f_{\max(U_1,U_2)}\,f_{(U_3U_4)}$ and $f_{\max(U_1,U_2)}\,f_{\min(U_1,U_2)}$ as "likelihoods", this shows that the model (4) favors more extreme population growth than the model (1).
   More explicitly, the probability density functions $f_{1,1,1,2}f_{(U_3U_4)}(x) = -\ln x\,\mathrm{I}_{(0,1)}(x)$ and $f_{1,2,1,1}f_{\min(U_1,U_2)}(x) = 2\,(1-x)\,\mathrm{I}_{(0,1)}(x)$ intersect each other at $x \approx 0.203188$, and scrutiny of the graph shows that the probability that $U_3\,U_4$ takes on very small values below that value is much higher than the probability of $\min(U_1, U_2) < 0.203188$, and therefore the controlling retroaction tends to be smaller, allowing for unsustainable growth.
   For more on product of functions of powers of products of independent standard uniform random variables, cf. Brilhante *et al.* [4] and Arnold *et al.* [2].
3. Rachev and Resnick, [11] developed a theory of stable limits of randomly stopped maxima with geometric subordinator (also called geo-max stability) similar to what had been independently achieved by Rényi [12], Kovalenko [7] and in all generality by Kozubowski [8], for a panorama cf. also Gnedenko and Korolev, [6].
   The geo-stable maxima laws are the logistic, the log-logistic and the simetrized log-logistic (corresponding to the Gumbel, Fréchet and Weibull when there is no geometric thinning, and with similar characterization

of domains of attraction). Hence, the classical Verhulst (1) population growth model can also be looked at as an extreme value model, but in a context where there exists a natural thinning that maintains sustainable growth.

More involved population dynamics growth differential equation models do have explicit solution for special combinations of the shape parameters, for instance the solution of

$$\frac{\mathrm{d}}{\mathrm{d}t}N(t) = r\,[N(t)]^{2-\gamma}\,\left[1-\frac{N(t)}{K}\right]^{\gamma}, \quad \gamma < 2 \tag{5}$$

is

$$N(t) = \frac{K}{1+\left\{(\gamma-1)\,r\,K^{1-\gamma}t + \left(\frac{K}{N_0}-1\right)^{1-\gamma}\right\}^{\frac{1}{1+\gamma}}}$$

as shown by Turner *et al.* [15], cf. also Tsoularis [14].

References

1. Aleixo, S., Rocha, J.L., and Pestana, D., Probabilistic Methods in Dynamical Analysis: Population Growths Associated to Models Beta (p,q) with Allee Effect, in Peixoto, M. M; Pinto, A.A.; Rand, D. A. J., editors, *Dynamics, Games and Science, in Honor of Maurício Peixoto and David Rand*, vol II, Ch. 5, pages 79–95, New York, 2011. Springer Verlag.
2. Arnold, B. C., Carlos A. Coelho, C. A., and Marques, F. J., The distribution of the product of powers of independent uniform random variables – A simple but useful tool to address and better understand the structure of some distributions, *J. Multivariate Analysis*, 2012, doi:10.1016/j.jmva.2011.04.006.
3. Brilhante, M. F., Gomes, M. I., and Pestana, D., BetaBoop Brings in Chaos. *Chaotic Modeling and Simulation*, 1: 39–50, 2011.
4. Brilhante, M. F., Mendonça, S., Pestana, D., and Sequeira, F., Using Products and Powers of Products to Test Uniformity, In Luzar-Stiffler, V., Jarec, I. and Bekic, Z. (eds.), *Proceedings of the ITI 2010, 32nd International Conference on Information Technology Interfaces*, IEEE CFP10498-PRT, pages 509–514, Zagreb, 2010.
5. Brilhante, M. F., Pestana, D. and Rocha, M. L., Betices, *Bol. Soc. Port. Matemática*, 177–182, 2011.
6. Gnedenko, B. V., and Korolev, V. Yu., *Random Summation: Limit Theorems and Applications*, Bocca Raton, 1996. CRC-Press.
7. Kovalenko, I. N., On a class of limit distributions for rarefied flows of homogeneous events, *Lit. Mat. Sbornik* **5**, 569–573, 1965. (Transation: On the class of limit distributions for thinning streams of homogeneous events, *Selected Transl. Math. Statist. and Prob.* **9**, 75– 81, 1971, Providence, Rhode Island.)
8. Kozubowski, T. J., Representation and properties of geometric stable laws, *Approximation, Probability, and Related Fields*, New York, 321–337, 1994, Plenum.

9. Lotka, A. J., *Elements of Physical Biology*, Baltimore, 1925, Williams and Wilkins Co (reprinted under the title *Elements of Mathematical Biology*, New York, 1956, Dover; original edition downloadable at `http://ia600307.us.archive.org/35/items/elementsofphysic017171mbp/elementsofphysic017171mbp.pdf`).
10. Pestana, D., Aleixo, S., and Rocha, J. L., Regular variation, paretian distributions, and the interplay of light and heavy tails in the fractality of asymptotic models. In C. H. Skiadas, I. Dimotikalis and C. Skiadas, editors, *Chaos Theory: Modeling, Simulation and Applications*, pages 309–316, Singapore 2011. World Scientific.
11. Rachev, S. T., and Resnick, S., Max-geometric infinite divisibility and stability, *Communications in Statistics — Stochastic Models*, 7:191-218, 1991.
12. Rényi, A., A characterization of the Poisson process, *MTA Mat. Kut. Int. Kzl.* **1**, 519–527, 1956. (English translation in *Selected Papers of Alfred Rényi,* **1***, 1948–1956*, P. Turán, editors, 622–279 Akadémiai Kiadó, Budapest, with a note by D. Szász on posterior developments untill 1976).
13. Rocha, J. L., Aleixo, S. M. and Pestana, D. D., *Beta*(p, q)-Cantor Sets: Determinism and Randomness. In Skiadas, C. H., Dimotikalis, Y. and Skiadas, C., editors, *Chaos Theory: Modeling, Simulation and Applications*, pages 333–340, Singapore, 2011, World Scientific.
14. A. Tsoularis. Analysis of logistic growth models. *Res. Lett. Inf. Math. Sci.*, vol. 2:23–46, 2001.
15. M. E. Turner, E. Bradley, K. Kirk, K. Pruitt. A theory of growth. *Mathematical Biosciences*, vol. 29:367–373, 1976.
16. Verhulst, P.-F. Notice sur la loi que la population poursuit dans son accroissement. *Corresp. Math. Physics* 10:113–121, 1938.
17. Verhulst, P.-F. La loi de l'accroissement de la population, *Nouveaux Mémoires de l'Académie Royale des Sciences et Belles-Lettres de Bruxelles*, 18:1–42, 1845. (Partially reproduced in David, H. A., and Edwards, A. W. F. *Annotated Readings in the History of Statistics*, New York, 2001, Springer Verlag.
18. Verhulst, P.-F. Deuxième mémoire sur la loi d'accroissement de la population. *Mémoires de l'Académie Royale des Sciences, des Lettres et des Beaux-Arts de Belgique* 20:1–32, 1847
19. Waliszewski, J., and Konarski, J., A Mystery of the Gompertz Function, in G.A. Losa, D. Merlini, T. F .Nonnenmacher and E.R. Weibel, editors, *Fractals in Biology and Medicine*, Basel, 277–286, 2005, Birkhäuser.

FCT *This research has been supported by National Funds through FCT — Fundação para a Ciência e a Tecnologia, project PEst-OE/MAT/UI0006/2011, and PTDC/FEDER.*


Proceedings, 5th Chaotic Modeling and Simulation International Conference, 12 – 15 June 2012, Athens Greece

Extension of Panjer's iterative procedures and multifractals

M. Fátima Brilhante[1], M. Ivette Gomes[2], and Dinis Pestana[3]

[1] Universidade dos Açores (DM) and CEAUL, Ponta Delgada, Portugal
(E-mail: fbrilhante@uac.pt)
[2] CEAUL — Centro de Estatística e Aplicações da Universidade de Lisboa, Lisboa, Portugal
(E-mail: ivette.gomes@fc.ul.pt)
[3] CEAUL — Centro de Estatística e Aplicações da Universidade de Lisboa, Lisboa, Portugal
(E-mail: dinis.pestana@fc.ul.pt)

Abstract. Binomial, Poisson and Negative Binomial are the basic count models whose probability mass function satisfies a simple recursive relation. This has been used by Panjer [6] to iteratively compute the density of randomly stopped sums, namely in the context of making provision for claims in insurance. Pestana and Velosa [7] used probability generating functions of randomly stopped sums whose subordinator is a member of Panjer's family to discuss more involved recursive relations, leading to refinements of infinite divisibility and self-decomposability in count models. After discussing multifractal measures generated by the geometric and by the Poisson laws, as guidelines to define multifractals generated by general count measures with denumerably infinite support, the complex recursivity of Pestana and Velosa [7] classes of randomly stopped sums is exhibited, hinting that randomness can bring in deeper meaning to multifractality, that, as Mandelbrot argues, is a vague concept that remains without an agreed mathematical definition. A simple random extension of binomial and multinomial multifractals, considering that each multiplier of a cascade is the outcome of some stochastic count model, is also discussed in depth.
Keywords: Count models, probability generating functions, multifractal measures, random multipliers.

1 Introduction

Simple introductory texts on multifractals, e.g. Evertsz and Mandelbrot [1], use binary splitting and multiplicative cascades generating binomial measures as a straightforward and intuitive example. Mandelbrot [4] (p. 83–84 and 89–91) also uses the binomial measure to exhibit the complications that arise when self-similarity and self-affinity are applied to measures rather than to sets, restricting the probability p to take values in the interval $[0, \frac{1}{2}]$.[1]

[1] In fact, for $p = 1/2$ the procedure leads to the uniform measure in (0,1), a straightforward consequence of the binary representation of real numbers in the

Evertsz and Mandelbrot [1], under the heading "Beyond Multinomial Measure" (p. 937–938), briefly mention multifractal measures generated by a countably infinite support probability mass function. In Section 2 we detail the construction of such measures starting either from a geometric distribution or from a Poisson distribution.

On the other hand, Mandelbrot [4] (p. 14) states that "*the terms* fractal *and* multifractal *remain without an agreed mathematical definition*", although the fact that self-similarity, self-affinity and the ensuing mild or wild variability play an essential role in their theory. Binomial, negative binomial and Poisson count measures probability mass functions satisfy some sort of self-similarity, in the sense that $p_{n+1} = (a + \frac{b}{n+1})\, p_n,\ n = 0, 1, \ldots$, a recursive expression that has been successfully used by Panjer [6] to iteratively compute densities of randomly stopped sums whose subordinator is one of the above mentioned count models, and our first choice has been to exploit implications and extensions of this extended kind of self-similarity. Observe that the simplest cases are $N \frown Poisson(b)$ for $a = 0$ and $N \frown Geometric(1 - a)$ for $b = 0$, leading to simple forms of extended self-similarity, and that for this reason are the topic of Section 2.

In Section 3 we briefly mention the basic count models whose probability mass function satisfies some sort of mitigated self-similarity, extending Panjer's [6] class, and we use probability generating functions investigated in [7] to discuss multiple self-similarity.

In Section 4 we discuss other pathways to multifractality, extending the construction of binomial/multinomial measures to accommodate the case of countably infinite support discrete generators, using randomness as a device to operate this alternative extension of multifractality.

2 Geometric and Poisson generated measures

Let $X \frown Exponential\,(1/\delta)$, and define the countably discrete random variable

$$N = \begin{cases} k & k = 0, 1, \ldots \\ p_k = \mathbb{P}[N = k] = \mathbb{P}[k \le X < k + 1] = (1 - \mathrm{e}^{-\delta})(\mathrm{e}^{-\delta})^k \end{cases}$$

interval (0,1) and of Borel's pioneering construction of continuous probability. As Mandelbrot [4] (p. 45) states, "*The definition of multifractality used in this book and almost everywhere else in the literature* [...] *is limited to singular non-negative measures constructed using continuous non-decreasing generators.*"

Feller [2] (p. 141–142), on the same issue, denoting F_p the distribution of $Y_p = \sum_{k=1}^{\infty} \frac{X_k}{2^k}$, where $X_k \frown Bernoulli(p)$, observes that $Y_{\frac{1}{2}}$ is the standard uniform random variable, and that Y_p is a singular random variable for each $p \neq 1/2$. He further comments that "*A little reflection* [...] *reveals that a decision* [on the fairness of a coin] *after finitely many trials is due to the fact that* F_p *is singular with respect to* $F_{\frac{1}{2}}$ *(provided* $p \neq 1/2$*). The existence of singular distributions is therefore essential to statistical practice.*"

i.e., $N = \lfloor X \rfloor \frown Geometric(1 - \mathrm{e}^{-\delta})$ ($\lfloor x \rfloor$ denotes the integer part of x).

On the other hand, from the probability integral transform,

$$1 - \mathrm{e}^{-\delta X} \stackrel{\mathrm{d}}{=} \mathrm{e}^{-\delta X} \stackrel{\mathrm{d}}{=} U \frown Uniform[0,1].$$

Thus, starting from the interval [0,1], in the first step [0,1] is splitted in countably many subintervals,

$$[0,1] = \bigcup_{k=0}^{\infty} \left(\mathrm{e}^{-(k+1)}, \mathrm{e}^{-k}\right] = \bigcup_{k=0}^{\infty} \mathcal{I}_{k(1)}$$

to which we attach probabilities $m_k = (1 - \mathrm{e}^{-\delta})(\mathrm{e}^{-\delta})^k,\ k = 0, 1, \ldots$.

In step 2, each $\mathcal{I}_{k(1)}$ is treated as a reduction of the original [0,1] interval, i.e., using self-explaining standard notations for the translation and scaling of sets,

$$\mathcal{I}_{k(1)} = \bigcup_{j=0}^{\infty} \left\{\mathrm{e}^{-(k+1)} + \left(\mathrm{e}^{-k} - \mathrm{e}^{-(k+1)}\right)\left(\mathrm{e}^{-(j+1)}, \mathrm{e}^{-j}\right]\right\} = \bigcup_{j=0}^{\infty} \mathcal{I}_{j_k(2)},$$

so that $[0,1] = \bigcup_{k=0}^{\infty}\Big(\bigcup_{j=0}^{\infty} \mathcal{I}_{j_k(2)}\Big)$, and to each interval $\mathcal{I}_{j_k(2)}$ we attach the probability $m_k m_j$.

In step 3, the subintervals $\mathcal{I}_{j_k(2)}$ are treated as the $\mathcal{I}_{k(1)}$ intervals in step 2, and similarly in the countably infinite steps that follow to build up a multifractal generated by a Geometric initial measure. Notations soon become cumbersome, but the principles used in the build up of the multiplicative cascade $m_{k_1} m_{k_2} \cdots$ are simple.

The procedure described above is intuitive in view of the geometric discretization of the exponential measure, but it can in fact be used with an initial generator whose support is $\mathbb{N}$, namely $N \frown Poisson(\lambda)$.

$N_G \frown Geometric(p)$ may be looked at as the "unit" of the class of $NegativeBinomial(r,p)$ random variables, in the same sense that $N_B \frown Bernoulli(p)$ is the unit of $Binomial(n,p)$ random variables; on the other hand the sum of independent Poisson random variables is Poisson, and hence we may consider that $N_P \frown Poisson(1)$ is the unit of the class of $Poisson(\lambda)$ random variables. Observe also that the Poisson is a yardstick in the perspective of dispersion, since its dispersion index $\frac{\mathrm{Var}[N_P]}{\mathbb{E}[N_P]} = 1$, while $Binomial(n,p)$ random variables are underdispersed and $NegativeBinomal(r,p)$ random variables are overdispersed.

Observe also that Binomials, Poissons and NegativeBinomials are the only discrete classes of natural exponential families whose variance is at most a quadratic function of the mean value (Morris [5]), who writes "*Much theory is unified for these* [...] *natural exponential families by appeal to their quadratic variance property, including* [...] *large deviations*", one of the tools routinely

used to investigate dimensionality issues in multifractals. Without pursuing the matter further herein, we remark that a differential simile of Panjer's difference iteration is $\frac{f'}{f} = a + \frac{b}{x}$, where f denotes the density function of a positive absolutely continuous random variable, and hence f must be the density of a $Gamma(b+1, -\frac{1}{a})$ random variable, for $b > -1$ and $a < 0$. The gamma random variables are the sole Morris continuous random variables q-th positive support.

3 Extended self-similarity of basic count models

Consider discrete random variables $N_{\alpha,\,\beta,\,\gamma}$ whose probability mass functions (p.m.f.) $\left\{p_n = f_{N_{\alpha,\,\beta,\,\gamma}}(n)\right\}_{n\in\mathbb{N}}$ satisfy the relation

$$\frac{f_{N_{\alpha,\,\beta,\,\gamma}}(n+1)}{f_{N_{\alpha,\,\beta,\,\gamma}}(n)} = \alpha + \beta\,\frac{\mathbb{E}(U_0^n)}{\mathbb{E}(U_\gamma^n)} = \alpha + \frac{\beta}{\sum_{k=0}^n \gamma^k}\,,\ \alpha,\,\beta \in\ \mathbb{R},\ n = 0, 1, \ldots$$

where $U_\gamma \frown Uniform(\gamma,\,1),\ \ \gamma \in (-1,\,1)$. As

$$\mathbb{E}(U_\gamma^n) = \frac{1}{n+1}\,\frac{1-\gamma^{n+1}}{1-\gamma} \underset{\gamma\to 1}{\longrightarrow} 1,$$

Panjer's class corresponds to the degenerate limit case, letting $\gamma \longrightarrow 1$ so that $U_\gamma \underset{\gamma\to 1}{\longrightarrow} U_1$, the degenerate random variable with unit mass at 1. Further generalizations may be constructed relaxing the iterative expression to hold for $n \geq k_0$, see Hess *et al.* [3] construction of what they call basic count models.

The probability generating function $\mathcal{G}_{\alpha,\,\beta,\,\gamma}(s) = \sum_{n=0}^{\infty} f_{N_{\alpha,\,\beta,\,\gamma}}(n)\, s^n$ must then satisfy $\mathcal{G}_{\alpha,\,\beta,\,\gamma}(s) = \mathcal{G}_{\alpha,\,\beta,\,\gamma}(\gamma^{n+1}s)\prod_{k=0}^n \frac{1-\alpha\gamma^{k+1}s}{1-[\alpha+\beta(1-\gamma)]\gamma^k s}$. Observing that

$$\frac{\mathcal{G}_{\alpha,\,\beta,\,\gamma}(s)}{\mathcal{G}_{\alpha,\,\beta,\,\gamma}(1)} = \frac{\mathcal{G}_{\alpha,\,\beta,\,\gamma}(\gamma^{n+1}s)}{\mathcal{G}_{\alpha,\,\beta,\,\gamma}(\gamma^{n+1})}\ \prod_{k=0}^{n}\ \frac{\frac{1-\alpha\gamma^{k+1}s}{1-[\alpha+\beta(1-\gamma)]\gamma^k s}}{\frac{1-\alpha\gamma^{k+1}}{1-[\alpha+\beta(1-\gamma)]\gamma^k}}$$

and letting $n \to \infty$,

$$\mathcal{G}_{\alpha,\,\beta,\,\gamma}(s) = \prod_{k=0}^{\infty}\ \frac{1-\alpha\gamma^{k+1}s}{1-\alpha\gamma^{k+1}}\ \ \frac{1-[\alpha+\beta(1-\gamma)]\gamma^k}{1-[\alpha+\beta(1-\gamma)]\gamma^k s}\,. \tag{1}$$

If $\gamma \in [0,1),\ \ \alpha < 0$ and $\beta \in \left\{-\frac{\alpha}{1-\gamma},\,\frac{1-\alpha}{1-\gamma}\right\}$, we recognize in (1) the probability generating function of an infinite sum of independent random variables, the k-th summand being the result of randomly adding 1, with probability $\frac{\alpha\gamma^{k+1}}{\alpha\gamma^{k+1}-1}$, to an independent $Geometric(1-[\alpha+\beta(1-\gamma)]\gamma^k)$

random variable. Each summand exhibits its own scale of extended self-similarity, a characteristic feature observed, in what concerns self-similarity and self-affinity, in strict sense (in Mandelbrot's perspective) multifractals.

The limiting case $\gamma = 1$ may be approached as follows: observing that

$$\frac{\mathcal{G}_{\alpha,\beta,\gamma}(s) - \mathcal{G}_{\alpha,\beta,\gamma}(\gamma s)}{\alpha s[\mathcal{G}_{\alpha,\beta,\gamma}(s) - \mathcal{G}_{\alpha,\beta,\gamma}(\gamma s)] + (1-\gamma)s[\beta\mathcal{G}_{\alpha,\beta,\gamma}(s) + \alpha\mathcal{G}_{\alpha,\beta,\gamma}(\gamma s)]} = 1,$$

dividing the numerator and the denominator by $(1-\gamma)s$ and letting $\gamma \to 1$, we get

$$\frac{\mathcal{G}'_{\alpha,\beta,1}(s)}{\alpha s\mathcal{G}'_{\alpha,\beta,1}(s) + \beta\mathcal{G}_{\alpha,\beta,1}(s) + \alpha\mathcal{G}_{\alpha,\beta,1}(s)} = 1 \Longleftrightarrow \frac{\mathcal{G}'_{\alpha,\beta,1}(s)}{\mathcal{G}_{\alpha,\beta,1}(s)} = \frac{\alpha+\beta}{1-\alpha s},$$

the expression we obtain working out the probability generating function in Panjer's iterative expression $p_{\alpha,\beta}(n+1) = \left(\alpha + \frac{\beta}{n+1}\right) p_{\alpha,\beta}(n)\,,\ \alpha,\ \beta \in \mathbb{R}$, $n = 0, 1, \ldots$.

4 A simple generalization of the binomial/multinomial measure

There are many ways to expand the notion of a multiplicative cascade, one is to consider that each multiplier is the outcome of some stochastic rule. These kind of multiplicative iterative schemes are usually called random multiplicative cascades.

In Section 2 we introduced the geometric and Poisson generated measures. In this section we shall expand differently the notion of random multiplicative cascades by allowing the number of subdivisions that each interval undergoes, at each step of the measure's construction, to be determined by the outcome of a discrete random variable N, where $\mathbb{P}[N \geq 2] = 1$. This procedure generalizes the binomial and multinomial measures in the sense that at step k, $k = 1, 2, \ldots$, the outcome of N dictates the number of subdivisions that each existing interval suffers. On the other hand, the binomial and multinomial measures correspond to N being a degenerate random variable at b, with $b = 2$ and $b > 2$, respectively. In this new scenario the multipliers used at each step also depend on the outcome of N, i.e., $m_i = m_i^{(N)}$.

Starting with the interval [0,1], having uniformly distributed unit mass, the new measure is formally constructed as follows:

Step 1: Generate an observation n_1 from the random variable N. Split the interval [0,1] into the n_1 equally length subintervals

$$[in_1^{-1}, (i+1)n_1^{-1}]\,, \quad i = 0, 1, \ldots, n_1 - 1, \tag{2}$$

receiving uniformly distributed masses $m_i^{(n_1)}$, $i = 0, 1, \ldots, n_1 - 1$, respectively;

Step 2: Generate a second observation n_2 from N, independent from n_1. Split each interval in (2) into n_2 equally length subintervals and use the multipliers $m_i^{(n_2)}$, $i = 0, 1, \ldots, n_2 - 1$, to uniformly distribute the parent interval's mass by these subintervals. After this step is completed the subintervals formed are $[i(n_1 n_2)^{-1}, (i+1)(n_1 n_2)^{-1}]$, $i = 0, 1, \ldots, n_1 n_2 - 1$;

Step k: Generate an observation n_k from N, independent from the previous $k-1$ observations of N. Split each interval from the previous step into n_k subintervals of equal length and use the multipliers $m_i^{(n_k)}$, $i = 0, 1, \ldots, n_k - 1$, to uniformly distribute the parent interval's mass by these subintervals. The subintervals formed after this step are $[i(n_1 n_2 \ldots n_k)^{-1}, (i+1)(n_1 n_2 \ldots n_k)^{-1}]$, $i = 0, 1, \ldots, n_1 n_2 \ldots n_k - 1$;

The new measure μ results from applying the previous procedure infinitely.

An example of a family of multipliers that can be used in this type of measure construction is

$$m_i^{(n)} = \frac{2(i+1)}{n(n+1)} \quad i = 0, 1, \ldots, n-1\,, \tag{3}$$

when $N = n$. (Note that with the multipliers defined in (3) we never observe the case $m_0^{(n)} = m_1^{(n)} = \ldots = m_{n-1}^{(n)} = 1/n$.)

In order to illustrate how the measure is obtained we give a simple example. Suppose that the random variable N has support on the finite set $\{2, 3\}$ with p.m.f. $\mathbb{P}[N = 2] = 1/4$ and $\mathbb{P}[N = 3] = 3/4$. Let us further assume that we observe for the first two steps of the measure's construction the sequence of divisors $(N_1, N_2) = (3, 2)$, where N_1 and N_2 are independent replicas of N. Using the multipliers defined in (3), we get $m_0^{(2)} = 1/3$ and $m_1^{(2)} = 2/3$, and $m_0^{(3)} = 1/6$, $m_1^{(3)} = 1/3$ and $m_2^{(3)} = 1/2$.

At step one we obtain the subintervals $[0, \frac{1}{3}]$, $[\frac{1}{3}, \frac{2}{3}]$ and $[\frac{2}{3}, 1]$, with masses $1/6$, $1/3$ and $1/2$, respectively, and after step two the intervals $[0, \frac{1}{6}]$, $[\frac{1}{6}, \frac{1}{3}]$, $[\frac{1}{3}, \frac{1}{2}]$, $[\frac{1}{2}, \frac{2}{3}]$, $[\frac{2}{3}, \frac{5}{6}]$ and $[\frac{5}{6}, 1]$, with masses $1/18$, $1/9$, $1/9$, $2/9$, $1/6$ and $1/3$, respectively. We should point out that when a measure of this type is being formed, one actually does not know which generator sequence of divisors $(N_1, N_2, \ldots)$ is being used in the construction, and consequently which multipliers are being considered at each step.

In the binomial and multinomial measures the multipliers used throughout all steps are both fixed in value and in number. In this new scheme each multiplier should be regarded as a random variable, since the magnitude and number of multipliers used are directly determined by the distribution of N.

Lets go back to the example to see how this is the case. For the multipliers defined in (3) we can have, e.g., $m_0 = 1/3$ or $m_0 = 1/6$, with probability $1/4$ and $3/4$, respectively, and we shall need to define 3 random multipliers. If M_i denotes the random variable that represents the value of the i-th random

Table 1. Masses for all possible addresses obtained after step 2 using N as divisor

Address	(2,2) [1/16]	(2,3) [3/16]	(3,2) [3/16]	(3,3) [9/16]	Mean mass
0.00	1/9	1/18	1/18	1/36	25/576
0.01	2/9	1/9	1/9	1/18	25/288
0.10	2/9	1/9	1/9	1/18	25/288
0.11	4/9	2/9	2/9	1/9	25/144
0.02	0	1/6	0	1/12	5/64
0.20	0	0	1/6	1/12	5/64
0.12	0	1/3	0	1/6	5/32
0.21	0	0	1/3	1/6	5/32
0.22	0	0	0	1/4	9/64

multiplier,

$$M_0 = \begin{cases} \frac{1}{3} & \frac{1}{6} \\ \frac{1}{4} & \frac{3}{4} \end{cases}, \quad M_1 = \begin{cases} \frac{2}{3} & \frac{1}{3} \\ \frac{1}{4} & \frac{3}{4} \end{cases} \quad \text{and} \quad M_2 = \begin{cases} 0 & \frac{1}{2} \\ \frac{1}{4} & \frac{3}{4} \end{cases}. \tag{4}$$

(The expected values for the multipliers given in (4) are $\mathbb{E}[M_0] = 5/24$, $\mathbb{E}[M_1] = 5/12$ and $\mathbb{E}[M_2] = 3/8$.) For an arbitrarily random variable N, the number of random multipliers M_i will depend on the number of points where N has non null mass.

In each step of this new multiplicative cascade we can also attach an address to each interval generated, as is done in the binomial and multinomial measures (for more details see e.g. Evertsz and Mandelbrot [1]). However, given the way the measure is constructed, we can have different intervals attached to the same address, i.e. there is no one-to-one correspondence between address and interval, contrarily to what happens with the binomial and multinomial measures. Furthermore, intervals with the same address do not have necessarily the same mass. For example, the address 0.00 can be linked to the intervals $[0, \frac{1}{4}]$ if $(N_1, N_2) = (2, 2)$, $[0, \frac{1}{6}]$ if $(N_1, N_2) = (2, 3)$ or $(N_1, N_2) = (3, 2)$ and $[0, \frac{1}{9}]$ if $(N_1, N_2) = (3, 3)$, having masses 1/9, 1/18 and 1/36, respectively. In Table 1 we indicate all possible masses associated with all possible addresses at step 2 (the probability of observing each generator sequence of divisors is shown in brackets underneath). From Table 1 we see that addresses that are permutations of one an other have the same mean mass (this remains true at any step).

The question now is "How can we determine the measure of a particular address $0.\beta_1\beta_2\ldots\beta_k$, $\beta_i = 0, 1, \ldots$, $i = 1, 2, \ldots, k$, which can have a multitude of intervals attached to it, if one does not know which generator sequence $(N_1, N_2, \ldots, N_k)$ was used?" As we shall see next, the answer is quite simple.

We can prove that the address $0.\beta_1\beta_2\ldots\beta_k$ has expected measure

$$\mu_E(0.\beta_1\beta_2\ldots\beta_k) = \mathbb{E}(M_{\beta_1})\mathbb{E}(M_{\beta_2})\ldots\mathbb{E}(M_{\beta_k}),$$

not depending on the generator sequence, but only on the multipliers expectations, which ultimately are influenced by the distribution of N (this is implicit in Table 1). For example, both addresses 0.01 and 0.10 have expected measure $\mathbb{E}(M_0)\mathbb{E}(M_1) = 25/288$.

On the other hand, the singularity of this kind of measure construction prevents the direct application of the classic definitions of coarse and local Hölder exponents given in the literature. However, these definitions can be generalized in order to accommodate this new case. For the generalized coarse Hölder exponent we use

$$\alpha_k(0.\beta_1\beta_2\ldots\beta_k) = \frac{\log(\mu_E(0.\beta_1\beta_2\ldots\beta_k))}{\log\left(\mathbb{E}\left[\left(\prod_{i=1}^{k} N_i\right)^{-1}\right]\right)} \approx -\frac{\log(\mu_E(0.\beta_1\beta_2\ldots\beta_k))}{k\log(\mathbb{E}[N])}$$

and for the generalized local Hölder exponent,

$$\alpha = \lim_{k\to\infty} \alpha_k(0.\beta_1\beta_2\ldots\beta_k) \approx -\lim_{k\to\infty} \frac{\log(\mu_E(0.\beta_1\beta_2\ldots\beta_k))}{k\log(\mathbb{E}[N])},$$

if the limit exists. Note that $\left(\prod_{i=1}^{k} N_i\right)^{-1}$ represents the (random) length of the intervals at step k, $k = 1, 2, \ldots$.

References

1. Evertsz, C. J. G., and Mandelbrot, B. Multifractal Measures. In H.-O. Peitgen, H. Jürgens, and D. Saupe. *Chaos and Fractals: New Frontiers of Science*, pages 921–969, New York, 1993, Springer Verlag.
2. Feller, W. *An Introduction to Probability Theory and its Applications*, vol. II, 2nd ed., New York, 1971, Wiley.
3. Hess, K. Th., Lewald, A., and Schmidt, K. D., An extension of Panjer's recursion, *ASTIN Bulletin* 32:283–297, 2002.
4. Mandelbrot, B. *Multifractals and* $1/f$ *Noise; Wild Self-Affinity in Physics*, New York, 1999, Springer Verlag.
5. Morris, C. N., Natural Exponential Families with Quadratic Variance Functions, *Ann. Statist.* 10:65-80, 1982.
6. Panjer, H. H. Recursive evaluation of a family of compound distributions, *ASTIN Bulletin*, 12:22–26, 1981.
7. Pestana, D., and Velosa, S. Extensions of Katz-Panjer families of discrete distributions, *REVSTAT* 2:145-162, 2004.

FCT *This research has been supported by National Funds through FCT — Fundação para a Ciência e a Tecnologia, project PEst-OE/MAT/UI0006/2011.*